Summer 7-29-2013

Magnetic Interactions in Low-Dimensional Iron Nanostructures

Rui Zhang
University of Nebraska-Lincoln, rzhang@huskers.unl.edu

Magnetic Interactions in Low-Dimensional Iron Nanostructures

by

Rui Zhang

A DISSERTATION

Presented to the Faculty of

The Graduate College at the University of Nebraska

In Partial Fulfillment of Requirements

For the Degree of Doctor of Philosophy

Major: Physics and Astronomy

Under the Supervision of Professor David J. Sellmyer and Professor Ralph Skomski

Lincoln, Nebraska

July, 2013

Magnetic Interactions in Low-Dimensional Iron Nanostructures

Rui Zhang, Ph.D.

University of Nebraska, 2013

Advisor: David J. Sellmyer and Ralph Skomski

Three systems involving low-dimensional magnetic nanostructures, namely the *Kondo Effect in Isolated Cu(Fe) Clusters, Magnetization Reversal in Transition-Metal/Fe:SiO_2 Thin Films,* and *Anisotropy and Micromagnetism of Fe/CrPt Bilayers,* have been investigated to understand the magnetic interactions in iron nanostructures.

Kondo Effect in Isolated Cu(Fe) Clusters —Iron impurities were added into copper clusters embedded in an insulating matrix to ensure that the Kondo effect is strictly confined by the size of the cluster. The Kondo temperature of our naoscale system is 0.7 K, which is greatly suppressed from its bulk value of 29 K and is consistent with our theory prediction. This approach offers a new angle to experimentally probe the Kondo screening cloud.

Magnetization Reversal in Transition-metal/Fe:SiO_2 Thin Films —A novel way has been proposed to improve the performance of the soft-magnetic layers via magnetostatic interactions through iron clusters. All tested soft magnetic materials showed clear signs of coercivity reduction and for certain materials, such as Co-Fe-B, the permeability was

also improved by factors of up to 5. This method opens up a new path towards the design of free layers used in magnetic tunneling junctions and spin-valve structures.

Anisotropy and Micromagnetism of CrPt / Fe Bilayers —Iron thin films, exchange-coupled to an adjacent antiferromagnetic CrPt layer, have been used as a probe to measure the anisotropy of $L1_0$-ordered CrPt. The alloy is of interest as a replacement for the Mn-based antiferromagnetic layers in magnetic tunneling junctions, but its anisotropy has been largely underestimated due to the complications introduced by magnetic annealing. The estimated value from our methods is -438 kJ/m^{3,} which is much closer to its theoretical prediction than values obtained by other experimental methods.

The present findings have several scientific and technologic implications, as described in the main part of the thesis.

ACKNOWLEDGMENTS

I would like to take this this opportunity to show my appreciations to everyone that has helped me during my Ph. D. program.

First, my deepest thank goes to my advisors, Prof. D. J. Sellmyer and Prof. Ralph Skomski. Their knowledgeable guidance and patient tutoring carried me throughout my program. I cannot remember how many times that I approached them with questions and puzzles and left with answers and ideas. It is their supports that have led me through the most challenging time of my life.

I would also like to thank Prof. Sy-Hwang Liou for teaching me many things in experimental physics and beyond, and for supporting my work through the grants sponsored by ARO. Special thanks are due to Prof. Axel Enders for his instructive and valuable suggestions concerning the writing of my thesis. For that, I am most thankful. Also thanks are due to Prof. Jeffrey Shield for serving on my supervisory committee. His timely help is really appreciated.

I would like to thank Prof. Parashu Ram Kharel, Dr. Zhiguang Sun, Dr. Xingzhong Li, Dr. Zhen Li, Dr. Steven Michalski, Dr. Shah Valloppilly, Dr. Lanping Yu, Dr. Damien Le Roy, Dr. Balamurugan Balasubramanian, Dr. Jiong Hua and Dr. Xiaohui Wei for the thoughtful discussion regarding my projects. Special thanks go to Mr. Tom George, Miss Xiaolu Yin and Mr. Bhaskar Das for their unconditional help every step on my way. Their marvelous skills and dedications were what made many of my projects possible and their kindness is what makes the whole department function like a team while feeling like a big family. For that, I am most thankful.

I would also like to thank the following people for helpful discussions and support in the past: Prof. Brian Robertson, Prof. Christian Binek, Prof. Roger Kirby, Dr. Takashi Yotaka, Dr. Lu Yuan, Dr. Lan Gao, Dr. Danqin Feng, Dr. Xi He, Dr. Yushun Lin, Dr. Xumin Chen, Mr. Brian Jones, Mr. Yuan Tian, Miss L. Nicholl and Miss Qianqian Jiao.

Many thanks to the support team at the Physics Department, Michael J. Jensen, Les Marquart, Bob Rhynalds, Keith Placek, Pat Pribil, Dr. John R. Kelty and Brian Farleigh, Shelli Krupicka, Patty Christen, Theresa Sis, Kay Haley, Jenny Becic and Joyce McNeil.. Without their dedication my research would not have run as smoothly.

Special thanks go to my parents Jizu Zhang and Hong Zhao who are always there for me and always believe in me, and also thank my wife Ningna Hu for her love and support for so many years and more to come. Last but not least, I wish to thank my two wonderful kids Ryan and Bryan who lighten my life in the way that nobody has ever done before.

Table of Contents

LISTS OF MULTIMEDIA OBJECTS

Chapter 1 : Introduction

Magnetic nanostructures, defined by feature sizes below one micrometer, exhibit fascinating physics, since structural length scales would greatly interfere with physical length scales and cause intriguing new effects [1.1, 1.2]. In the Kondo effect [1.3], for instance, magnetic impurities are screened by conduction electrons and these electrons form a Kondo screening cloud that often extends over hundreds of nanometers [1.4]. However, if the dimension of the conduction sea surrounding the impurity is only a few nanometers in all directions, the Kondo screening cloud cannot expand to site, which affects the low-temperature Kondo behavior [1.5]. Another example is magnetic domain walls. When the dimension of the magnetic system becomes comparable to about 5 to 100 nm depending on the anisotropy and geometry of the specimen [1.6], magnetic domains do not form since the increase of exchange energy can no longer be compensated by the reduction of the magnetostatic energy and the magnetic reversal is then governed by the coherent rotation of the magnetization [1.2]. Such effects are scientifically interesting and have many implications in technology [1.7].

Among all elements important in magnetism, iron is probably the most versatile and intriguing one. It exhibits a particularly rich physics, partially due to its location near the middle of the transition-metal (TM) series, and is also the most widely used magnetic element in technological applications, from Fe-Si and permalloy soft magnets to microwave ferrites and permanent magnets such as $Nd_2Fe_{14}B$ and $BaFe_{12}O_{19}$ [1.8, 1.9]. This, and the existence of a variety of Fe-based research projects at the University of

Nebraska, has prompted us to investigate several Fe-based nanostructures, as illustrated in Figure 1-1.

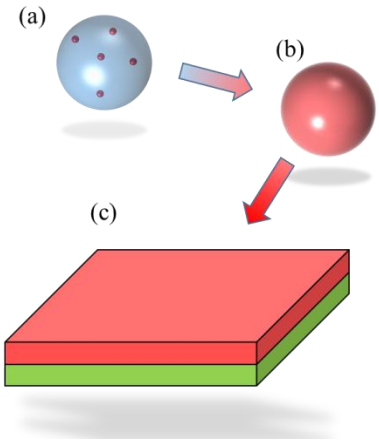

Figure 1-1 Basic geomechies of the Fe-nanostructures investigated in this thesis: (a) Fe atoms in Cu clusters (b) Soft-magnetic Fe nanoparticles and (c) Fe thin film on a CrPt layer

1.1 Synopsis of Research

The present dissertation is based on several subprojects. Three of these projects, namely: I. *Kondo Effect in Isolated Nanoparticles* [1.5, 1.10], II. *Free-Layer Magnetization Reversal in Magnetic Sensors* [1.11] and III. *Anisotropy and Micromagnetism of Fe/CrPt Bilayers* [1.12], form the main part of this thesis. They will be discussed in the remaining sections of the introduction and in the main part of the thesis. In addition, the thesis work contains three minor research projects, which are briefly summarized in this section.

FePt and CoPt $L1_0$ Phase Formation. — The demand for innovative methods to prepare $L1_0$ phase FePt and CoPt with (001) texture and small grain size has fueled researches regarding the phase formation and magnetic properties of these alloys. For CoPt thin films deposited at elevated temperature on (001) MgO substrates, it has been

demonstrated that a properly inserted Au layer can effectively lower the phase-formation temperature down to 350 °C while maintaining reasonably strong perpendicular anisotropy and a large coercivity of 6 kOe [1.13]. For the FePt thin film deposited at the room temperature, both heat treatment methods can be used to promote growth of the $L1_0$ phase, but samples treated with ion-beam irradiation show strong (111) texture and large grain size [1.14]. Another $L1_0$ phase system, namely CrPt, was encountered during the search for the replacement for Mn-base antiferromagnetic (AFM) materials [1.12] and is dealt with in Project III (Chapter 6).

High Temperature Resistance Measurement System. —The high temperature resistance measurement system is an important tool regarding heat treatment and characterization of magnetic tunneling junctions (MTJ). It offers additional information regarding the high-temperature performance of the MTJ and the effectiveness of the heat treatment. It has been used in the MTJ noise research [1.15] and provided essential information regarding the effect of heat treatment on the exchange bias, which is presented in Project III (Chapter 6).

Magnetoresistive FORC Measurements. — First Order Reversal Curve (FORC) diagrams [1.16, 1.17] are an elaborate and time-consuming method to extract information about reversible and irreversible magnetization processes, normally based on $M(H)$ hysteresis loops. We have developed an alternative approach, namely magnetoresistive FORC (MR-FORC). This approach is possible because magnetoresistance (MR) measurements yield information regarding magnetization reversal that is very similar to *M-H* measurements. Our MR-FORC measurement system has been designed to provide a

new angle towards the analysis MTJs. In the future, it may also yield crucial information regarding the reversibility of TM layer in TM/Fe:SiO_2 bilayer systems (Project II).

1.2 Kondo Effect in Isolated Particles (Project I)

In the 1930s, the resistance minimum observed in many partially ordered metallic systems created a great puzzle regarding its origin [1.18]. A general model was proposed by Anderson in 1961 suggesting the *s-d* exchange interaction between localized impurity spin and conduction electron spins might be responsible for the resistance minimum [1.19], and an atomic explanation was given by Kondo in 1964 based on Anderson's *s-d* exchange model [1.3]. His calculation explained the resistance minimum and the logarithmic behavior. It was also consistent with the experimental results except when $T \to 0$. He confirmed that the origin of the Kondo effect is the scattering and screening of conduction electrons by a magnetic impurity at low temperatures and also suggested the screening is realized by what is no known as the Kondo screening cloud. The disagreement at low temperature was solved by the numerical renormalization group (NRG) analysis, based on earlier work by Wilson [1.20, 1.21]. In the early 1980s, an exact solution regarding *s-d* model S=1/2 was discovered [1.22, 1.23]. The single-impurity Kondo effect is now well understood theoretically. Since the Kondo problem is well defined, it has become a testing ground for many numerical and analytical theories for many-electron problems, including but not limited to heavy Fermion systems [1.24].

For a long time, experimental investigations focused on the low-temperature resistance and magnetic-susceptibility of bulk and thin-film samples, where the Kondo effect was studied for various impurity concentrations [1.25], compositions [1.26], and dimensions [1.27]. Systems involving a single impurity were hard to prepare and

characterize until late 1990s, when scanning tunneling microscopy (STM) was used to directly image the Kondo resonance by scanning the *dI/dV* curve laterally across impurity adatoms on the non-magnetic metal surface [1.28, 1.29]. Since then, new methods have been developed such as electrical measurements of quantum dots [1.30-32] and molecular transistors [1.33, 1.34]. Many efforts have been devoted to directly observe the Kondo screening cloud. In most studies, the Kondo screening cloud diameter is much smaller than the dimensions of the investigated systems. Even for nanoscale Kondo studies, the conduction electrons can still travel beyond the borders of the Kondo screening cloud due to either the surrounding conducting matrix or the contacts required for such measurement [1.5, 1.35]. In other words, the Kondo screening cloud is partially confined to nanoscale in a complicated way. In nanoparticles, the conduction-electron states are discrete and the number of itinerant electrons contributing to the Kondo effect becomes smaller at low temperature. This alters the Kondo behavior and the low-temperature magnetic susceptibility [1.5]. Therefore, it is important to establish a system in which bulk and nanoscale Kondo effects can be distinguished.

In Chapter 4, a procedure has been developed to investigate the Kondo effect with a confined Kondo screening cloud. Copper clusters doped with iron impurities are embedded in SiO_2 matrix which prevents the Kondo screening cloud from reaching its full extension. Magnetic measurements were carried out to study the interactions associated among iron atoms inside the copper clusters at low temperatures [1.10].

1.3 Free-Layer Magnetization Reversal in Magnetic Sensors (Project II)

Magnetic-field sensors that utilize the MR phenomenon have drawn great attention, thanks to the achievement of high MR ratios in recent years [1.36-38]. Two mechanisms

are widely used in different magnetic sensors, namely giant magnetoresistance (GMR) [1.39] and tunneling magnetoresistance (TMR) [1.38], both realized by multilayer structures. A soft-magnetic layer that can rotate freely under the influence of an external magnetic field serves as the sensing element and is commonly referred as a free layer. In order to achieve high sensitivity for a magnetic sensor, a few key factors must be met, including high MR ratio, high signal to noise ratio, high permeability and low hysteresis loss [1.9, 1.40-43].

Up to now, many different approaches have been used to improve the performance of the free layer. One way is to use novel materials, such as superparamagnetic materials [1.41, 1.44]. Such systems yield great hysteresis reduction due to the nature of the superparamagnetism, but this is at the expense of a reduced MR ratio and/or a large particle size distribution. Furthermore, by using magnetic flux concentrators (MFCs), some systems show a clear hysteresis reduction [1.44], while others only shows permeability increases [1.40, 1.46]. The implementation of MFCs can be as easy as putting two macroscopic-sizes MFC at each end of the sensor, which makes the device bulky and reduces its resolution [1.45]. Another implementation is through nanofabrication which greatly complicates the sample preparation [1.46]. Additionally, it has been shown that magnetic annealing (MA) can greatly advance the performance of the free layer through magnetic and structural changes of the system [1.15, 1.43]. However, the annealing conditions, such as temperature and time, must be controlled to avoid harmful interdiffusion inside the multilayer structures [1.47]. Moreover, through nanofabrication, one can exploit the shape anisotropy of a small bar or ellipse to assist the magnetization reversal of the free layer [1.15, 1.48]. It is usually beneficial to apply

multiple techniques at the same time. It is, therefore, important to find innovative ways to further improve the magnetic properties of the free layer of magnetic sensors.

Granular Fe:SiO_2 containing nanosize particles are of interest for many applications such as catalysis [1.49], microwave absorbers [1.50] and biomedical applications [1.51]. The magnetic properties of such system range from superparamagnetic to ferromagnetic (FM) with coercivities of up to 1000 Oe, depending on the preparation process [1.52, 1.53]. The Fe:SiO_2 granular films used in this study have an Fe volume fraction of 38% and Fe clusters with less than 10 nm diameter which are mostly well-separated from each other. Although in this configuration, the behavior of the Fe clusters are dominated by superparamagnetism, the clusters are coupled to an adjacent TM layer, such as NiFe, through magnetostatic interactions. In Chapter 5, we show that the reversibility and permeability of the TM layer can be improved through these types of interactions and that this mechanism offers a new method to improve the performance of modern magnetic sensors [1.11].

1.4 Anisotropy and Micromagnetism of Fe/CrPt Bilayers (Project III)

Although predicted in 1932 and confirmed in 1949 [1.54], AFM materials had little practical use due to the zero net magnetization for a long time. However, when an AFM material is adjacent to a FM layer, the exchange interaction between the AFM and the FM layers strongly affects the magnetic properties of the FM layer [1.55]. For instance, when an AFM/FM bilayer system is cooled through the Néel temperature of the AFM layer in the presence of an external magnetic field, a unidirectional anisotropy is introduced at the AFM/FM interface and the bilayer system normally exhibits a hysteresis-loop shift which is commonly referred as exchange bias. This phenomenon has

been widely used as a magnetization stabilizer in magnetic-field sensors [1.56, 1.57] and magnetic random access memories [1.58]. Despite the wide range of applications, the role of the AFM layer in exchange-bias systems is still not fully understood and sometimes even controversial [1.59-61]. Several models have been proposed and most of them are not mutually exclusive, but they can only partially explain the system and are limited to specific situations, such as single crystals with uncompensated [1.55, 1.62] or fully compensated [1.63-65] spin configurations and for polycrystalline [1.66, 1.67]. This is largely because most observations of the AFM layer are through analyzing the adjacent FM layer. Information regarding the intrinsic properties of AFM materials is still required, such as the magnetocrystalline anisotropy, which is directly related to the unidirectional anisotropy in AFM/FM bilayer structures [1.68].

It is possible to directly extract the anisotropy of the AFM by doing magnetic susceptibility measurements along the easy and hard axes [1.69]. However, the magnetic field required for such measurement is of the order of a few hundred teslas for AFM materials with high anisotropy, such as CrPt. This is difficult to measure by current experimental methods. Some study has proposed to use dynamic complex permeability spectra to estimate the anisotropy of the AFM [1.70]. This method also requires the AFM layer to have a weak anisotropy and to be within its critical thickness which allows the AFM layer to rotate coherently with the FM layer. Another method using the blocking temperature of the exchange bias system was also proposed [1.71,72]. The major drawback is the potential structural changes during the heating process, not to mention the system dependence of the blocking temperature. Using the unidirectional anisotropy to estimate the anisotropy of AFM materials is a commonly used method [1.68]. In this

case, it is crucial to fully establish the exchange bias before the measurement takes place. An enhanced coercivity of the adjacent FM layer could also be observed even when the loop shift is not established [1.56]. In fact, the enhanced coercivity may persist even beyond the blocking temperature of the AFM at which the loop shift vanishes [1.73]. This suggests that the coercivity is closely related to the intrinsic properties of AFM material [1.61, 1.73] and can be used as a characterization tool [1.74]. A suitable AFM/FM bilayer system would be able to link the enhanced coercivity to the anisotropy of the AFM layer.

Our focus is on the AFM alloy CrPt. This $L1_0$ phase CrPt bears many advanced properties in comparison with other AFM materials. It has a good corrosion resistance, a high Néel temperature, and low interdiffusion at high temperatures, which makes it a valuable potential replacement for Mn-based AFM materials currently used in magnetic sensors.[1.75, 1.76] However, the experimental effort towards finding the anisotropy of CrPt has not been very conclusive. Theoretical calculations have suggested that the anisotropy of CrPt is 3500 kJ/m^3 [1.12], while experimental estimations have a much smaller value of 10 kJ/m^3 [1.77]. It is important to identify the origin of the discrepancy. Chapter 6 will show, by analyzing the enhanced coercivity of Fe/CrPt bilayer structure, the estimate of CrPt anisotropy can be much better reconciled with its theoretical value [1.12].

1.5 Overview

The structure of the thesis is as follows. Chapter 2 summaries the theoretical background relevant to this thesis and Chapter 3 introduces the experimental techniques used in this study. Project I, II and III will be presented in Chapter 4, 5 and 6. Finally, Chapter 7 summaries this work and provides an outlook for the future research.

1.6 References

[1.1] R. Skomski, J. Phys.: Condens. Matter **15** (20), R841 (2003).

[1.2] C. L. Dennis, R. P. Borges, L. D. Buda, U. Ebels, J. F. Gregg, M. Hehn, E. Jouguelet, K. Ounadjela, I. Petej, I. L. Prejbeanu, and M. J. Thornton, J. Phys.: Condens. Matter **14** (49), R1175 (2002).

[1.3] J. Kondo, Prog. of Theor. Phys. **32** (1), 37 (1964).

[1.4] L. Kouwenhoven and L. Glazman, Physics World **14** (1), 33 (2001).

[1.5] R. Skomski, R. Zhang, P. Kharel, A. Enders, S. H. Liou, and D. J. Sellmyer, J. Appl. Phys. **107** (9), 09E126 (2010).

[1.6] R. Skomski, *Simple models of magnetism*. (Oxford University Press, Oxford; New York, 2008), pp.349.

[1.7] D. K. Ferry, Science **335** (6064), 45 (2012).

[1.8] R. M. Bozorth, *Ferromagnetism*. (Van Nostrand, New York,, 1951), pp.968.

[1.9] R. A. McCurrie, *Ferromagnetic materials: structure and properties*. (Academic, London; San Diego, 1994) pp.320.

[1.10] R. Zhang, T. A. George, P. Kharel, R. Skomski, and D. J. Sellmyer, J. Appl. Phys. **113** (17), 17E148 (2013).

[1.11] R. Zhang, R. Skomski, X. Yin, S. H. Liou, and D. J. Sellmyer, J. Appl. Phys. **107** (9) (2010).

[1.12] R. Zhang, R. Skomski, X. Z. Li, Z. Li, P. Manchanda, A. Kashyap, R. D. Kirby, S. H. Liou, and D. J. Sellmyer, J. Appl. Phys. **111** (7) (2012).

[1.13] T. Yokota, L. Gao, R. Zhang, L. Nicholl, M. L. Yan, D. J. Sellmyer, and S. H. Liou, J. Magn. Magn. Mater. **286**, 301 (2005).

[1.14] T. Yokota, M. L. Yan, Yingfan Xu, L. Gao, R. Zhang, L. Nicholl, L. Yuan, R. Skomski, D. J. Sellmyer, S. H. Liou, C. H. Lai, C. H. Yang, and S. H. Huang, J. Appl. Phys. **97** (10), 10H306 (2005).

[1.15] S. H. Liou, R. Zhang, S. E. Russek, L. Yuan, S. T. Halloran, and D. P. Pappas, J. Appl. Phys. **103** (7) (2008).

[1.16] C. R. Pike, A. P. Roberts, and K. L. Verosub, J. Appl. Phys. **85** (9), 6660 (1999).

[1.17] A. Stancu, P. Andrei, and L. Stoleriu, J. Appl. Phys. **99** (8) (2006).

[1.18] W. Meissner and B. Voigt, Ann. Phys.-Berlin **7** (8), 892 (1931).

[1.19] P. W. Anderson, Phys. Rev. **124** (1), 41 (1961).

[1.20] K. G. Wilson, B. Am. Phys. Soc. **19** (3), 303 (1974).

[1.21] K. G. Wilson, Rev. Mod. Phys. **47** (4), 773 (1975).

[1.22] P. B. Wiegmann, J Phys C Solid State **14** (10), 1463 (1981).

[1.23] N. Andrei, K. Furuya, and J. H. Lowenstein, Rev. Mod. Phys. **55** (2), 331 (1983).

[1.24] S. Smirnov and M. Grifoni, Phys. Rev. B **84** (23) (2011).

[1.25] J. M. Franz and D. J. Sellmyer, Phys. Rev. B **8** (5), 2083 (1973).

[1.26] K. Inoue and Y. Nakamura, J. Phys. Soc. Jpn. **32** (2), 441 (1972).

[1.27] M. A. Blachly and N. Giordano, Phys. Rev. B **49** (10), 6788 (1994).

[1.28] V. Madhavan, W. Chen, T. Jamneala, M. F. Crommie, and N. S. Wingreen, Science **280** (5363), 567 (1998).

[1.29] A. F. Otte, M. Ternes, S. Loth, C. P. Lutz, C. F. Hirjibehedin, and A. J. Heinrich, Phys. Rev. Lett. **103** (10) (2009).

[1.30] W. Izumida and O. Sakai, J. Phys. Soc. Jpn. **74** (1), 103 (2005).

[1.31] T. Kobayashi, S. Tsuruta, S. Sasaki, T. Fujisawa, Y. Tokura, and T. Akazaki, Phys. Rev. Lett. **104** (3), 036804 (2010).

[1.32] K. Shibata and K. Hirakawa, Appl. Phys. Lett. **93** (6), 062101 (2008).

[1.33] D. Goldhaber-Gordon, J. Gores, H. Shtrikman, D. Mahalu, U. Meirav, and M. A. Kastner, Mat. Sci. Eng. B **84** (1-2), 17 (2001).

[1.34] N. Roch, S. Florens, T. A. Costi, W. Wernsdorfer, and F. Balestro, Phys. Rev. Lett. **103** (19) (2009).

[1.35] O. Ujsaghy and A. Zawadowski, J. Phys. Soc. Jpn. **74** (1), 80 (2005).

[1.36] S. Tsunegi, Y. Sakuraba, M. Oogane, Hiroshi Naganuma, K. Takanashi, and Y. Ando, Appl. Phys. Lett. **94** (25), 252503 (2009).

[1.37] S. Yuasa, J. Physi. Soci. Jpn. **77** (3), 031001 (2008).

[1.38] S. Yuasa and D. D. Djayaprawira, J. Phys. D: Appl. Phys. **40** (21), R337 (2007).

[1.39] M. N. Baibich, J. M. Broto, A. Fert, F. Nguyen Van Dau, and F. Petroff, Phys. Rev. Lett. **61** (21), 2472 (1988).

[1.40] A. S. Edelstein and G. A. Fischer, J. Appl. Phys. **91** (10), 7795 (2002).

[1.41] R. Schad, H. Alouach, J. W. Harrell, M. Shamsuzzoha, and D. Wang, J. Appl. Phys. **93** (10), 8561 (2003).

[1.42] F. C. S. da Silva, W. C. Uhlig, A. B. Kos, S. Schima, J. Aumentado, J. Unguris, and D. P. Pappas, Appl. Phys. Lett. **85** (24), 6022 (2004).

[1.43] J. Hayakawa, S. Ikeda, Y. M. Lee, F. Matsukura, and H. Ohno, Appl. Phys. Lett. **89** (23), 232510 (2006).

[1.44] L. Xi, Z. Z. Zhang, J. B. Wang, C. X. Li, F. S. Li, S. H. Ge, T. Xu, and S. R. Yang, J Phys D Appl Phys **33** (6), 621 (2000).

[1.45] S. H. Liou, X. L. Yin, S. E. Russek, R. Heindl, F. C. S. Da Silva, J. Moreland, D. P. Pappas, L. Yuan, and J. Shen, IEEE T. Magn. **47** (10), 3740 (2011).

[1.46] Z. Marinho, S. Cardoso, R. Chaves, R. Ferreira, L. V. Melo, and P. P. Freitas, J. Appl. Phys. **109** (7), 07E521 (2011).

[1.47] W. G. Wang, C. Ni, A. Rumaiz, Y. Wang, X. Fan, T. Moriyama, R. Cao, Q. Y. Wen, H. W. Zhang, and J. Q. Xiao, Appl. Phys. Lett. **92** (15), 152501 (2008).

[1.48] R. Skomski, J. Phys.: Conden. Matter **15** (20), R841 (2003).

[1.49] M. Yuan, J. Tao, G. Yan, M. Tan, and G. Qiu, Transactions of Nonferrous Metals Society of China **20** (4), 632 (2010).

[1.50] J. Ma, J. Li, X. Ni, X. Zhang, and J. Huang, Appl. Phys. Lett. **95** (10), 102505 (2009).

[1.51] J. H. Byeon and Y. Kim, RSC Adv. (2013).

[1.52] Y. Kanai and S. H. Charap, J. Appl. Phys. **69** (8), 4478 (1991).

[1.53] G. Xiao, S. H. Liou, A. Levy, J. N. Taylor, and C. L. Chien, Phys. Rev. B **34** (11), 7573 (1986).

[1.54] C. G. Shull and J. Samuel Smart, Phys. Rev. **76** (8), 1256 (1949).

[1.55] W. H. Meiklejohn and C. P. Bean, Phys. Rev. **105** (3), 904 (1956).

[1.56] J. Nogués and Ivan K. Schuller, J. Magn. Magn. Mater. **192** (2), 203 (1999).

[1.57] C. Reig, M. D. Cubells-Beltran, and D. R. Munoz, Sensors **9** (10), 7919 (2009).

[1.58] S. S. P. Parkin, K. P. Roche, M. G. Samant, P. M. Rice, R. B. Beyers, R. E. Scheuerlein, E. J. O'Sullivan, S. L. Brown, J. Bucchigano, D. W. Abraham, Yu Lu, M. Rooks, P. L. Trouilloud, R. A. Wanner, and W. J. Gallagher, J. Appl. Phys. **85** (8), 5828 (1999).

[1.59] Ch. Nam, B. K. Cho, and S. P. Lee, J. Appl. Phys. **93** (10), 6584 (2003).

[1.60] A. N. Dobrynin, D. N. Ievlev, K. Temst, P. Lievens, J. Margueritat, J. Gonzalo, C. N. Afonso, S. Q. Zhou, A. Vantomme, E. Piscopiello, and G. Van Tendeloo, Appl. Phys. Lett. **87** (1), 012501 (2005).

[1.61] D. Kaya, P. N. Lapa, P. Jayathilaka, H. Kirby, C. W. Miller, and I. V. Roshchin, J. Appl. Phys. **113**, 17D717 (2013).

[1.62] D. Mauri, H. C. Siegmann, P. S. Bagus, and E. Kay, J. Appl. Phys. **62** (7), 3047 (1987).

[1.63] A. P. Malozemoff, J. Appl. Phys. **63** (8), 3874 (1988).

[1.64] N. C. Koon, Phys. Rev. Lett. **78** (25), 4865 (1997).

[1.65] T. C. Schulthess and W. H. Butler, Phys. Rev. Lett. **81** (20), 4516 (1998).

[1.66] M. D. Stiles and R. D. McMichael, Phys. Rev. B **59** (5), 3722 (1999).

[1.67] A. Harres and J. Geshev, J. Phys.: Condens. Matter **24** (32) (2012).

[1.68] D. Mauri, E. Kay, D. Scholl, and J. K. Howard, J. Appl. Phys. **62** (7), 2929 (1987).

[1.69] J. M. D. Coey, *Magnetism and magnetic materials*. (Cambridge University Press, Cambridge, 2010), p.614.

[1.70] D. Spenato, S. P. Pogossian, D. T. Dekadjevi, and J. Ben Youssef, J. Phys. D: Appl. Phys. **40** (11), 3306 (2007).

[1.71] N. P. Aley and K. O'Grady, J. Appl. Phys. **109**, 07D719 (2011).

[1.72] G. Vallejo-Fernandez, L. E. Fernandez-Outon, and K. O'Grady, Appl. Phys. Lett. **91**, 212503 (2007).

[1.73] J. T. Kohlhepp, H. Wieldraaijer, and W. J. M. de Jonge, Appl. Phys. Lett. **89**, 032507 (2006).

[1.74] T. Kosub, A. Bachmatiuk, D. Makarov, S. Baunack, V. Neu, A. Wolter, M. H. Rümmeli, and O. G. Schmidt, J. Appl. Phys. **112**, 123917 (2012).

[1.75] B. Dai, J. W. Cai, W. Y. Lai, Y. K. An, Z. H. Mai, F. Shen, Y. Z. Liu, and Z. Zhang, Appl. Phys. Lett. **87**, 092506 (2005).

[1.76] G. W. Anderson, Y. M. Huai, and M. Pakala, J. Appl. Phys. **87**, 5726 (2000).

[1.77] B. Dai, J. W. Cai, W. Y. Lai, Y. Z. Liu, Z. Zhang, F. B. Meng, and Y. X. Li, J. Appl. Phys. **99**, 073902 (2006).

Chapter 2 : Theoretical Background

In this chapter, the primary goal is to provide the necessary theoretical background that will be used in the Chapter 4, 5 and 6. Theories and definitions that are closely related to the subject will be introduced and briefly explained while additional details can be found in the references listed at the end.

2.1 Atomic-Scale Magnetism

Magnetic systems are classified by their respond to the external magnetic fields under different circumstances. Some phenomena, such as ferromagnetism, have been used for centuries due to their unique properties while others were only found and implemented recently [2.3, 2.4]. Nonetheless, most of those mechanisms share the same origin on an atomic scale, and a few principles govern a wide range of nanoscale magnetic phenomena.

2.1.1Magnetic Moment and Electron Angular Momentum

One way of creating a magnetic field is to use electric current. In atoms, the corresponding contribution of the total orbital angular momentum is $m = \sqrt{l(l+1)}\,\frac{e\hbar}{2m_e} = \sqrt{l(l+1)}\mu_B$ where m_e is the mass of electron and l is the angular momentum quantum number [2.4]. The projection of the magnetic moment along the external field direction is quantized, $m = -m_l\mu_B$ where m_l is the magnetic quantum number and can have the value of 0, ±1... ±l. Another contribution to the magnetic moment of an atom is from electron spins. The projection of the magnetic moment from electron spins is also quantized, $m = -g_e m_s \mu_B$ where g_e is called the g-factor of the electron with $g_e \approx 2$ and m_s is called secondary spin quantum number which can take the

value of $\pm\frac{1}{2}$ [2.4]. Therefore the magnetic moment from an electron spin is close to one Bohr magneton.

Since electrons possess magnetic moments through both the orbital and the spin angular momenta, the magnetic field generated by the former would interact with the magnetic moment associated with the latter. This effect is known as spin-orbit coupling and only become significant for heavy atoms. It is directly associated with magnetocrystalline anisotropy, magnetostriction, anisotropic MR and the anomalous planar and spin Hall effect [2.3].

In most elements, there is more than one electron in the atom. The magnetic moment of the atom is determined by the total angular momentum of all electrons inside. For light atoms, such as 3*d* TMs, the couplings of orbit-orbit and spin-spin are much stronger than spin-orbit coupling. As a result, the total angular momentum can be acquired by firstly obtaining the total orbital angular momentum and the total spin angular momentum separately and then combining these two terms together [2.4]. This is commonly referred as Russell-Saunders coupling. Since multiple electrons are involved in the process, *J*, *L* and *S* are used to represent total angular momentum quantum number, total orbital quantum number and total spin quantum number respectively.

For many systems, the empirical Hund's rules can be used to calculate the total angular momentum quantum numbers. It contains three parts: firstly, the electrons inside the atom tend to maximize their total spin; secondly, without violating the first rule, electrons tends to maximize their total orbital angular momentum; finally, for atoms with less than half-full shells, $J = |L - S|$ otherwise $J = |L + S|$ [2.6]. The total magnetic

moment of the atom can be written as $m = -g\mu_B\sqrt{J(J+1)}$ where $g = 1 + \frac{J(J+1)+S(S+1)-L(L+1)}{2J(J+1)}$ is called the Landé g-factor.

For 3*d* TMs, the magnetic moment of each atom is mostly contributed from electron spins due to the quenching of the orbital moment [2.7, 2.8]. This is mainly caused by the strong coupling between the orbits and the crystal lattice, which prevents the respond of orbital moments to the external magnetic field [2.6]. Since the spin is only weakly coupled with orbits and crystal lattice for those materials, spin moments are not affected by this effect. For example, the orbital quenching in Fe yields *L* nearly 0 and $J \approx S$ which is 2. We can derive that the Landé g-factor is equal to 2 and the total magnetic moment of a single Fe atom is around 4.9μ_B.

2.1.2Brillouin Theory

The responds of the magnetization to the external field can be characterized by $\chi = dM/dH$ where χ is the magnetic susceptibility and *M* is the magnetization of the sample. The value of χ is a constant only for small magnetic field and is subject to the temperature change. In many cases, such as FM materials, it also depends on the magnetic history of the sample [2.8]. Therefore, the magnetization is not only a function of external magnetic field but also a function of temperature.

For systems where magnetic interactions between particles are negligible, the magnetization of the specimen can be written as $M = N\langle m\rangle$ where *N* is the number of particles inside the specimen. As described in the previous section, the projection of magnetic moment in the direction of the external magnetic field is quantized and has the expression [2.8]

$$\langle m \rangle = gJ\mu_B B_J(x) \tag{2.1}$$

where $x = \frac{gJ\mu_0\mu_B H}{k_B T}$ and $B_J(x)$ is the Brillouin function which is defined as the following

$$B_J(x) = \frac{2J+1}{J}\coth\left(\frac{(2J+1)x}{2J}\right) - \frac{1}{2J}\coth\left(\frac{x}{2J}\right) \tag{2.2}$$

It can be seen from Figure 2-1, the responds between $\langle m \rangle$ and *H* tend to be linear for low magnetic field. Therefore, for small field, we have $\chi \approx \frac{M}{H}$. Through Taylor expansion, the Brillouin function can also be written as [2.4]

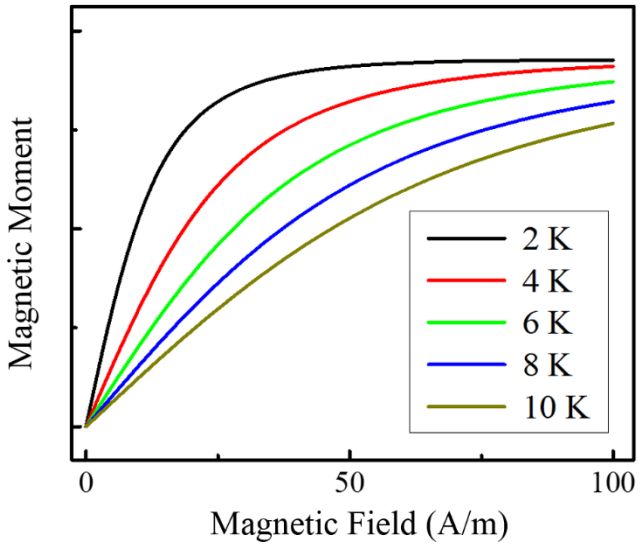

Figure 2-1 Field and temperature dependence of the magnetization of pure magnetic ions with *J*=2. Notice the linear proportion at low field region.

$$B_J(x) = \frac{J+1}{3J}x - \frac{[(J+1)^2 + J^2](J+1)}{90J^3}x^3 + \cdots \tag{2.3}$$

Then the expression for magnetic susceptibility can be written as

$$\chi = \frac{Ng^2J(J+1)\mu_0{\mu_B}^2}{3k_BT} = \frac{C}{T} \tag{2.4}$$

where $C = \frac{Ng^2J(J+1)\mu_0{\mu_B}^2}{3k_B}$ is commonly referred as Curie constant.

2.1.3 Mean Field Theory (MFT)

For systems with long-range order, magnetic interactions between atoms are important. The simplest way to understand these interactions is to consider them under the influence of a molecular field (H_A) that is proportional to their magnetization (M), $H_A = \gamma M$ where γ is called the molecular field constant. In this case, the contribution from the molecular field to the total magnetic field that exerts on the specimen must also be considered. Eq. 2.4 can then be rewritten as

$$\chi = \frac{M}{H} = \frac{C}{T-\theta} \tag{2.5}$$

which is known as the Curie-Weiss law and $\theta = \gamma C$ [2.3]. A positive θ value suggests the magnetic moments inside the specimen are aligned in parallel with each other and is normally referred as the Curie temperature.

The same analogical strategy can also be applied to AFM materials. Simple antiferromganets can be considered as the combination of two sublattices A and B with opposite magnetizations, namely $M_A = -M_B$. The molecular fields associated with each sublattice can then be written as

$$\begin{cases} H_A = \gamma M_A + \gamma' M_B & \text{(a)} \\ H_B = \gamma M_B + \gamma' M_A & \text{(b)} \end{cases} \tag{2.6}$$

where γ is the intra-sublattice molecular field coefficient while γ' is the inter-sublattice molecular field coefficient which has a negative value. Therefore, each sublattice can be treated as a FM system with half of the total atoms of the original system. By using the same method deriving Eq. 2.4, the condition for the appearance of spontaneous sublattice magnetization can be acquired. The Néel temperature (T_N) is equal to $\frac{C}{2}(\gamma - \gamma')$. Following the similar process as FM, the magnetic susceptibility above the Néel temperature can be calculated using

$$\chi = \frac{M_A + M_B}{H} = \frac{C}{T - \theta} \tag{2.7}$$

where $\theta = \frac{C}{2}(\gamma + \gamma')$ is normally a negative number [2.3]. It can be seen that if the intra-sublattice interaction is negligible ($\gamma = 0$), $|\theta| = T_N$.

Below the Néel temperature, the spontaneous magnetization of each sublattice inside the AFM can be represented by a Brillouin function

$$\begin{cases} M_A = \frac{N}{2} gJ\mu_B B_J(x_A) & \text{(a)} \\ M_B = \frac{N}{2} gJ\mu_B B_J(x_B) & \text{(b)} \end{cases} \tag{2.8}$$

where x_i (i=A,B) is a linear function of the molecular field. The susceptibility strongly depends on the direction of the external magnetic field relative to the spin configuration of the AFM. There are two possible scenarios, as illustrated in Figure 2-2.

As shown in Figure 2-2(a), the external magnetic field that is perpendicular to the direction of the magnetization of AFM sublattices cants magnetic moments by a small

angle δ. At the equilibrium state, the molecular field generated by the spin configuration would be completed balanced by the external magnetic field [2.4].

$$H = (H_A + H_B)\sin\delta \tag{2.9}$$

Since $M_A = -M_B$, we can apply Eq. 2.8 to the equation above and have $H = \gamma' M$ where $M = 2M_A \sin\delta$. As a result, the expression for the magnetic susceptibility $\chi_\perp$ can be written as

$$\chi_\perp = \frac{H}{M} = \frac{1}{\gamma'} = const. \tag{2.10}$$

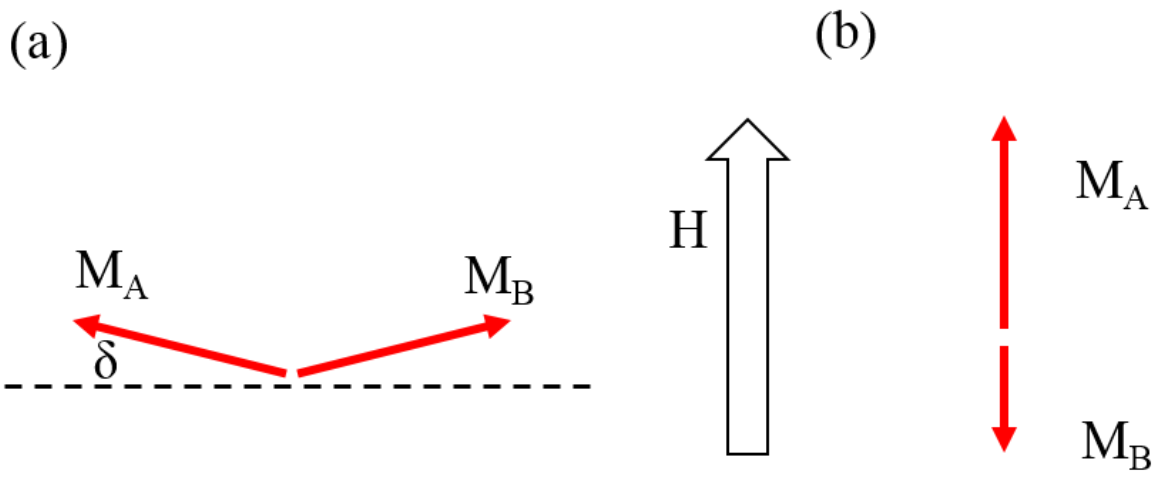

Figure 2-2 Calculation of the AFM susceptibility below T_N with the external magnetic field (a) perpendicular and (b) parallel to the magnetization of AFM sublattices.

Figure 2-2(b) shows the case where a small magnetic field is applied parallel to the magnetization of the AFM sublattices. Magnetizations of the two sublattices are no longer balanced and each can be described using Eq. 2.8

$$\begin{cases} M_A = \frac{N}{2} gJ\mu_B B_J(H_0 + \Delta H) & \text{(a)} \\ M_B = \frac{N}{2} gJ\mu_B B_J(H_0 - \Delta H) & \text{(b)} \end{cases} \quad (2.11)$$

where $B_J(H_0 + \Delta H) = B_J(H_0) + \Delta H B'_J(H_0)$ and H_0 is the molecular field. Eq. 2.11 yields the magnetic susceptibility $\chi_{\parallel} = \frac{M_A + M_B}{\Delta H}$ or

$$\chi_{\parallel} = \frac{2C \frac{3J}{J+1} B'_J(H_0)}{T - \theta} \quad (2.12)$$

where $\theta = \frac{C}{2}\gamma' \frac{3J}{J+1} B'_J(H_0)$. Detailed information regarding the mathematics can be found in the reference [2.6]. For polycrystalline or powder specimens, the magnetic susceptibility lies in the intermediate regime of Figure 2-3 [2.3].

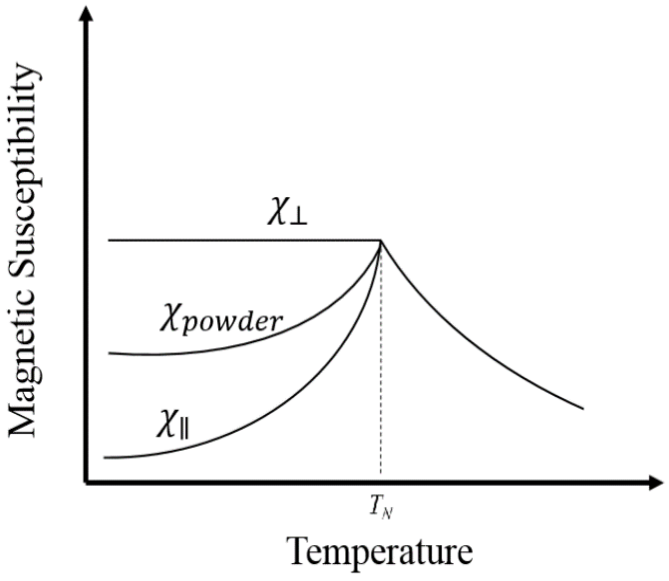

Figure 2-3 Temperature dependence of the magnetic susceptibility of a simple antiferromagnet. From the top to the bottom, the magnetic field is perpendicular, intermediate and parallel to the AFM easy axis, respectively. Redrawn base on reference [2.3].

2.1.4 Anisotropy of Antiferromagnets

Figure 2-3 shows that $\chi_{\parallel}$ is smaller than $\chi_{\perp}$ in the temperature regime below the Néel temperature. However, the AFM spins cannot be easily reconfigured to their energetically most favorite state under the influence of an external magnetic field. The reason is the magnetocrystalline anisotropy, as shown in Figure 2-4(a) [2.3]. The magnetocrystalline anisotropy acts separately on the magnetization of each sublattice, which effectively keeps the sublattice magnetizations parallel to the AFM easy axis. The external magnetic field that is applied to the parallel direction of the AFM spins should at least surpass certain value (H_{sf}) to overcome this effect as suggested in Figure 2-4(b). It is possible to directly measure the AFM uniaxial anisotropy K_{AFM} by following the equation listed below.

$$H_{sf}^2 \approx 4K_{AFM}J \tag{2.13}$$

where J is the interatomic exchange which essentially given by the Néel temperature

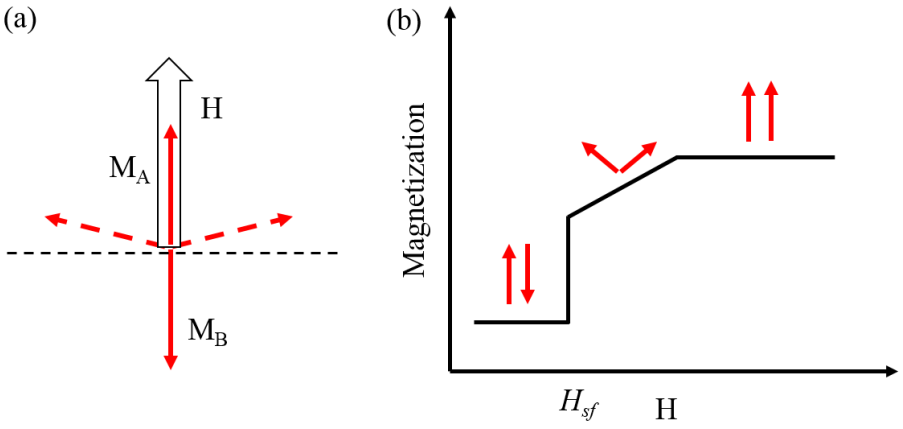

Figure 2-4 Spin-flop transition in antiferromagnets (a) sublattice magnetizations before (solid lines) and after spin flop process (dashed lines) in an external magnetic field that is parallel to the easy axis and (b) corresponding magnetization curve. Redrawn base on reference [2.3].

[2.8]. However, for many AFM materials, H_{sf} is as high as a few hundred teslas, which is extremely difficult to measure.

2.1.5 Exchange Bias

AFM material alone has little practical use due to the zero net magnetization. However, when it is adjacent to a FM layer, the exchange interaction between the AFM and the FM layers can greatly alter the magnetic properties of the FM layer. When an AFM/FM bilayer is cooled through the Néel temperature of the AFM layer in a magnetic field, the bilayer system exhibits a hysteresis loop shift which is normally referred as exchange bias [2.9, 2.10]. Figure 2-5 shows an example, where an exchange bias field of 83 Oe is induced through MA of a CoFe/CrPt bilayer structure. In most cases, an enhanced coercivity is also observed [2.11].

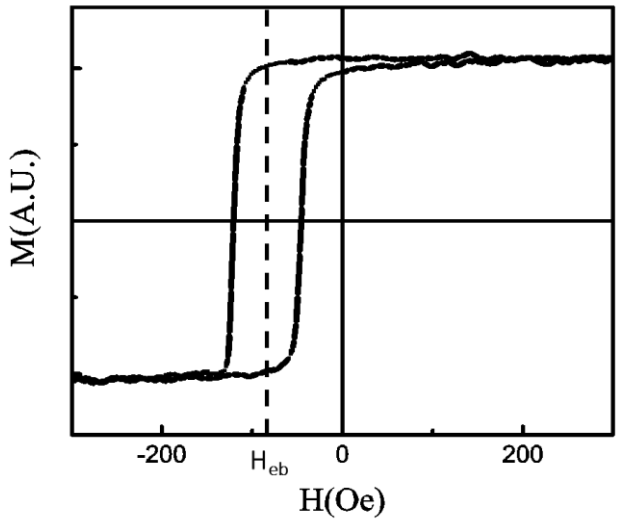

Figure 2-5 Hysteresis loop of a AFM-FM bilayer system (Si/ Ta/ $Co_{90}Fe_{10}$ / CrPt) after MA

Based on an early model [2.12], if the anisotropy of FM can be ignored, the energy area density in the exchange bias system can be written as

$$E = -HM_{FM}t_{FM}\cos\theta + K_{AFM}t_{AFM}\sin^2\theta - E_{eb}\cos\theta \tag{2.14}$$

where θ is the angle between the external field H and the FM magnetization $M_{FM,}$ t is the thickness for each layer and E_{eb} is the uniaxial anisotropy energy area density [2.13]. To minimize the energy, the following condition must be satisfied

$$\sin\theta\,(HM_{FM}t_{FM} + 2K_{AFM}t_{AFM}\cos\theta - E_{eb}) = 0 \tag{2.15}$$

Since the magnetization switching occurs at $\theta = \frac{\pi}{2}$ for coherent rotation, the switching field is equal to the exchange bias field H_{eb} [2.14].

$$E_{eb} = H_{eb}M_{FM}t_{FM} \tag{2.16}$$

This equation is commonly used to determine how effectively the AFM layer can bias the adjacent FM layer. It is important to have $E_{eb} \leq M_{AFM}t_{AFM}$ to observe the exchange bias field, otherwise, AFM spins would switch with the FM spin, and only the enhanced coercivity is observed [2.15]. This simple model can qualitatively explain what might cause the exchange bias but the estimation for the exchange bias field is several orders too high comparing with the experimental results [2.14]. Other considerations have been introduced to correct the problem, such as interface roughness, AFM thickness, grain size, crystallinity, AFM anisotropy and etc. [2.9]. Another assumption made by the model is uncompensated spins at the FM/AFM interface which play a key role in the exchange bias, since a fully compensated AFM interface, which has zero net magnetization, would lead E_{eb} to 0 [2.16].

Very strong exchange bias has been observed in systems containing $FeF_{2,}$ MnF_2 and FeMn, whose spin configurations are fully compensated at the interface [2.17-19]. This phenomenon can be explained by the spin-flop state of the AFM material which is

similar to what is shown in Figure 2-4(a), except that the FM spin antiparallel to the *H* [2.20]. The numerical micromagnetic calculations suggest that the spins of AFM and FM materials favors 90° alignment at the fully compensated interface [2.20]. During the magnetic cooling process, a parallel domain wall is formed in the AFM layer and stable due to the AFM anisotropy, which effectively pins the FM spin along the field cool direction [2.21]. Another calculation with a classical micromagnetic approach was also carried out on the same spin configuration, but only coercivity enhancement was obtained and the loop shift was not realized until uncompensated spins were introduced into the calculation [2.9, 2.19].

As described in Section 2.1.4, the anisotropy of the AFM is hard to observe directly in experiments. Alternative methods must be used by analyzing the change of FM layer magnetic properties with/without the AFM layers. One of the most commonly used methods to estimate the anisotropy of AFM is by using the following equation [2.3]

$$K_{AFM} = \frac{E_{eb}}{t_C} \tag{2.17}$$

where t_C is the critical thickness of AFM layer, above which the exchange bias is thermally stable. Like other properties associated with exchange bias system, the critical thickness is also system dependent as shown in Table 2-1. One major challenge faced by

Table 2-1 Critical thickness of a few AFM/FM exchange bias systems [2.1, 2.2]

.AFM/FM	t_C(ML)
CrPt/CoFe	40~45
MnPt/CoFe	35
MnPt/NiFe	45~50
MnIr/CoFe	15~25
MnIr/NiFe	20~30

Eq. 2.17 is that the E_{eb} is system dependent [2.22].

The influence of the crystallinity of the AFM layer also depends on the specific systems. For some systems, such as NiFe/NiO, the exchange bias is insensitive to the crystallinity of the AFM layer [2.23]. For other systems, such as CrPt/CoFe, the texture is the dominant factor for getting high exchange bias. In most cases, exchange bias increases with increasing texture for a single orientation systems [2.24], with only a few exceptions [2.9]. This could be due to the interface exchange energies are different for different crystallographic orientations. Crystallinity could also influence the formation of AFM domains and the anisotropy, changing exchange bias accordingly [2.25]. However, when a system involves more than one texture, exchange bias may change without following any particular trend [2.14]. It is also worthwhile mentioning that a well textured system could effectively decrease the roughness while a non-oriented system could strongly increase it [2.26]. Additionally, the most common way to introduce exchange bias is through MA. In many cases, the high temperature annealing would cause grain growth [2.1, 2.27] and recrystallization [2.24, 2.25] in both FM and AFM layers, drastically increase of surface roughness [2.28, 2.29] and interdiffusion at the FM/AFM interface [2.30]. All these changes could have great impacts on the magnitude of the interfacial exchange energy.

As mentioned above, an enhanced coercivity can also be observed in exchange bias systems. Many researches have suggested the enhanced coercivity might have a different origin than the exchange bias and is closer to the intrinsic properties of the AFM layer [2.31, 2.32]. For soft magnetic materials, such as Fe, the apparent anisotropy increase can

be viewed as the result of the AFM/FM interaction and the enhancement of the coercivity field is approximately equal to the anisotropy field introduced by the AFM layer [2.11].

2.2 Kondo Effect

2.2.1 Origin of Kondo Effect

When FM atoms are diluted inside a non-magnetic metallic matrix, the interactions between the magnetic impurities and surrounding conduction electrons become dominant at low temperatures. As shown in Figure 2-6(a), the resistance of such system shows a minimum which can be suppressed by an external magnetic field due to the split of the local spin degeneracy [2.33, 2.34]. The Kondo effect only arises when the impurities in

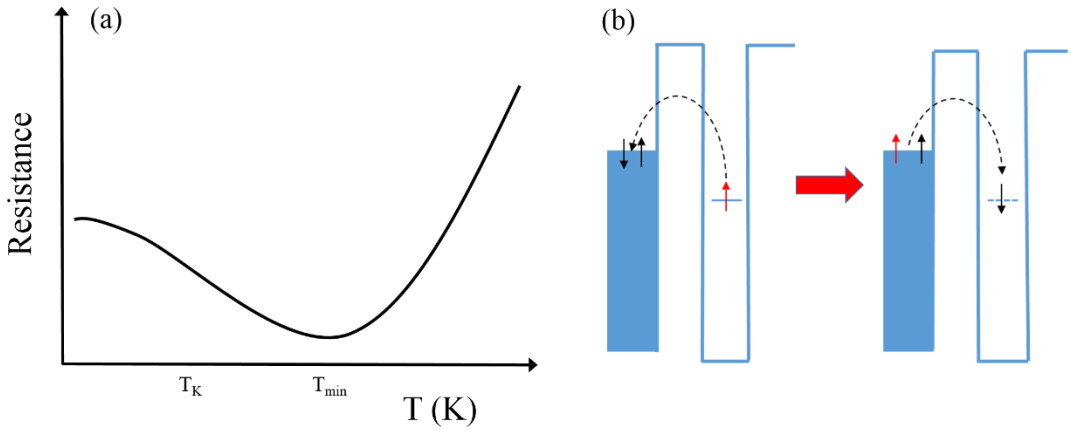

Figure 2-6 Kondo effect (a) resistance minimum and (b) atomic origin involving a spin-flip process of the impurity by the delocalized states of the conduction electrons.(blue)

the metal system are magnetic and does not require any kind of interactions between the magnetic impurities [2.34, 2.35]. The localized impurity spins are embedded in a conduction-electron sea where all the states with energy levels below the Fermi level are occupied [2.36]. The impurity electron with energy (E_0) is trapped below the Fermi level as shown in Figure 2-6(b). However, it can virtually hop into the conduction-electron sea

for a short period of time [2.34, 2.37]. Meanwhile, another electron near the Fermi level from the conduction-electron sea must hop into the impurity to occupy the empty state within that time frame. The tunneling electron can have the opposite spin configuration comparing with the previous electron [2.38]. This process, referred as spin-flipping, establishes a new state called Kondo resonance. This state is quite effective at scattering electrons near the Fermi level thus leads to the increase of the system resistivity.

2.2.2 Derivation of Resistivity Minimum

The derivation of the low temperature resistance minimum by Kondo starts with the Kondo Hamiltonian.

$$H = \sum_{k\sigma} \varepsilon_k c_\sigma^\dagger c_\sigma + JS \cdot s \tag{2.18}$$

where $c_\sigma^\dagger$ and c_σ are the creation and annihilation operator corresponding to the *k*-state spin with energy ε_k, and *J* is the exchange constant between impurity spin *S* and conduction electron spin *s* at the impurity site [2.39]. Through the second Born approximation and the assumption that localized spins are randomly oriented, the probability of impurity spin *k* transiting to a new state k' with the same polarization is given by

$$W(k \to k') = \frac{2\pi J^2 S(S+1)c}{3\hbar N}[2.1 + 4Jg(\varepsilon_k)]\delta(\varepsilon_k - \varepsilon_{k'}) \tag{2.19}$$

where c is the concentration and $g(\varepsilon) = \frac{1}{N}\sum_q \frac{f^0{}_q}{\varepsilon_q - \varepsilon_k}$ with $f^0{}_q$ being the Fermi distribution function for the electron with energy ε_q and *N* being the total number of electrons [2.39]. The probability of the spin-flip processes derived through similar process is equal

to $2W(k \to k')$. At finite temperature, the transport life time τ under an electric field $E_{\vec{x}}$ can be retrieved by calculating the rate of change of the probability due to the collision with the impurity spin [2.39].

$$\frac{1}{\tau_k} = \frac{3\pi z J^2 S(S+1)c}{2\hbar\varepsilon_F}[1 + 4Jg(\varepsilon_k)] \tag{2.20}$$

Since the conductivity $\sigma = \frac{ne^2\tau_k}{m_e}$, where n is the conduction-electron density, the resistivity contribution from the impurity spin scattering can be obtained from the following equation,

$$\rho_{imp} = \frac{1}{\sigma} = cA\left[1 - \frac{\hbar^2 J}{\pi m_e k_0}\int g(\varepsilon_k)\left(\frac{df^0}{d\varepsilon_k}\right)d^3k\right] \tag{2.21}$$

where $A = \frac{3\pi m_e J^2 S(S+1)}{2e^2\hbar\varepsilon_F n}$ is a constant [2.39]. By neglecting the higher order terms,

$$\rho_{imp} = cA\left(1 - \frac{3zJ}{\varepsilon_F}\ln\frac{T}{T_K}\right) \tag{2.22}$$

where T_K is defined as the Kondo temperature [2.39]. The total resistivity can be expressed as

$$\rho_{Total}(T) = const. + \rho_{pho}(T) + \rho_{imp}(T) \tag{2.23}$$

where $\rho_{pho}(T) = BT^5$ is the phonon contribution to the resistivity.[2.40] Since at low temperature, the phonon term can be neglected, $\Delta\rho(T) \approx \rho_{imp}(T)$. It can be seen that the logarithmic term comes from the calculation of the resistivity for the *s*-*d* exchange model to a higher order of *J* and reflects the sharpness of the Fermi level [2.41, 2.42]. This logarithmic behavior generally exists in all Kondo-effect-related parameters, such as

susceptibility, entropy and specific heat [2.41]. The above equation agrees with experiments very well except when $T \rightarrow 0$ where the resistivity deviates from the logarithmic behavior and approaches a constant [2.43]. This divergence at low temperature is commonly referred as the Kondo problem.

The Kondo problem was first solved by applying the NRG method by Wilson [2.44]. The idea is to rescale the energy level to eliminate high energy state and transform the Kondo Hamiltonian into a sequence of effective Hamiltonians which are valid over a reduced energy level [2.42, 2.44]. Wilson's calculation showed as $T \rightarrow 0$, the impurity spin is fully compensated by the screening cloud and the low temperature behavior of other parameters can be approached by similar methods [2.44, 2.45].

2.2.3 Kondo Screening Cloud

In the Kondo resonance state, the conduction electrons, surrounding the impurity, effectively form a singlet state while the other electrons behave like a free gas. It can be viewed as the formation of a Kondo screening cloud of itinerant spins screening the magnetic moment of the impurity [2.3]. As illustrated in Figure 2-7(a), the Kondo screening cloud has limited dimension within which the impurity spin is effectively antiferromagnetically coupled to the conduction electrons. It represents the distance that two electrons, near the Fermi level with energy difference of $k_B T_K$, can travel before their phases differ by π [2.46]. Using the RG method, the width in wave-vector, Δk_F can be express as

$$\Delta k_F = |k - k_F| = \frac{\Delta E}{\hbar v_F} \tag{2.24}$$

where ΔE is the width in energy and v_F is the Fermi velocity [2.47]. Therefore, the

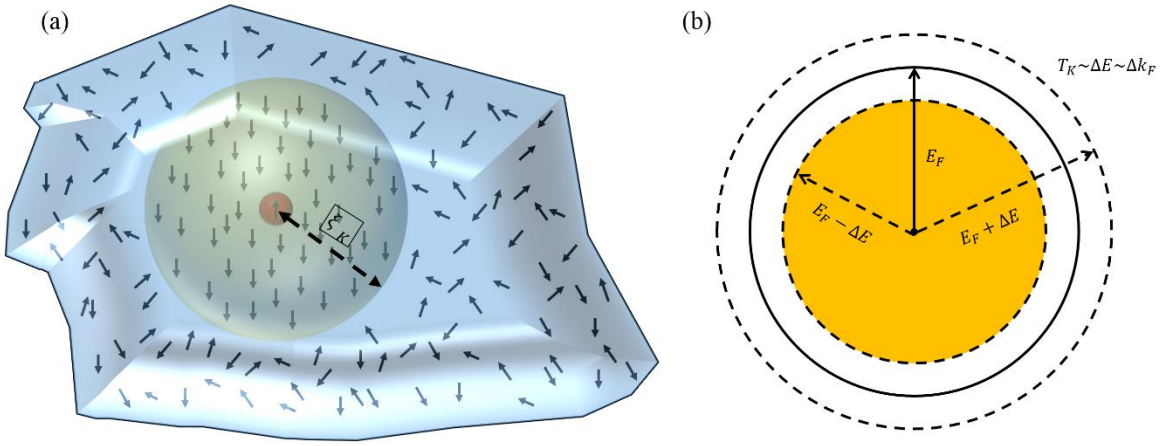

Figure 2-7 Schematic diagram of (a) Kondo screening cloud below the Kondo temperature. The big sphere represents the Kondo screening cloud while the blue area is the nonmagnetic metal host for the magnetic impurity (red) and (b) Kondo effect in k-space where the yellow area indicates full occupation by the conduction electrons.

Kondo coherence length (size of the Kondo screening cloud) is directly related to the Kondo temperature via $\Delta E = k_B T_K$ [2.48],

$$\xi_K = \frac{\hbar v_F}{k_B T_K} \tag{2.25}$$

where ξ_K is called the Kondo coherence length representing the radius of the Kondo screening cloud. As illustrated by Figure 2-7(b), the Kondo effect happens near the Fermi level with binding energy of T_K. If the Kondo temperature decreases, the associated Δk_F decreases as well. Table 2-2 lists Kondo temperatures for different systems [2.5]. Many factors can influence the Kondo temperature, such as external magnetic field, size of the system, presence of other interaction, etc. [2.34, 2.49, 2.50]. The Kondo coherence length ranges from a few nanometers to several micrometers for different systems and has not been observed experimentally [2.51, 2.52].

Table 2-2 Kondo temperature (K) for different bulk systems [2.5]

Host Impurity	V	Cr	Mn	Fe	Co	Ni
Cu	1000	2	0.01	30	500	>1000
Ag	-	0.01	$<10^{-6}$	5	-	-
Au	300	0.001	$<10^{-6}$	0.2	500	>1000
Mo	-	-	10	1	25	-
Rh	-	-	50	50	1000	-
Pd	-	100	0.01	0.02	0.1	-
Pt	-	200	0.1	0.3	1	-

2.2.4 Nanoscale Kondo Systems

When the dimension of the "box" containing the conduction electrons is reduced below the Kondo coherence length, the Kondo screening cloud can no longer extend to its full length inside the nonmagnetic host. However, as demonstrated in Figure 2-8(a), if the low-dimensional Kondo system (blue) is embedded in a metallic matrix, the Kondo screening cloud can still extend beyond the limit of the Kondo system into the hosting matrix. Therefore, there is strong hybridization between the conduction electrons of the Kondo system and the matrix, which not only blurs the distinction between bulk and

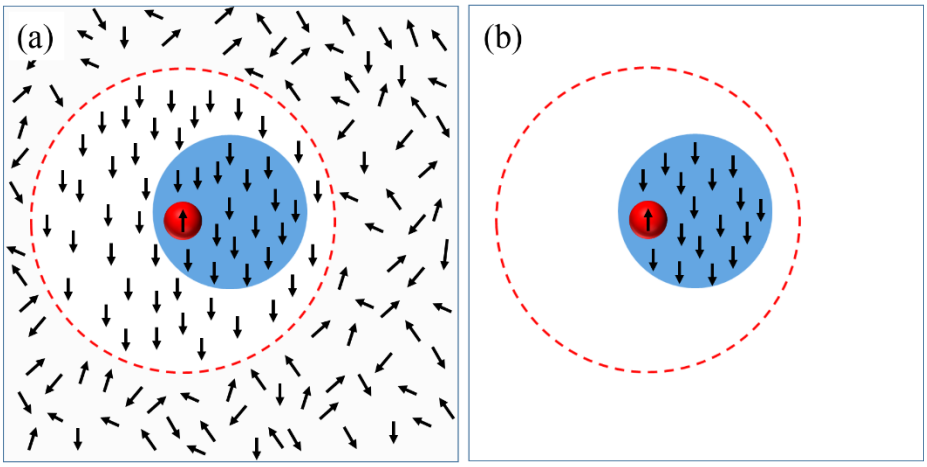

Figure 2-8 Low-dimensional Kondo systems inside (a) metallic matrix and (b) insulating matrix. Blue area represents the size of the Kondo system and dashed circle represents the supposed Kondo screening cloud

nanoscale Kondo system but also cause the Kondo screening cloud no longer well defined [2.41]. This complication can be avoided by using an insulating matrix instead of a metallic one as shown in Figure 2-8(b). Although the nature of the matrix would make it difficult to study the characteristic behavior of the resistivity of the Kondo system, the related magnetic properties can still be measured.

As illustrated in Figure 2-9, at high temperature, the magnetic susceptibility of the bulk Kondo system follows a paramagnetic-like behavior. In the vicinity of the Kondo temperature, the slope of the curve shows a strong reduction because of the establishment of the Kondo resonance and the magnetic susceptibility becomes constant when the Kondo screening cloud extends to its full length [2.53-55]. The nanoscale Kondo system

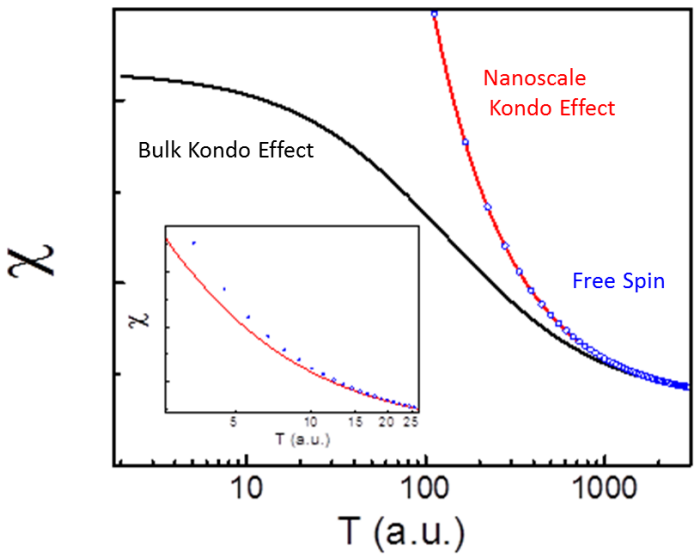

Figure 2-9 Schematic diagram of magnetic susceptibilities of free spin (blue dots) bulk (black line), nanoscale(red line) Kondo syste.

follows the similar route at the high temperature regime. However, it has been demonstrated that the reduction of the system size would greatly suppress the Kondo effect which yields a smaller Kondo temperature [2.56, 2.57].

Studies regarding thin-film Kondo systems reveal contradictory results [2.57-60]. Some found the Kondo effect in Cu(Fe) suppressed as the thickness of the film gets thinner and observed a reduced Kondo temperature [2.61], while others found an unchanged Kondo temperature in the same system [2.60]. This phenomenon might be caused by the interaction between magnetic impurities since the thickness dependence is closely related to the impurity concentration [2.58]. In the present thesis, we assume that the local moments are well-established and stable, in agreement with past research on Fe in Cu.

2.2.5 Ruderman-Kittel-Kasuya-Yosida (RKKY) Interaction

One complication of a dilute magnetic system is the interaction between different impurity spins, which goes beyond the Kondo effect in a narrower sense. When more than one magnetic impurities are present inside the system and their distance becomes close due to the impurity concentration, the Kondo resonance can still be established while the interactions between those impurities can no longer be ignored, among which is the RKKY interaction [2.41, 2.62, 2.63].

When the magnetic impurities are too far away to interact directly with each other, a long-range interaction can still occur through the surrounding conduction electrons. The effective coupling between the two magnetic impurities can be described using the following equation [2.8]

$$J_{ef} = J_o \frac{2k_F R\cos(2k_F R) - \sin(2k_F R)}{(2k_F R)^4} \tag{2.26}$$

where k_F is the Fermi wavevector and R is the distance between impurities. The Fermi wavevector is in the order of 0.1 nm^{-1}, therefore the sign of the effective interaction

oscillates on the scale of nanometers while the intensity falls off as R^{-3} [2.3] This type of interactions not only exist in atomic-scale but also encountered between thin film layers and embedded particles [2.8].

Analogously, both Kondo effect and RKKY interaction share a common origin which is the interaction between localized magnetic impurities and the free-electron sea. Regarding the Kondo effect, magnetic impurities are screened by the conduction electrons, which leads to the formation of the Kondo screening cloud. The RKKY interaction, on the other hand, effectively correlates the distant magnetic impurities and makes them more localized, namely difficult to be screened [2.50, 2.64]. The RKKY interaction can either be FM or AFM depending on the distance between magnetic impurities. The AFM interaction binds the two impurities into a singlet state ($S=0$) which greatly suppress the Kondo effect [2.65, 2.66]. The FM interaction, however, leads to a triplet state ($S=1$) which has a smaller Kondo temperature than systems without RKKY interaction [2.67].

2.2.6 Magnetic Pairs in Dilute Magnetic System

When the magnetic impurities are so close to each other, they can be considered as diatomic molecules. The forming of the pair is mainly the consequence of sample preparation process such as quench rate and cold work rather than the impurity concentration (c). It could exist in dilute magnetic system as low as 300 ppm [2.62].

For such system, single impurities and pairs co-exist with different Kondo temperature, namely T_{K_1} and T_{K_2} respectively. The total magnetization mainly contains two parts and can be written as $M = N_1M_1 + N_2M_2$ where M_1 and M_2 are the

magnetization associated with impurity singlet and pair and N_1 and N_2 are their total numbers respectively. Their contribution to the magnetic susceptibility can be expressed as

$$\chi = \frac{C_1}{T + T_{K_1}} + \frac{C_2}{T + T_{K_2}} \tag{2.27}$$

where $C_1 \propto c$, $C_1 \propto c^2$ [2.62].

Bulk samples containing magnetic pairs have been systematically studied previously. The sample was prepared through melting process of the magnetic impurity and its host. The analysis of the M-H curve reveal an S=3 behavior for the iron pairs [2.62].

2.3 Micromagnetism

Some of the researches that will be discussed in the following chapters involve magnetization phenomena on length scales of many interatomic distances, or at least several nanometers. It is commonly referred as micromagnetic phenomena and will be discussed in this section.

When the presence of magnetic moments inside the system becomes dominant, the direct interactions between magnetic moments and their surrounding lattices, such as dipolar interaction, exchange interactions, start to take the leading role in the determination of the magnetic properties of the system. Especially for the low-dimensional magnetic systems, the shape anisotropy induced by the reduced size of the system acts together with pre-existing interactions, which pushes the magnetic properties of the system away from their bulk counterparts. The competition between those

interactions under different conditions will ultimately determine the overall behavior of the low-dimensional magnetic system. The best way to analyze such competition is through analyzing the energy associated with each interaction as below.

$$E_{Sum} = \int \left\{ A\left[\nabla\left(\frac{M}{M_s}\right)\right]^2 - K_1\frac{(n\cdot M)^2}{{M_s}^2} - \mu_0 M\cdot H - \frac{\mu_0}{2}M\cdot H_d(M)\right\} dV \qquad (2.28)$$

Here A is the exchange stiffness, K_1 is the second-order uniaxial anisotropy, n is the unit vector along the easy-axis and $H_d(M)$ is the demagnetization field [2.68]. The above equation represents the summation of different micromagnetic energies including exchange energy, crystalline anisotropy energy, Zeeman energy and magnetostatic energy respectively. The sum of those energies has to be minimized for the system to stay in a magnetically stable state.

2.3.1 Magnetic Domain Formation

One main result of such competition is the form of magnetic domains. If only the exchange energy is considered inside a magnet, all the magnetic moments tend to align in the same direction which ends up with a single-domain configuration as shown in Figure 2-10(a). However, such configuration of magnetic moments only exists in very small particles. As the size of the particles increases, the magnetostatic energy becomes more significant. The magnetic moment configuration, shown in Figure 2-10(b), has much smaller magnetostatic energy which can be further lowered if a magnetic closure-domain is formed as shown in Figure 2-10(c). Although the exchange energy rises for such magnetic domain configuration, the overall energy is reduced and the system remains in an energy stable state. The competition between the exchange energy and magnetostatic energy can be characterized by the exchange length

$$l_{ex} = \sqrt{\frac{A}{\mu_0 M_s^2}} \tag{2.29}$$

where A is the exchange stiffness [2.8]. If the grain size of the specimen is below the

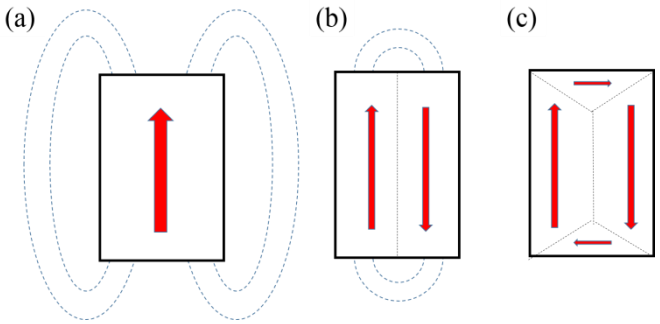

Figure 2-10 The magnetic flux of magnets with (a) single-domain, (b) two-domain and (c) closure-domain. Magnetostatic energy is the main driven force for the domain formation. Redrawn based on reference [2.4].

exchange length, systems, involving two magnetic phases with different anisotropies, would exhibit single-phase hysteresis loops. It also determines the transition from coherent rotation to curling [2.8].The scale of exchange length is typically around 10 nm.

Since the magnetization of (FM) materials tends to align along certain crystallographic direction, the magnetocrystalline energy also contributes to the configuration of domains due to the symmetry of crystal structures. For instance, the bcc iron has six equivalent easy axes, namely $\langle 100\rangle$,$\langle 010\rangle$, $\langle 001\rangle$, $\langle \bar{1}00\rangle$, $\langle 0\bar{1}0\rangle$, $\langle 00\bar{1}\rangle$. Due to the nature of their directions, it is possible to form the domain configuration as shown in Figure 2-10(c) which reduces not only the magnetocrystalline energy but also the magnetostatic energy.

2.3.2 Domain-Wall

The transition of the directions of magnetization is not atomically sharp between adjacent domains, which forms a region normally referred as domain wall. The two most encountered domain wall types are illustrated in Figure 2-11. It can be seen that the direct opposition of the magnetization of two domains would give rise to exchange energy which is in the order of $10^{-1}\,J\cdot m^{-2}$ at the interface [2.69].The energy rise can be reduced by gradually changing the magnetization direction over a certain distance. Therefore, the exchange energy prefers wide domain walls and large domain sizes.

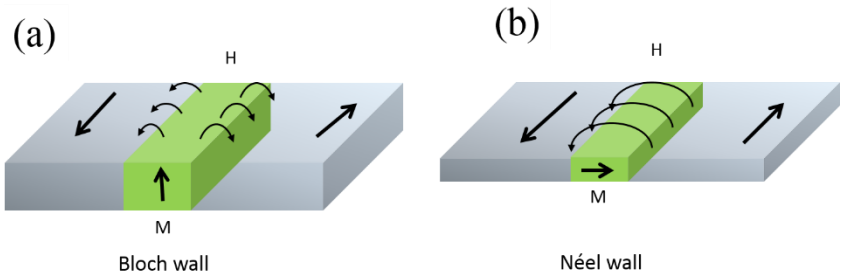

Figure 2-11 Schematic diagram of the stray field from (a) Bloch wall (thickness > 20nm) and (b) Néel wall (thickness <20nm)

However, such wide domain wall would cause the magnetization to deviate from the easy axes of the specimen and give rise to magnetocrystalline energy. Minimizing such energy requires large domain size and narrow domain walls. Therefore the domain wall thickness is determined by the competition between exchange energy and magnetocrystalline energy. In the case of simple uniaxial materials, the magnetocrystalline energy can be expressed as

$$E_{ex} = K_1 \sin^2(\theta) \tag{2.30}$$

where K_1 is the anisotropy constant. The domain wall width has the form of

$$\delta_o = \sqrt{\frac{A}{K_1}} \tag{2.31}$$

and varies from a few nanometers to several hundred nanometers [2.8].

For 180° Bloch wall, Eq. 2.31 can be refined as $\delta_B = \pi\sqrt{\frac{A}{K_1}}$ [2.8] and the domain wall energy density for a Bloch wall is $\gamma_B = 4\sqrt{AK_1}$ which is on the order of 1 $mJ \cdot m^{-2}$ [2.69]. A Néel wall, on the other hand, can only occur in a thin-film system where the thickness of the film is much less than the width of the domain wall. The expression of the domain-wall width and domain-wall energy density are $\delta_N \approx \pi\sqrt{\frac{2A}{K_1}}$ and $\gamma_N \approx 4tM_s$ respectively, where *t* is the thickness of the thin film [2.69].

2.3.3 Magnetization Reversal

When an external magnetic field is applied to a magnetic material with multi-domain structures, a pressure is applied to the domain wall. As illustrated in Figure 2-12, the initial closure domain yields a zero net magnetization and the easy axis of the specimen is slightly off the direction of the external magnetic field. As the field increases, the domain wall starts to migrate in such a way that the domain with magnetization closest to the field direction starts to expand. The change in Zeeman energy of the domain wall is

$$E_{Ze} = -2\mu_0 M_s H x L^2 \tag{2.32}$$

where x is the domain wall position and L^2 is the effective domain-wall area [2.70]. Therefore the total energy of the domain wall is

$$E_{wall} = \gamma(x)L^2 + E_{Ze} \tag{2.33}$$

Once the whole specimen is occupied by such domain state, the magnetization starts to rotate away from its easy axis and further align with the external field.

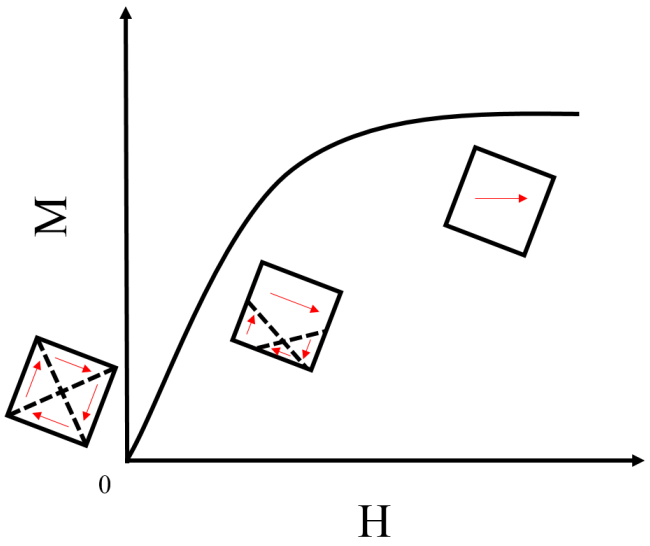

Figure 2-12 Evolution of magnetic domains of a FM material under external magnetic field. The magnetic field is deviated from the easy axis by a small angle. Redrawn base on reference [2.4].

Without the influence of defects, the domain wall motion is highly reversible. However, there is always some kind of distribution of defects in the magnetic systems. When the domain wall encounters a defect, if the domain wall energy is higher when it is around the defect, the defect serves as a barrier for the domain wall motion. On the other hand, if the domain wall energy is lower when it is around the defect, the domain wall is trapped by the defect [2.4]. When the size of the defect is comparable to the size of the domain wall, it will effectively pin the domain wall at its location until the Zeeman energy is large enough to overcome its effect. The pinning effect is also related to the contrast of K_1 or A between the defect and the bulk, for instance, voids have $K_1 = A = 0$.

The domain wall motion around defects is the major contribution to the irreversibility of a magnetic system.

To understand the mechanism of the magnetization reversal, several models have been proposed. The Stoner-Wohlfarth (SW) model basically considers only the coherent rotation of the magnetization. Its energy normally involves two terms which are the uniaxial anisotropy energy and Zeeman energy

$$E_{SW} = K_u \sin^2\theta - \mu_0 M_s H \cos(\alpha - \theta) \tag{2.34}$$

where $K_u$is the sum of all anisotropies and α is the angle between the anisotropy axis and applied field direction [2.71]. During a magnetization reversal process, it tends to follow a path which would minimize E_{SW}. The SW model can be used to describe the magnetization reversal in thin films by adding a shape anisotropy term, $2\pi M_s^2(N_\perp - N_\parallel)\sin^2\theta$, in the total anisotropy form where $N_\perp$ and $N_\parallel$ are demagnetization factors perpendicular and parallel to the *z-axis* [2.71]. To simplify the problem, take $\alpha = 0$ and analyze the stability of E_{SW} for small θ where $\sin\theta \approx \theta$ and $\cos(\theta) \approx 1 - \frac{\theta^2}{2}$. The above equation for E_{SW} can be written as

$$E_{SW} = \left(K_u + \frac{\mu_0 M_s H}{2}\right)\theta^2 + \mu_0 M_s H \tag{2.35}$$

The coercivity field is corresponding to the transition of the system from a stable energy minimum to an unstable maximum and satisfies the following expression [2.8]

$$H_c = \frac{2K_u}{\mu_0 M_s} \tag{2.36}$$

Despite its limitation in describing the non-coherent rotation process and magnetization reversal behavior in multi-domain structures, the SW model offers a simple approximation for other models of granular materials that deal with hysteresis [2.71, 2.72].

2.3.4 Superparamagnetism

A multi-domain structure is not an energy favorable state if the particle size is less than the critical single domain radius [2.8]

$$R_{sd} \approx \frac{36\sqrt{AK_1}}{\mu_o M_s^2} \tag{2.37}$$

It forms a single-domain state instead; for instance, the critical single domain radius for Fe is around 10 nm [2.3]. The particle undergoes either coherent rotation or nucleation with the presence of defects under an external magnetic field [2.73]. However, further reducing the particle size would cause the magnetic moments to jump between two different stable orientations of the magnetizations under the influence of ambient thermal energy [2.74]. Therefore, although the magnetization is mostly uniform over the particle volume, the average magnetization over time is zero above its blocking temperature. The volume of the particle can be estimated using

$$V_o \approx \frac{25k_B T_B}{K_1} \tag{2.38}$$

where T_B is the blocking temperature [2.75], which can be retrieved by analyzing the ZFC/FC curve as shown in Figure 2-13. In order to measure the ZFC curve, the system is firstly cooled down without the presence of the external magnetic field. Upon reaching the desired temperature, a small magnetic field is applied and magnetic susceptibility is

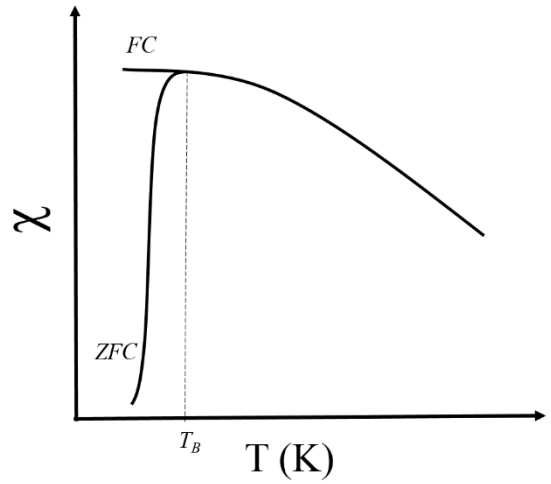

Figure 2-13 ZFC/FC measurement of superparamagnetic system with blocking temperature T_B

measured as a function of rising temperature. The magnitude increases initially since the increasing thermal energy slowly frees the spins from their frozen state and allows them to align with the external magnetic field. After reaching the blocking temperature of the system, the thermal energy outweighs the Zeeman energy, which cause the magnetic susceptibility drops with further increasing temperature. On the other hand, the FC measurement requires the system to be cooled in the presence of an external magnetic field. Due to the magnetic history of the system, the magnetic susceptibility remains a constant upon passing the blocking temperature. The *M-H* curve of such system exhibits a Langevin behavior and has no coercivity above the blocking temperature.

2.4 References

[2.1] B. Dai, J. W. Cai, W. Y. Lai, Y. K. An, Z. H. Mai, F. Shen, Y. Z. Liu, and Z. Zhang, Appl. Phys. Lett. **87**, 092506 (2005).

[2.2] C. Mitsumata, A. Sakuma, K. Fukamichi, M. Tsunoda, and M. Takahashi, J. Phys. Soc. Jpn. **77** (4), 044602 (2008).

[2.3] J. M. D. Coey, *Magnetism and magnetic materials*. (Cambridge University Press, Cambridge, 2010), p.614.

[2.4] N. A. Spaldin, *Magnetic materials: fundamentals and applications*, 2nd ed. (Cambridge University Press, Cambridge ; New York, 2011), p.274.

[2.5] H. Ehrenreich, F. Seitz, and D. Turnbull, *Solid State Physics: Advances in Research and Applications*. (Academic Press, New York, 1969).

[2.6] B. D. Cullity and C. D. Graham, *Introduction to magnetic materials*, 2nd ed. (IEEE/Wiley, Hoboken, N.J., 2009), p.544.

[2.7] M. Niemeyer, K. Hirsch, V. Zamudio-Bayer, A. Langenberg, M. Vogel, M. Kossick, C. Ebrecht, K. Egashira, A. Terasaki, T. Möller, B. v. Issendorff, and J. T. Lau, Phys. Rev. Lett. **108,** 057201 (2012).

[2.8] R. Skomski, *Simple models of magnetism*. (Oxford University Press, Oxford ; New York, 2008), p.349.

[2.9] A. E. Berkowitz and Kentaro Takano, J. Magn. Magn. Mater. **200** (1–3), 552 (1999).

[2.10] S. H. Chung, A. Hoffmann, and M. Grimsditch, Phys. Rev. B **71** (21), 214430 (2005).

[2.11] R. Zhang, R. Skomski, X. Z. Li, Z. Li, P. Manchanda, A. Kashyap, R. D. Kirby, S. H. Liou, and D. J. Sellmyer, J. Appl. Phys. **111**, 07D720 (2012).

[2.12] W. H. Meiklejohn and C. P. Bean, Phys. Rev. **105** (3), 904 (1956).

[2.13] W. H. Meiklejohn, J. Appl. Phys. **33** (3), 1328 (1962).

[2.14] J. Nogués and Ivan K. Schuller, J. Magn. Magn. Mater. **192** (2), 203 (1999).

[2.15] X. Y. Wang, H. Wang, H. W. Jiang, P. J. Wang, and J. L. Wang, J. Nanosci. Nanotechno. **12** (2), 1032 (2012).

[2.16] M. Kiwi, J. Magn. Magn. Mater. **234** (3), 584 (2001).

[2.17] T. Mewes, B. Hillebrands, and R. L. Stamps, Phys. Rev. B **68**, 184418 (2003).

[2.18] J. Nogues, T. J. Moran, D. Lederman, I. K. Schuller, and K. V. Rao, Phys. Rev. B **59** (10), 6984 (1999).

[2.19] A. L. Dantas, L. L. Oliveira, M. L. Silva, and A. S. Carrico, J. Appl. Phys. **112**, 073907 (2012).

[2.20] N. C. Koon, Phys. Rev. Lett. **78** (25), 4865 (1997).

[2.21] D. Mauri, E. Kay, D. Scholl, and J. K. Howard, J. Appl. Phys. **62** (7), 2929 (1987).

[2.22] O. V. Billoni, S. A. Cannas, and F. A. Tamarit, J. Phys.: Condens. Matter **23**, 386004 (2011).

[2.23] M. Pakala, Y. Huai, G. Anderson, and L. Miloslavsky, J. Appl. Phys. **87** (9), 6653 (2000).

[2.24] Yukio S., Teruyasu M., Fumiyasu O., Masatada Y., Takahisa Y., and Yuichi I., Appl. Phys. Lett. **84** (26), 5311 (2004).

[2.25] A. N. Dobrynin, D. N. Ievlev, K. Temst, P. Lievens, J. Margueritat, J. Gonzalo, C. N. Afonso, S. Q. Zhou, A. Vantomme, E. Piscopiello, and G. Van Tendeloo, Appl. Phys. Lett. **87** (1), 012501 (2005).

[2.26] De-Hua Han, Jian-Gang Zhu, Jack H. Judy, and John M. Sivertsen, J. Appl. Phys. **81** (1), 340 (1997).

[2.27] Y. F. Li, John Q. Xiao, and D. V. Dimitrov, J. Appl. Phys. **91** (10), 7227 (2002).

[2.28] P. Wisniowski, T. Stobiecki, J. Kanak, G. Reiss, and H. Bruckl, J. Appl. Phys. **100** (1), 013906 (2006).

[2.29] Geoff A., Yiming H., and Lena M., J. Appl. Phys. **87** (9), 6989 (2000).

[2.30] J. H. Lee, H. D. Jeong, C. S. Yoon, C. K. Kim, B. G. Park, and T. D. Lee, J. Appl. Phys. **91** (3), 1431 (2002).

[2.31] A. Tillmanns, S. Oertker, B. Beschoten, G. Guntherodt, C. Leighton, I. K. Schuller, and J. Nogues, Appl. Phys. Lett. **89**, 202512 (2006).

[2.32] R. Morales, Z. P. Li, J. Olamit, K. Liu, J. M. Alameda, and I. K. Schuller, Phys. Rev. Lett. **102**, 097201 (2009).

[2.33] D. Giuliano, B. Jouault, and A. Tagliacozzo, Phys. Rev. B **63**, 125318 (2001).

[2.34] L. Kouwenhoven and L. Glazman, Physics World **14** (1), 33 (2001).

[2.35] J. Kondo, J. Phys. Soc. Jpn. **74** (1), 1 (2005).

[2.36] S. Amasha, A. J. Keller, I. G. Rau, A. Carmi, J. A. Katine, Hadas Shtrikman, Y. Oreg, and D. Goldhaber-Gordon, Phys. Rev. Lett. **110**, 046604 (2013).

[2.37] R. Skomski, J. Phys.: Condens. Matter **19**, 315202 (2007).

[2.38] R. M. Potok, I. G. Rau, Hadas Shtrikman, Yuval Oreg, and D. Goldhaber-Gordon, Nature **446** (7132), 167 (2007).

[2.39] J. Kondo, Prog. of Theor. Phys. **32** (1), 37 (1964).

[2.40] T. A. Costi, L. Bergqvist, A. Weichselbaum, J. von Delft, T. Micklitz, A. Rosch, P. Mavropoulos, P. H. Dederichs, F. Mallet, L. Saminadayar, and C. Bauerle, Phys. Rev. Lett. **102**, 056802 (2009).

[2.41] R. Skomski, R. Zhang, P. Kharel, A. Enders, S. H. Liou, and D. J. Sellmyer, J. Appl. Phys. **107** (9), 09E126 (2010).

[2.42] A. C. Hewson, *The Kondo problem to heavy fermions*. (Cambridge University Press, Cambridge; New York, 1993), pp. 444.

[2.43] J. Kondo, P. Jpn. Acad. B-Phys. **82** (9), 328 (2006).

[2.44] K. G. Wilson, Rev. Mod. Phys. **47** (4), 773 (1975).

[2.45] H. R. Krishnamurthy, K. G. Wilson, and J. W. Wilkins, Phys. Rev. Lett. **35** (16), 1101 (1975).

[2.46] M. A. Blachly and N. Giordano, Phys. Rev. B **51** (18), 12537 (1995).

[2.47] I. Affleck, in *Perspectives of Mesoscopic Physics*, edited by Ora Entin-Wohlman and Amnon Aharony (World Scientific Publishing Co. Pte. Ltd., Singapore, 2010), pp. 1.

[2.48] G. Bergmann, Phys. Rev. B **77** (10), 104401 (2008).

[2.49] Y. Meir and N. Wingreen, Phys. Rev. B **50** (7), 4947 (1994).

[2.50] P. Knake and A. Chudnovskiy, arXiv preprint arXiv:0905.4392 (2009).

[2.51] J. Park, S. S. B. Lee, Y. Oreg, and H. S. Sim, Phys. Rev. Lett. **110** (24) (2013).

[2.52] I. Affleck, László Borda, and Hubert Saleur, Phys. Rev. B **77** (18), 180404 (2008).

[2.53] Y. M. Hou, D. Jin, F. M. Yang, Q. Z. Ran, Y. P. Wang, Z. J. Chen, and Y. S. He, Chin. Phys. Lett. **15** (2), 131 (1998).

[2.54] A. Yaouanc, P. Dalmas de Réotier, P. Bonville, G. Lebras, P. C. M. Gubbens, A. M. Mulders, and S. Kunii, Europhys. Lett. **47** (2), 247 (1999).

[2.55] R. Troć, R. Andruszkiewicz, R. Pietri, and B. Andraka, J. Magn. Magn. Mater. **183** (1–2), 132 (1998).

[2.56] R. Zhang, T. A. George, P. Kharel, R. Skomski, and D. J. Sellmyer, J. Appl. Phys. **113** (17), 17E148 (2013).

[2.57] S. Mishra, S. Bose, P. Vasa, and P. Ayyub, Phys. Rev. B **71**, 094429 (2005).

[2.58] P. J. Silverman and C. V. Briscoe, Phys. Rev. B **15** (9), 4336 (1977).

[2.59] S. N. Mishra, S. K. Mohanta, S. M. Davane, N. Kulkarni, and Pushan Ayyub, Phys. Rev. Lett. **105** (14) (2010).

[2.60] M. A. Blachly and N. Giordano, Phys. Rev. B **49** (10), 6788 (1994).

[2.61] G. Apostolopoulos and C. Papastaikoudis, Solid State Commun **99** (4), 277 (1996).

[2.62] J. M. Franz and D. J. Sellmyer, Phys. Rev. B **8** (5), 2083 (1973).

[2.63] C. Kittel, *Introduction to solid state physics*, 8th ed. (Wiley, Hoboken, NJ, 2005), p.680.

[2.64] W. T. Herrera, Y. T. Xing, S. M. Ramos, P. Munayco, M. B. Fontes, E. M. Baggio-Saitovitch, and F. J. Litterst, Phys. Rev. B **84** (1), 014430 (2011).

[2.65] A. Crépieux and C. Lacroix, Phys. Rev. B **59** (21), 13824 (1999).

[2.66] M. T. Tran and K. S. Kim, J. Phys.: Condens. Matter **23**, 425602 (2011).

[2.67] H. B. Heersche, Z. de Groot, J. A. Folk, L. P. Kouwenhoven, H. S. van der Zant, A. A. Houck, J. Labaziewicz, and I. L. Chuang, Phys. Rev. Lett. **96** (1), 017205 (2006).

[2.68] R. Skomski, J. Phys.: Condens. Matter **15** (20), R841 (2003).

[2.69] R. C. O'Handley, *Modern magnetic materials: principles and applications*. (Wiley, New York, 2000), p.740.

[2.70] R. Skomski, M. L. Yan, Y. F. Xu, and D. J. Sellmyer, IEEE Transl. J. Magn. Jpn. **43** (6), 2163 (2007).

[2.71] C. Tannous and J. Gieraltowski, Eur. Phys. J. D **29** (3), 475 (2008).

[2.72] S. H. Charap and A. Ktena, J. Appl. Phys. **73** (10), 5818 (1993).

[2.73] G. P. Zhao, X. L. Wang, Y. P. Feng, and C. W. Huang, IEEE T. Magn. **43** (6), 2908 (2007).

[2.74] C. L. Dennis, R. P. Borges, L. D. Buda, U. Ebels, J. F. Gregg, M. Hehn, E. Jouguelet, K. Ounadjela, I. Petej, I. L. Prejbeanu, and M. J. Thornton, J. Phys.: Condens. Matter **14** (49), R1175 (2002).

[2.75] R. Zhang, R. Skomski, X. Yin, S. H. Liou, and D. J. Sellmyer, J. Appl. Phys. **107**, 09E710 (2010).

Chapter 3 : Sample Fabrication and Characterization Methods

In this chapter, the main focus is on various experimental techniques that are used in this study. It can be divided into two groups, sample fabrication, including a home-made magnetron sputtering system, a home-made cluster deposition system, an AJA deposition system, annealing system, and sample characterization, including X-Ray Diffractometer (XRD), Scanning Electron Microscope (SEM), Transmission Electron Microscopy (TEM), Alternative Gradient Force Magnetometer (AGFM) Superconducting Quantum Interference Devices (SQUID), Physical Property Measurement System (PPMS) and high-temperature resistance measurement system (HTRMS). Many systems have more than one functionality depending on the setup; however, only the core principle and functions that are directly related to the project will be discussed here.

3.1 Magnetron Sputtering

A sputtering process describes the phenomenon that energetic particles constantly bombard the surface of a solid and cause atoms of the solid to be removed during the process. The sputtering process with the assistant of magnetron cathodes is called magnetron sputtering which is widely used in both scientific and industrial fields [3.1].

3.1.1 Magnetron Sputtering Principle

Inert gases, such as Argon (Ar), are ionized through natural cosmic radiation. Under the influence of the electric field, those ions bombard the target surface and emit secondary electrons which ionize more inert gas particles through electron-atom collision process. The effectiveness of this process depends on the mass, energy and angle of

incidence of inert gas ions as well as the mass, surface binding energies, crystallinity and orientation of the crystallinity of the target [3.2].

Another important factor is the deposition rate. It determines how fast the sputtered specimen can be condensed on a substrate. It is directly related to the available inert gas ions and the mean free path of the sputtered atoms. Naturally, increasing the gas pressure would certainly increase the availability of ions; however, it would also greatly decrease the mean free path of the sputtered atoms and leads to a drop of sputtering rate. In a magnetron sputtering process, as shown in Figure 3-1, under the Lorentz force, electrons are confined near the target surface, which greatly increases the chance of its collision

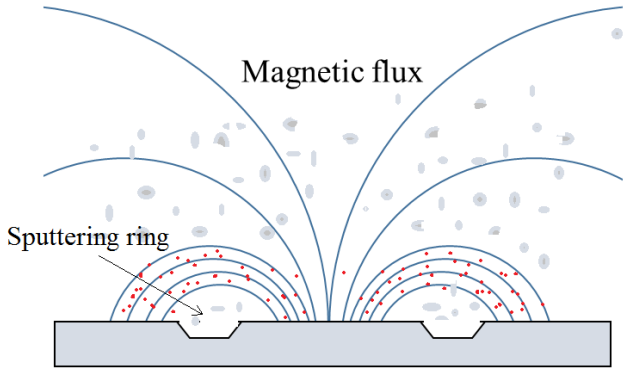

Figure 3-1 Schematic diagram of the relation between sputtering ring and target surface flux distribution in magnetron sputtering process. Red dots are the electron trapped by magnetic flux.

with inert gas particles [3.3]. This allows the sputtering to happen at a relatively low gas pressure while still yields a reasonable deposition rate. The drawback is the target material utilization because the sputtering is now determined by the magnetic flux distribution on the target surface as well. Consequently, the bombardments would occur in those target surface areas showed in Figure 3-1. In most cases, only 30% of the target material can be used for the magnetron sputtering process [3.4].

For a composite target, a stoichiometric sputtering can be established only after initial pre-sputtering process and with sufficient cooling to the target [3.2]. The composition of the deposited film could be slightly different from the composition of the target and may change if the deposition conditions, such as power, inert gas pressure, are altered [3.1]. In this regard, for composition-sensitive materials such as $L1_0$ phase FePt and CrPt, it is important to establish a fixed deposition condition and monitor their stoichiometry carefully.

In most cases, increasing the sputtering power and/or decreasing the inert gas pressure will lead to an increase in sputtering rate, as demonstrated in Figure 3-2. However, achieving high deposition rate is not always that straightforward. As discussed above, high target temperature which is induced by high sputtering power could change

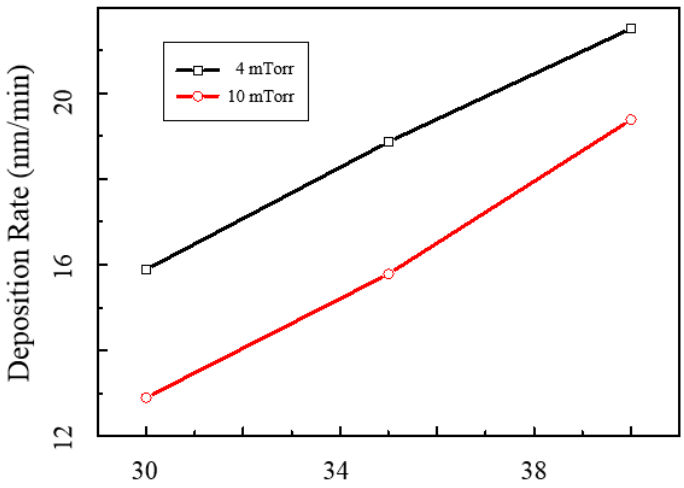

Figure 3-2 Sputtering power dependence for NiMn under different inert gas pressures. Plasma cannot be ignited when the pressure is less than 3 mTorr

the stoichiometry of the deposited film causing a depth profile inside the sample over the deposition period, which, in most cases, is not desired. Figure 3-2 also shows the decrease of inert gas pressure would increase the sputtering rate; however, certain gas

pressure is still required in order to maintain sustainable plasma near the target surface. For instance, most insulator targets and magnetic targets require high gas pressure (over 30 mTorr) and high sputtering power (50~120 W) to ignite the plasma while other metallic targets can start as low as 10 W with 3 mTorr gas pressure. The source-substrate distance is another key factor for controlling the sputtering rate and the further apart of the source and substrate are, the lower the sputtering rate is. In some cases, low sputtering rate is desired, for instance, to achieve a uniform deposition over a large area, to lower the energy of sputtered atoms, and etc.

3.1.2 Radio Frequency (RF) Magnetron Sputtering

For most metal targets, the electric field can be supplied using a direct current (DC) power supply and the corresponding sputtering process is called DC magnetron sputtering. However, for insulating/dielectric targets, the positive charges would build up on the target surface and prevent further bombardment from happening. In this situation, a RF power supply along with a RF matching box is used. The reflected power can be minimized through impedance match and the alternative potential on the target surface could maintain the bombardment from inert gas ions while preventing the surface from building up charges. One of the disadvantages of RF magnetron sputtering is the slow deposition rate, which makes depositing thick films time-consuming. Another disadvantage is that the poor thermal conductivity of the target can cause heat accumulation in the target and eventually a thermal gradient over the vertical distance. The uneven thermal expansion could fracture the target over long deposition time.

As described in the previous sections, the sputtering process is greatly influenced by the magnetic flux configuration on the target surface. Figure 3-3 shows the surface

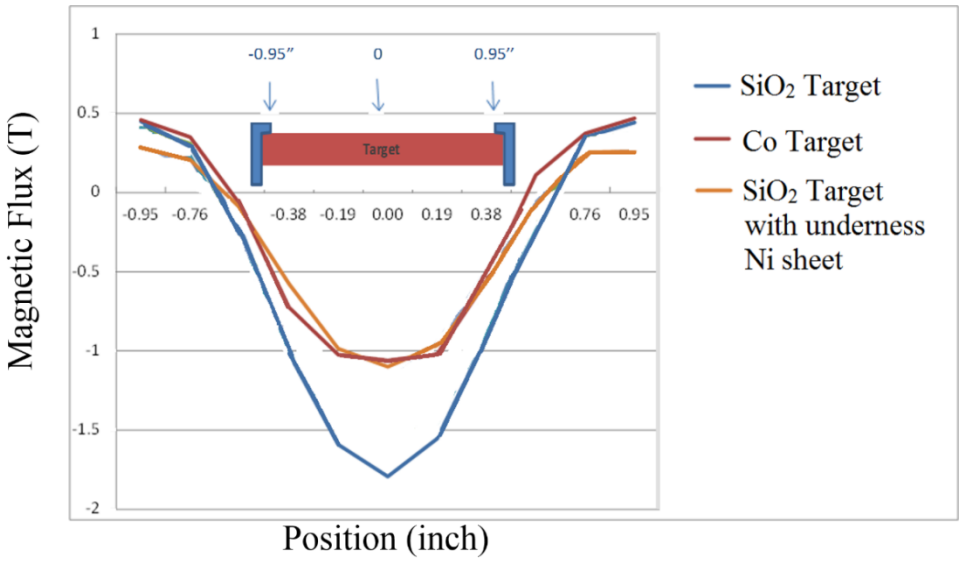

Figure 3-3 Magnetic flux distribution on different target surfaces. The difference could alter the shape and size of the sputtering area.

magnetic flux distribution for different targets. The magnetic flux at the surface of a magnetic target is much lower comparing with a non-magnetic target due to flux trapping. This effect leads to significant size and shape differences regarding the sputtering areas, especially for RF magnetron sputtering process. It can be seen from Figure 3-4 that the SiO_2 film deposited using RF magnetron sputtering without using the nickel underneath

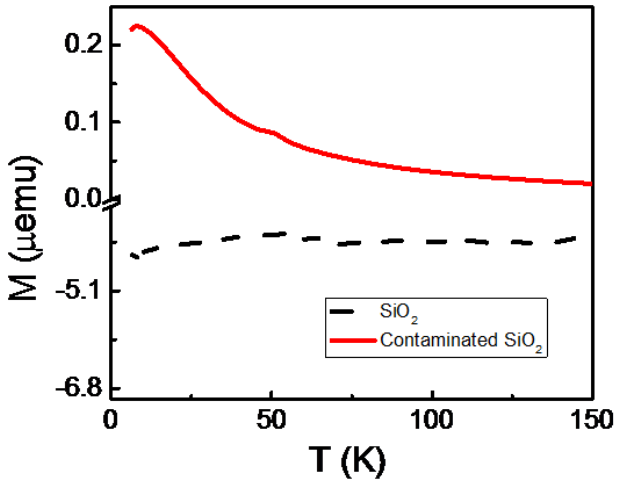

Figure 3-4 Temperature dependent magnetization of SiO_2 thin film deposited without (solid line) and with (dashed line) underneath nickel sheet. Diamagnetic behavior suggests the elimination of magnetic contamination.

sheet shows magnetic signal originated from the magnetic impurities inside the cathode of the sputtering gun. The magnetic flux distribution can be adjusted by introducing underneath magnetic sheets as demonstrated in Figure 3-3. Once the magnetic flux distribution of the SiO_2 target become similar to that of Co target, the deposited SiO_2 film shows only diamagnetic signals, as shown in Figure 3-4.

3.1.3 Home-made Cluster Deposition System

The cluster deposition system utilizes the principle of low-energy cluster beam deposition technique which allows the generated clusters to land onto the substrate without fragment upon impact [3.5]. The diameter of clusters varies from a few nanometers to tens of nanometers and normally follows a Gaussian distribution [3.6, 3.7].

As shown in Figure 3-5, the cluster deposition system mainly contains two parts, the gas-aggregation chamber and the deposition chamber. The gas-aggregation chamber

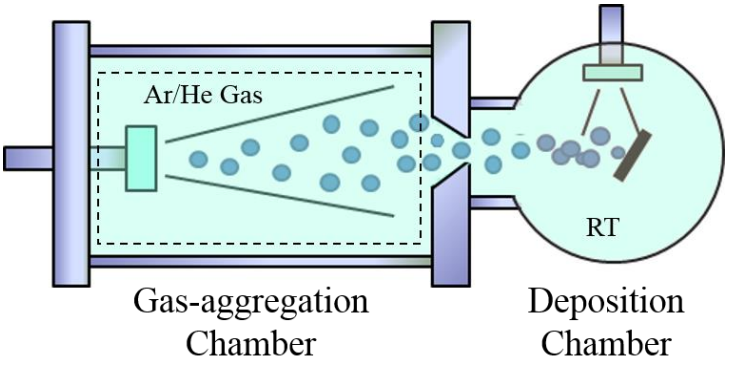

Figure 3-5 Schematic diagram of the home-made cluster deposition system. The inner chamber is illustrated using dashed line. Co-sputtering of the cluster and matrix can be achieved.

is operated under constant cooling by either water or liquid N_2. A mixture of Ar and He gases, acquired by controlling the flow rate of each gas, is introduced directly onto the surface of the three inch target. The constant flowing of the gas not only supply the gas

particles for ionization but also prevent small chips from building up on the target surface which could in time short the sputtering gun.

The sputtered atoms, generated through DC magnetron sputtering process, undergo interatomic collisions with cooled He atoms and among themselves [3.8]. This process greatly reduces the kinetic energy of the sputtered atoms allowing them to condense and form clusters. A high Ar pressure will increase the sputtering rate at the target surface and eventually increase the probability of the interatomic collisions [3.9, 3.10]. The He partial pressure can be used to control the cluster size, for instance, decreasing the Ar/He ratio would generally reduce the size of clusters [3.6]. Normally, the cluster will continue to grow through cluster-cluster collisions and atomic vapor condensation until it leaves the gas-aggregation chamber. It is driven through a small aperture due to the pressure difference between the gas-aggregation chamber and the deposition chamber [3.8]. Clusters can be collected in the depostion chamber where a two inch magnetron sputtering gun can be used to provide cover/matrix layer for the clusters.

The deposition rate of clusters is monitored in the deposition chamber by a quartz crystal thickness monitor. The rate can be control by changing the sputtering power, Ar/He ratio and source-aperture distance. Those factors are also crucial parameters for determination of cluster sizes. Other influential factors include target composition and topography. Therefore, it is recommended to monitor the sputtering rate of the cluster throughout the deposition process.

In principle, cluster size can be control by changing the sputtering power, Ar/He ratio, gas temperature and source-aperture distance. However, achieving a desired combination of deposition rate and cluster size is very complicated, mainly because

changing any of the parameters would have a direct impact on both of them. For instance, increasing the sputtering power would almost certainly increase the deposition rate, but it could also shift the cluster size distribution to a larger size. The size distribution can be measured by TEM as shown in Figure 3-6. Table 3-1 shows the cluster size difference for

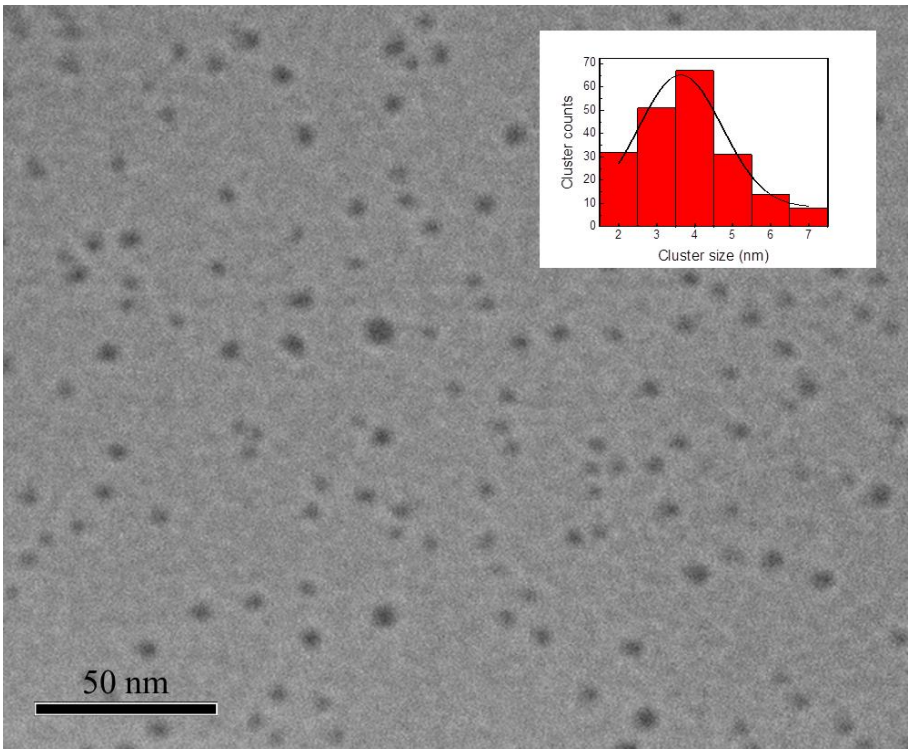

Figure 3-6 TEM measurement for C1. Most clusters are well-separated from each other. The inset is the cluster size distribution.

different deposition conditions. For clusters deposited under liquid N_2 cooling, drastically changing the sputtering power from 18 W to 40 W would greatly increase the average cluster diameter from 4 nm to 29 nm while small increase from 15 W to 18 W yields little difference. The Ar/He ratio also plays an important role and particularly, Ar flow rate less than 100 ccpm normally yields zero sputtering rates. Clusters deposited with water cooling normally requires more sputtering power to achieve similar sputtering rate as the one cooled by liquid N_2 and the average size of the cluster is also much bigger. Since it is

Table 3-1 Cluster size for different deposition conditions

ID	Ar:He	Gun to Aperture (cm)	Power (W)	Average Cluster Size (nm)	Inner Chamber Temperature (K)	Sputtering Rate (Å/sec)
C1	1	20	18	4	<137	0.2
C4	1	20	40	29	<137	0.2
C5	1.5	20	15	6	<150	0.2
D4	1.5	20	18	6	<150	0.2
C3	1.5	20	34	20	300	0.2

beneficial to have small cluster size for the investigation described in Chapter 4, deposition condition C1 was used.

Cu(Fe)/SiO_2 stack structure is achieved by alternating deposition from the 3 inch Cu(Fe) cluster source and 2 inch SiO_2 source. The separation of the cluster is important since adjacent clusters would effective increase the size of the confined system and lead to inconsistency in the sample. When it comes to estimate the amount of clusters being deposited, the term nominal thickness is used. It reflects the value when the volume of the deposited cluster is divided by the area of the substrate. Figure 3-7 shows the relation

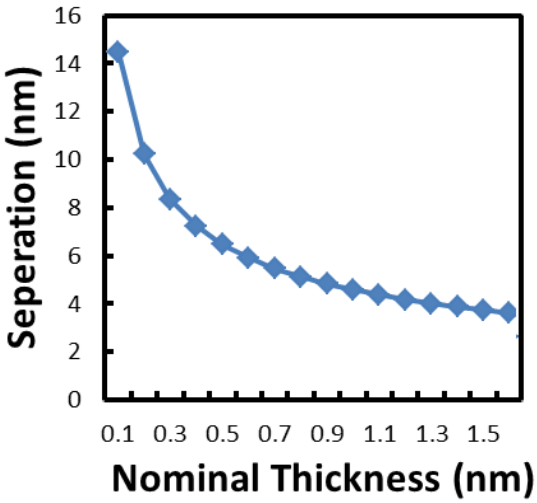

Figure 3-7 The cluster separation variation of 5 nm diameter Cu(Fe) clusters regarding cluster nominal thickness

between cluster separation and continuous deposition. Since it is desired to have cluster separated, the nominal thickness of 2 Å is commonly used in stack structure. As shown in Figure 3-5, co-sputtering of the cluster and matrix material can be achieved by tilting the sample 20º from the cluster incidence. This greatly reduced the sample preparation time and improves the sample consistency comparing with samples with the stack structure.

3.1.4 Home-made Magnetron Sputtering System

Our home-made magnetron sputtering system has a base pressure of 10^{-7} Torr and is equipped with four sputtering guns. Each gun can be connected to either a DC or RF power supply depending on the target attached and operate independently. Up to eight samples can be prepared with one pumping cycle, which would greatly improve the sample consistency. A sample cover is also installed to protect samples that are not being sputtered. Although sputtering guns have to be turned on manually, both the sample holder and sample cover can be controlled by a computer through two stepping motors which can further increase the consistency between samples by eliminating human error. Another advantage of this system is the flexibility. Replacing the multi-sample holder and sample cover with other attachments would allow us to deposit thin films under different conditions, such as high temperature deposition, deposition under a magnetic field and uniform wafer-size deposition.

This is the main sample fabrication system in the study described in Chapter 5. The multi-sample holder configuration is used and the deposition condition for each target is listed in Table 3-2. The deposition rate is measured by micro-balancer method and the thickness of each layer is controlled by varying the deposition time. At least one mutual

configuration was used for samples prepared in different pumping cycles to check the consistency between each series.

Table 3-2 Sample preparation condition for Chapter 5

Target	Power Supply	Power (W)	Gas Pressure (mTorr)	Distance (cm)
CoFe	DC	30	5	4
NiFe	DC	30	5	4
CoFeB	DC	30	5	4
MgO	RF	60	10	11
Fe:SiO_2	RF	60	10	5

3.1.5 AJA Magnetron Sputtering System

This is a commercially available system from AJA International, INC.. The system mainly contains three parts, deposition chamber, loading lock and control rack. Up to four different targets can be attached to the sputtering guns inside the deposition chamber. The sample holder is installed on the ceiling of the chamber and can be transferred to the loading lock without breaking the vacuum in the deposition chamber. A lamp heater is attached on the back of the sample hanger and can heat the sample holder up to 1100 K. The sputtered atoms land on the substrate with certain incident angle which can be adjusted by the node underneath the sputtering gun which manually tilts it to different angles. Samples with wedge structures can be made with angled deposition. Uniformity over large area, as illustrated in Figure 3-8, can be achieved by rotating the substrate holder with 37 rpm. The sample rack inside the loading lock can hold up to six different sample holders. Once the sample holder is loaded inside the deposition chamber, the sputtering process is fully automated through a Labview program. Samples with multi-layer structure can be easily prepared through proper programing.

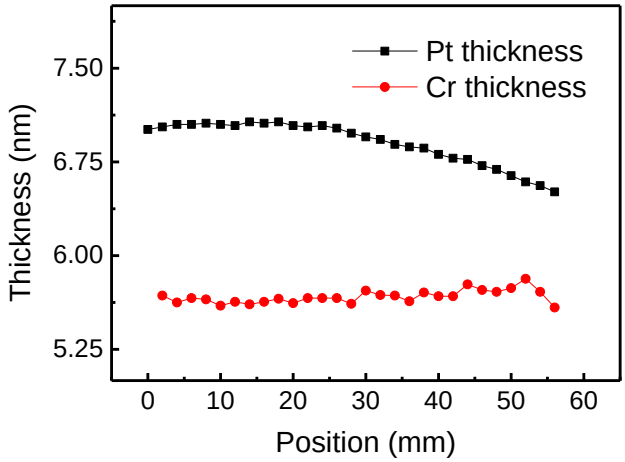

Figure 3-8 Thickness variation of Cr and Pt thin films over large distance deposited by AJA magnetron sputtering system.

This system is mainly used in the experiments described in Chapter 6. The sample holder was kept rotating for all depositions except the wedge structure. The deposition rate and thickness variation of the wedge structure were measured by XRR method. The CrPt composition is controlled by the deposition time which is fine-tuned by EDX. Unless mentioned otherwise, all samples are prepared at RT. Table 3-3 lists typical deposition condition for this project.

Table 3-3 Sample preparation condition Chapter 6

Target	Power Supply	Power (W)	Gas Pressure (mTorr)	Deposition Rate (nm/min)
Cr	DC	36	5	1.1
Fe	DC	59	5	1.0
Pt	RF	36	5	1.0
SiO_2	RF	60	3	1.2

3.2 Sputtering Target Preparation

Most magnetron sputtering targets are commercially available; however, for targets that require specific composition, it is sometimes efficient and cost-effective to prepare targets locally.

3.2.1 Sintered Composite Target

Fine powders of different materials with purity of 99.99% or higher are uniformly mixed and grinded together. The amount of materials is based on calculation for different compositions and target sizes. The mixture is then poured into a cylinder die and pressed by a pneumatic press for several hours. Upon finished, the target will be transferred into a high temperature furnace and sintered under an Ar/H_2 forming gas environment for up to eighteen hours. The forming gas is mainly to recover or prevent the target oxidation. The temperature should be set as high as possible yet not exceeding the melting point of any of the involved elements. The major advantage of this method is the uniformity of the composition throughout the target. However, the prepared targets would normally have a smaller density (less than 80%) comparing with alloy targets and are very fragile. The dimension of the target could not be precisely controlled either, due to the nature of the sintering process and the composition is fixed for each target. Targets, including CoFeB and CoFe used in Chapter 5, were prepared using this method.

3.2.2 Target with Chips Attached

As discussed in section 3.1, only certain area of a target is sputtered during the magnetron sputtering process. For a round shape target, it would form a circular ring on the target surface and is commonly referred as the sputtering ring. Therefore, by putting chips of different materials onto those sputtering ring, thin film or clusters with different composition can be prepared.

As shown in Figure 3-9, the designed Fe concentration for the deposited thin film can be estimated using the area ratio of the two materials on the sputtering ring, which in this case is 0.3 at. %. The chip is either commercially available or can be made by arc

melting. The advantage of this approach is the flexibility of composition control and easy manufacture. However, the disadvantage is pronounced as well. The composition of the deposited film cannot be precisely controlled because, as mentioned in previous sections,

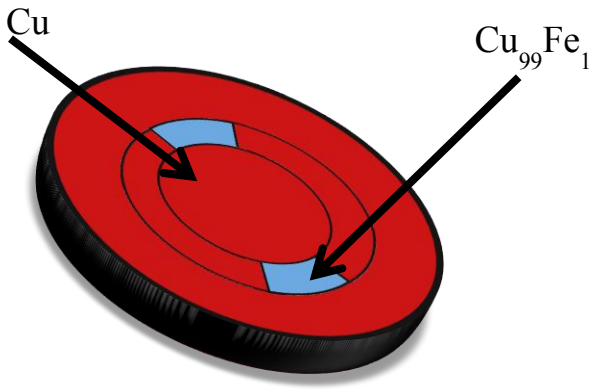

Figure 3-9 A schematic diagram of a Cu target with Cu(Fe) chip attached the center ring represents the sputtering ring. The composition of the target is determined by the area ratio of the chips and the rest of the sputtering ring.

different materials have different sputtering rate. Even when the stoichiometry of the sputtering becomes constant for one set of sputtering condition, it may vary when the sputtering condition is changed. The situation worsens when there is magnetic material involved. The sputtering process not only changes the topographic of the target but also alters the magnetic flux distribution near the magnetic material which would lead to a depth profile inside the deposited thin film especially for long time deposition and create inconsistencies among different samples. Therefore, the stoichiometry of the prepared sample has to be monitored closely.

3.3 Thermal Annealing System

Thermal annealing is a form of heat treatment which involves heating the specimen to a specified temperature for a specified period of time and then cooling either naturally

or at a controlled speed. The purpose of the process varies with different systems. It can be used to remove internal stresses and instabilities, to alter electrical and magnetic properties, to refine the crystalline structure, to remove gases, or to produce a definite micro-structure [3.11]. Through optimizing the annealing process, specimens with a specified composition and microstructure can be archived. The CA and RTP were mainly used to achieve $L1_0$ phase CrPt and MA was used to introduce unidirectional anisotropy in exchange bias system. Ar/H_2 forming gas was used for all annealing process to prevent/recover from oxidation.

3.3.1 Conventional Annealing (CA)

The conventional annealing system usually implies a relatively slow heating and cooling process. There are three stages in the annealing process, namely recovery stage, recrystallization stage, grain-growth stage [3.12]. During the recovery stage, crystal defects and internal stresses of the specimen is removed. This stage can occur at a relative low temperature. During the recrystallization stage, new grains start to nucleate and grow to replace those deformed by internal stresses. The temperature that is required for this stage is largely related to the amount of deformations and chemical impurities inside the specimen [3.13]. Once recrystallization is completed, grain growth will occur by absorbing nearby grains and the size of the grain is related to both the annealing temperature and time. Annealing occurs by the diffusion of atoms within a specimen towards its equilibrium state. Heat is needed to increase the rate of the diffusion process by providing the energy needed to break and form new boundaries. The process can be carried in high vacuum or in gas environments such as H_2, O_2, Ar, etc.. The ramping

speed used in this study was approximately 30 K per sec and the annealing time is around 5 hours before naturally cooled down to RT.

3.3.2 Rapid Thermal Annealing (RTA)

The RTA is similar to CA except that the heating is normally done within several seconds and has a relatively short annealing time. The rapid increasing of temperature blurs boundary of the recovery stage and recrystallization stage and allows them to happen at the same time. The strain introduced by the former would have great influence on the latter [3.14]. The short annealing time would minimize the grain growth stage which yields small grain sizes and surface roughness comparing with CA [3.15, 3.16]. The RTA used in this study has a typical ramping speed of 100 K per second with constant Ar/H_2 forming gas flow. The annealing time is 5 min at temperature up to 1073 K and then cooled down to RT within 10 min.

3.3.3 Magnetic Annealing (MA)

The only difference between MA and other annealing methods mentioned above is the presence of magnetic field during the annealing process. It is widely used as a process to introduce induced magnetic anisotropy in FM material and exchange bias in AFM/FM bilayer structures. It not only influences the magnetic properties of the material but may also change its texture and microstructure [3.17]. The MA used in this study has a similar ramping/cooling speed as the CA. The annealing time is less than one hour and the maximum external field is 10 kOe.

3.4 X-Ray Diffraction

X-rays are electromagnetic radiation which can be produced by striking a solid target with rapidly moving charged particles, such as electrons [3.18]. Its wavelength can be estimated by $\lambda\,(\text{Å}) = \frac{hc}{E} = \frac{12.39\ keV\cdot\text{Å}}{E}$. It can be seen that, for x-rays with energy higher than a few *keV*, its wavelength is comparable with the typical interatomic distance in solids (a few Å). Therefore it can be used for crystal structure analyses through reinforced diffraction pattern.

3.4.1 X-Ray Diffractometer (XRD)

When a beam of x-rays strikes a crystalline sample, it interacts with electronic shells of atoms in the sample. It will either be transmitted, in which case it will continue along its original path, or it will be scattered by the electrons of those atoms in the material [3.19]. All the atoms in the path of the x-ray beam scatter x-rays. In most cases, the scattered waves interfere destructively with each other, with the exception of special orientations where Bragg's law is satisfied.

Figure 3-10 shows an ideal situation where a parallel x-ray beam, with incident angle of θ, is diffracted by a crystal lattice separated by a distance *d*. The two outgoing beams can be completely in phase only if their path difference is equal to an integer (*n*) multiple the wavelength (λ), $n\lambda = 2d\sin(\theta)$. This relation is known as Bragg's law which is the foundation of X-ray diffraction analysis. Bragg's law does not only apply to adjacent crystal planes and can be generalized using Miller indices (hkl) $n\lambda = 2d_{hkl}\sin(\theta_{hkl})$, where d_{hkl} incorporates higher orders of diffraction i.e. n greater than 1.

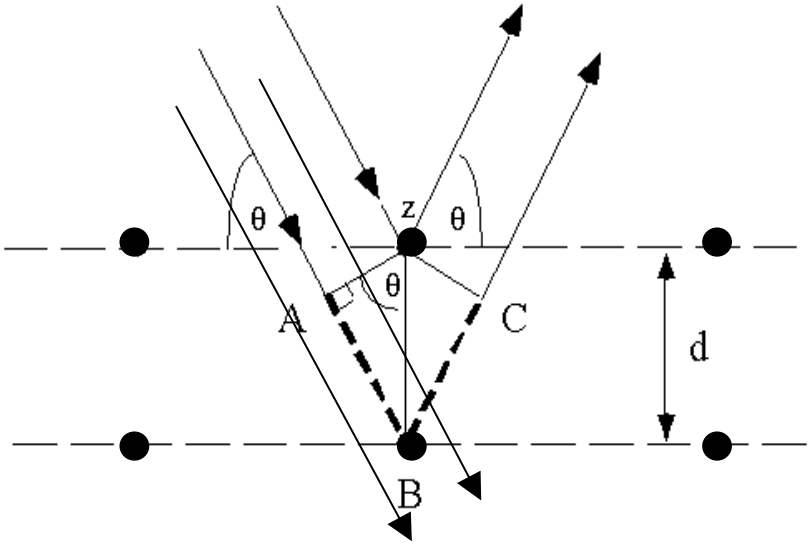

Figure 3-10 Schematic diagram of XRD process where θ is the incident angle and d is the lattice spacing

The angle between the transmitted and Bragg diffracted beams is always equal to 2θ as a consequence of the geometry of the Bragg condition. Therefore, for a thin film sample, a coupled θ-2θ measurement is used to achieve the x-ray diffraction pattern. By carefully analyzing the x-ray diffraction pattern, information such as crystal orientation, interplanar spacing, lateral grain size, crystallinity, crystal phase, stress, and etc., can be retrieved.

3.4.2 X-RAY Reflectometry (XRR)

Similar to XRD, when X-ray beam encounters an interface from two materials, due to the change of refractive index, part of the beam is reflected and will interact constructively if the Bragg's law is satisfied. The incident angle has to be small enough so that the reflection can be treated classically [3.20].

The XRR measures the intensity of x-rays reflected from an interface as a function of incident angle. For a single layer film, the reflected intensity oscillates and if the

difference between the two reflected waves is a multiple of the incident wavelength (λ), the maximum of intensity appears.

$$m\lambda \approx 2d_1\sqrt{\theta_i^2 - 2\delta_1}, m = 0,1,2... \quad (3.1)$$

where d_1 is the layer thickness, θ_i is the incidence angle, and δ_1 is the parameter of dispersion. For multilayer structures, however, it becomes much more complicated since it involves the contributions from all layers. In order to characterize the multilayer structure, simulation software Leptos from Bruker AXS, can be used. This software can easily build up layer structures from the substrate to the capping layer. By carefully adjusting parameters of each layer, such as thickness, roughness, density of each material, it can generate a simulation curve which will match the measured curve from XRR. Through this process, the previous mentioned parameters can be estimated. Figure 3-11 shows a typical XRR measurement and its simulation curve which yields a thickness of

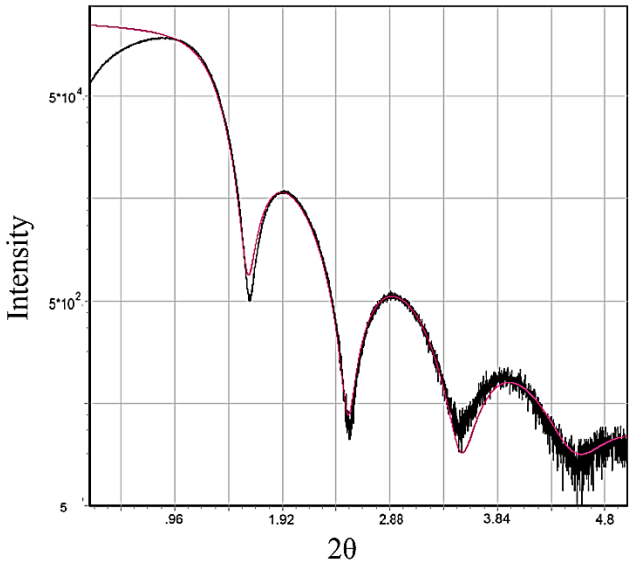

Figure 3-11 XRR measurement (black) and simulation curve (red) for Pt thin film. The fitting would reveal information such as film thickness, roughness and density, etc.

7.79 nm and 0.53 nm surface roughness. The range for all measurement was fixed from 0.1° to 5° with an interval of 0.005° measured at 0.2°/min.

3.4.3 Rigaku D/Max-B (Rigaku) & Bruker-AXS D8 Discover (Bruker)

Both systems can function as XRD and XRR. The Rigaku is simple to operate and uses Co K_α radiation (λ = 0.1790 nm) which is suitable for ferruginous samples. The Bruker, on the other hand, uses Cu K_α radiation (λ = 0.1541 nm) and can offer a better resolution with proper setups. Its sample holder offers more flexibility in sample mounting and allows sample size larger than one inch. The Bruker also provides more functionality with different attachment options, such as sample heater, general area detector diffraction system (GADDS), and etc.

3.5 Electron Microscope (EM)

Figure 3-12 shows the signals that can be emitted due to interactions between beam

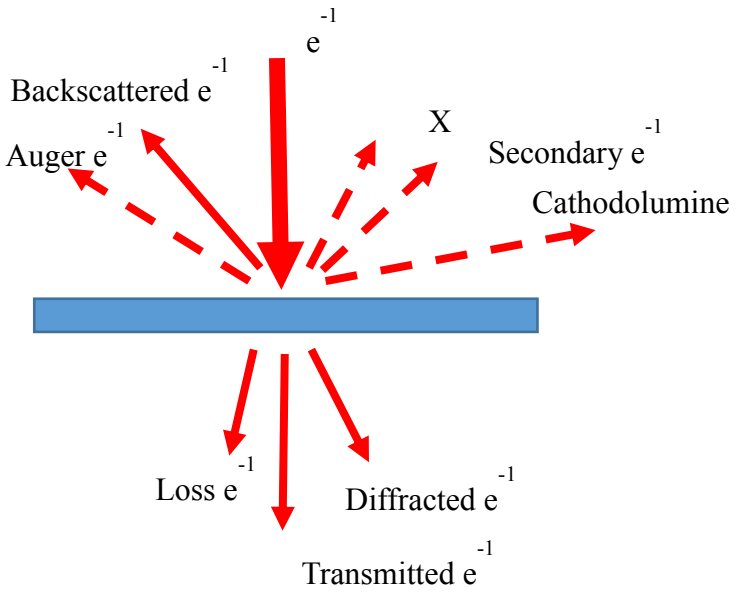

Figure 3-12 Schematic diagram of signals emitted from specimens due to interaction with beam electrons, which are used in different characterization tools.

electrons and the specimen [3.21, 3.22]. All these signals carry certain information about the specimen and can be used for characterization. The EM has been demonstrated to be a powerful tool when it comes to studying the microscopic features of all kinds of specimens. It utilizes the electron beam to illuminate the subject of interest and provides images with extremely high magnification which is several orders beyond the reach of any optical microscope. There are several different types of EMs depending on the signal it collects and uses for analysis, among which, TEM and SEM are used in this study.

3.5.1 Transmission Electron Microscopy (TEM)

TEM is the first type of EM that was developed around 1930s [3.23]. It can create high resolution images by letting a high voltage electron beam (200 kV for JEOL 2010 TEM) pass through the specimen.

Once the electron beam is created from the source chamber, it is converged and filtered by a series of apertures and electromagnetic/electrostatic lenses. The main purpose is to acquire a broad parallel electron beam with defined energy [3.23]. The beam then goes through the thin specimen while being scattered. There are mainly two scattering processes. One is the inelastic scattering which is caused by the interaction between beam electrons and the orbital electrons of the specimen atoms. It leads to a small deviation from the original path of the beam and generate a continuous background noise. On the contrary, the elastic scattering is due to the interaction between beam electrons and the nuclei of the atoms in the specimen. It, along with the un-scattered beam electron, is the main source to the TEM image. The image is then projected onto a fluorescent screen or CCD camera after focused by projection lenses. For crystalline specimen, the most important scattering is due to the Bragg diffraction. Since the

wavelength of the electron used in TEM is much smaller than the wavelength of x-ray and can operate on a smaller area, it can offer much more detailed information regarding the crystallinity of the specimen compared with XRD.

As mention above, the specimen measured by TEM must be really thin (100nm or less) to allow the electron beam to pass with minimized inelastic scattering. It can be realized by depositing samples directly onto a TEM grid. This method works well for cluster samples; however, most thin film samples require specific substrates to grow on in order to achieve certain properties. In this case, the substrate has to be thinner through a series of polishing processes. Firstly, it should be carefully polished with different grade of sand papers and then milled using our precision ion polishing system.

3.5.2 Scanning Electron Microscope (SEM)

Similar to the TEM, SEM also utilizes electrons to create images. The emitted electron beam is refined by a series of apertures and electromagnetic/electrostatic lenses. However, the beam is focused on the specimen surface instead of transmitting through it [3.22]. This is a crucial step for SEM because the resolution of the image is typically related to the final spot size. The beam then scans along a pattern of parallel lines. During the scanning, the electron beam can penetrate up to several micrometers into the specimen depending on the beam setup and specimen type. The interactions between the beam electrons and electrons in the specimen cause the emission of secondary electrons near the sample surface. These secondary electrons are then collected by an electron detector and their intensity distribution is plotted on the screen to form a SEM image [3.21]. Therefore, the brightness of the image is directly related to the number of secondary electrons that can be detected. A steep surface tends to have a shorter escape

distance for secondary electrons and make them easier to emit from the surface which ultimately leads to a brighter image comparing with a flat surface. This allows the SEM to produce three-dimensional apparent image for the specimen [3.21]. Since most secondary electrons are originated from a few nanometers from the surface, the image can be used to analyze the morphology of the specimen [3.22, 3.24].

3.5.3 Energy-Dispersive X-ray Spectroscopy (EDX)

It can be seen from Figure 3-12, for all EM system, there is also x-ray emissions, which are originated from the inelastic scattering of the beam electrons when interacting with the electrons of specimen atoms [3.25]. During the interaction, an inner shell electron from the atom is ejected. The vacancy left behind is then filled by an outer shell electron and an x-ray or Auger electron will be emitted during the process [3.22]. The energy of the x-ray is characteristic to each element inside the specimen. It carries rich information regarding the sample composition and can be detected by an EDX system. Chemical elements starting with atomic number 6 can be identified with this method [3.22]. Hence, the morphology and composition information can be obtained simultaneously which grants us the ability to map the element distribution of the specimen.

3.6 Alternative Gradient Force Magnetometer (AGFM)

AGFM uses an alternating gradient field to produce a periodic force on a sample that is placed in a variable/static DC field. Samples are mounted on an extension rod attached to a piezoelectric unit and experience an alternating force due to the alternating field gradient. The amount of the force is proportional to the magnitude of the gradient field, the magnetic moment of the sample and the intensity of the applied field. The

resulting deflection of the extension rod is transmitted to the piezoelectric sensing unit and is proportional to the total moment of the sample [3.26]. The output from the piezoelectric unit is detected synchronously at the operating frequency of the gradient field using a lock-in amplifier. Since the signal developed by the piezoelectric unit is greatly enhanced by operating at or near the mechanical frequency of the assembly, a tuning process is necessary to counter the mass change between different samples [3.27]. One major concern about the AGFM is the magnetic gradient field during the measurement. It can cause errors for soft magnetic materials when their coercivity is the same order of magnitude as the gradient field [3.26], which in our system is 4 Oe, 0.4 Oe and 0.04 Oe respectively. Alternative measurement method must be considered.

Magnetic fields, as high as 13 kOe, can be applied by our AGFM system (Princeton Measurements Micromag 2900) and the field direction can be either parallel or perpendicular to the sample surface depending on the probe used. The sample size can be as large as 5 mm x 5 mm x 2 mm. For samples with good signal noise ratio, the whole hysteresis loop can be measured less than one minute which is very fast comparing with other techniques such as VSM or SQUID. As the magnetic moment approaching the sensitivity of the system (10 μemu), the averaging time of the measurement must be increased at least 5 times in order to obtain analyzable data.

3.7 Superconducting Quantum Interference Devices (SQUID)

SQUID is one of the most sensitive techniques for magnetic measurements. It can measure very small changes in magnetic flux even when a large magnetic static field is presented.

Figure 3-13 shows a schematic diagram of a SQUID magnetometer. Pick-up coils, including two end coils and one central coil, are connected in such a way that the induced current due to magnetic flux change in each coil would be accumulated to enhance the

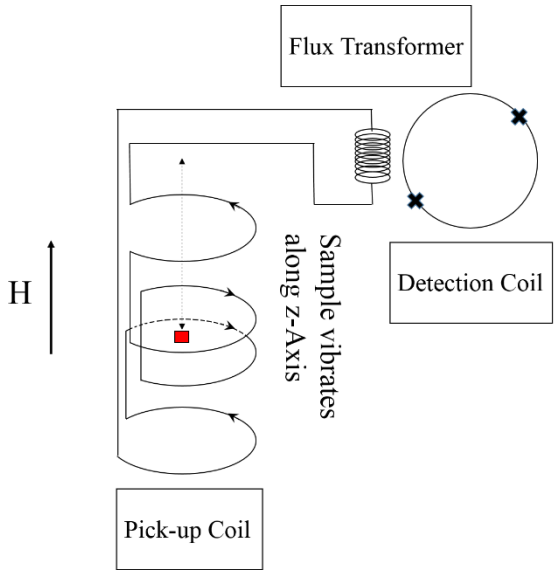

Figure 3-13 Schematic diagram of SQUID magnetometer, all wires are in their superconducting state.

signal. The magnetic field is produced by a superconducting magnet and is uniformly distributed throughout the pick-up coil area. The detection coil, in this setup, involves a superconducting ring with two Josephson junctions which include two superconducting materials separated by a thin layer of insulator [3.28, 3.29]. During the operation, a DC bias current is applied to the ring and kept constant through a feedback loop. Taking Reciprocating Sample Option (RSO) measurement for instance, the sample quickly oscillates through the central pick-up coil, causing a periodic magnetic flux change. With the help of lock-in amplifier to lock the frequency, the detection coil is able to counter the flux change by applying a voltage which is recorded and later fitted to an ideal dipole moment response. The sensitivity can be as high as 5×10^{-9} emu [3.30]. The tradeoff is the

measurement time. In order to minimize the background noise, the superconducting magnet is kept at persistent mode during each measurement. It would normally take significantly longer time to measure a full hysteresis loop comparing with AGFM or VSM.

Samples can be mounted in a straw with vertical length less than 5 mm in our SQUID system. Samples were handled with plastic/ceramic tools and the deformation of the straw was carefully evaded to avoid contamination [3.31]. Measurements, such as magnetization vs. temperature curve as well as typical hysteresis loops, can be performed in the temperature range from 1.8 K to 400 K with applied magnetic field of up to 7 T. The sensitivity with RSO is in the order of 10^{-7} emu with EverCool attachment. With the magnet reset option, the trapped field inside the superconducting magnet can be easily removed if a large field is previous applied.

3.8 Vibrating-Sample Magnetometer (VSM)

Ever since its invention in 1955, VSM has become the most common tool to measure magnetic properties due to its simplicity, flexibility and durability accompanied with reasonable sensitivity (10^{-6} emu) [3.26].

As shown in Figure 3-14, the sample is attached to a vibrating rod normally driven by a voice coil. A uniform static magnetic field is used to magnetize the sample. Due to the vibration, the magnetic stray field created by the sample would change the magnetic flux in the pick-up coils and can be sensed in the form of a voltage signal. A lock-in amplifier at a frequency specified by the signal from the sample vibrator is used to measure the signal. Since the signal measured by the pick-up coils is directly related to

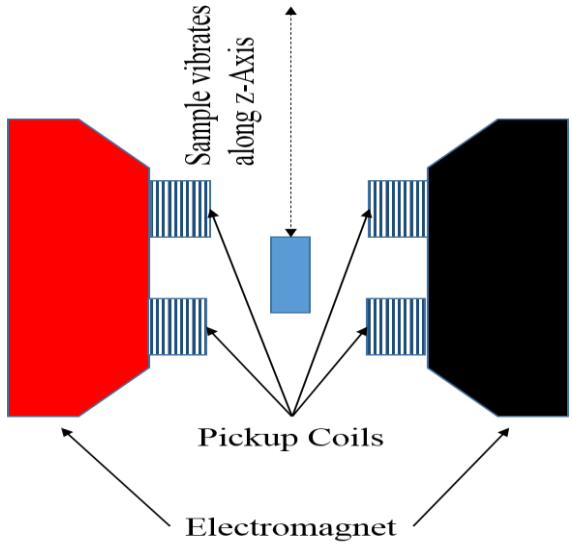

Figure 3-14 Schematic diagram of VSM. The sample size is chosen for clear view not based on real system scale.

the magnetization of the sample, the voltage signal can be converted to magnetization of the sample through a calibration process [3.32].

Our VSM is an option of PPMS with a superconducting magnet. Since no magnet reset option is available, the trapped field must be considered if a large field is previous applied. It can operate at a large temperature range of 2 – 800 K with magnetic fields of up to 9 T. The sensitivity of the measurement is on the order of 10^{-6} emu. The measurement time is close to that of the AGFM; however, the sample size is far less than the latter in order to mimic the dimension of a magnetic dipole.

3.9 Resistance Measurement System

Most resistance measurements in this study are carried under high/low temperature environment. The resistance measurement is carried by a four point probe method on all samples. The advantage of this setup is the negligible resistivity contribution from the contacts. During each measurement, the system alters the polarization of the current

passing through the sample, which greatly reduces the error caused by thermoelectric EMFs.

3.9.1 Resistivity Measurement Module of PPMS

As a part of the PPMS, the measure can be performed in a sealed environment and the temperature can vary from 2 to 300 K. Magnetic fields as high as 9 T can also be applied to study the magnetic field related resistivity change. Up to 3 samples can be measured simultaneously. This system is used to study the low temperature behavior of the Kondo system. The sample size is 2 mm x 0.5 mm x 50 nm, which has a typical resistance less than 1 ohm.

3.9.2 High Temperature Resistance Measurement System (HTRMS)

The home-made HTRMS was developed to fulfill two purposes: first, to monitor the resistance change during MA process; second, to perform high temperature resistance measurement for the test subject. Samples are sealed in an Ar/H_2 forming gas environment and can be heated up to 623 K with external magnetic field up to 10 kOe. The system is controlled by a Labview program and information such as temperature, magnetic field, current and voltage can be recorded simultaneously. It was used to study the annealing effect and high temperature characterization of MTJ in Chapter 6. The typical resistance of the MTJ used in this study is in the order of kOhm.

3.10 References

[3.1] P. J. Kelly and R. D. Arnell, Vacuum **56** (3), 159 (2000).

[3.2] R. Behrisch and W. Eckstein, *Sputtering by particle bombardment: experiments and computer calculations from threshold to MeV energies*. (Springer, Berlin ; New York, 2007), p.507.

[3.3] G. Bräuer, B. Szyszka, M. Vergöhl, and R. Bandorf, Vacuum **84** (12), 1354 (2010).

[3.4] T. Iseki, Vacuum **84** (2), 339 (2009).

[3.5] V. N. Popok, I. Barke, E. E. B. Campbell, and K. H. Meiwes-Broer, Surf. Sci. Rep. **66** (10), 347 (2011).

[3.6] G. Galinis, G. Torricelli, A. Akraiam, and K. Haeften, J. Nanopart. Res. **14**, 1057 (2012).

[3.7] A. Perez, P. Melinon, V. Dupuis, P. Jensen, B. Prevel, J. Tuaillon, L. Bardotti, C. Martet, M. Treilleux, M. Broyer, M. Pellarin, J. L. Vaille, B. Palpant, and J. Lerme, J. Phys. D: Appl. Phys. **30** (5), 709 (1997).

[3.8] K. Sattler, J. Mühlbach, and E. Recknagel, Phys. Rev. Lett. **45** (10), 821 (1980).

[3.9] H. Yasumatsu, The European Physical Journal D **63** (2), 195 (2011).

[3.10] C. Xirouchaki and R. E. Palmer, Philosophical transactions. Series A, Mathematical, physical, and engineering sciences **362** (1814), 117 (2004).

[3.11] N. X. Sun, S. Mehdizadeh, C. Bonhote, Q. F. Xiao, and B. York, J. Appl. Phys. **97** (10), 10N904 (2005).

[3.12] J. D. Verhoeven, *Fundamentals of physical metallurgy*. (Wiley, New York, 1975), p.567.

[3.13] M. Ashby, R. W. Messler, R. Asthana, E. P. Furlani, I. Polmear, and R. A. Higgins, (Elsevier, Burlington, 2009).

[3.14] C. Brombacher, C. Schubert, K. Neupert, M. Kehr, J. Donges, and M. Albrecht, J. Phys. D: Appl. Phys. **44** (35), 355001 (2011).

[3.15] T. Yokota, M. L. Yan, Yingfan Xu, L. Gao, R. Zhang, L. Nicholl, L. Yuan, R. Skomski, D. J. Sellmyer, S. H. Liou, Chih-Huang Lai, Cheng-Han Yang, and Sheng-Huang Huang, J. Appl. Phys. **97** (10), 10H306 (2005).

[3.16] K. Aimuta, K. Nishimura, S. Hashi, and M. Inoue, presented at the Magnetics Conference, 2005. INTERMAG Asia 2005. Digests of the IEEE International, 2005 (unpublished).

[3.17] D. S. Li, H. Garmestani, Shi-shen Yan, M. Elkawni, M. B. Bacaltchuk, H. J. Schneider-Muntau, J. P. Liu, S. Saha, and J. A. Barnard, J. Magn. Magn. Mater. **281** (2-3), 272 (2004).

[3.18] W. F. Smith and J. Hashemi, *Foundations of materials science and engineering*. (McGraw-Hill, Boston, Mass., 2010), pp 1068.

[3.19] B. D. Cullity, *Elements of x-ray diffraction*, 2d ed. (Addison-Wesley Pub. Co., Reading, Mass., 1978), pp.554.

[3.20] A. Gibaud and S. Hazra, Curr. Sci. **78** (12), 1467 (2000).

[3.21] K. D. Vernon-Parry, III-Vs Review **13** (4), 40 (2000).

[3.22] P. Russell, D. Batchelor, and J. Thornton, Veeco Instruments Inc., AN46, Rev A **1**, 2004 (2001).

[3.23] M. R. Lee, Mineral. Mag. **74** (1), 1 (2010).

[3.24] A. Bogner, P. H. Jouneau, G. Thollet, D. Basset, and C. Gauthier, Micron **38** (4), 390 (2007).

[3.25] A. J. D'Alfonso, B. Freitag, D. Klenov, and L. J. Allen, Phys. Rev. B **81**, 100101(R) (2010).

[3.26] C.D. Graham, J. Mater. Sci. Technol. **16** (02), 97 (2000).

[3.27] P. J. Flanders, J. Appl. Phys. **63** (8), 3940 (1988).

[3.28] R. L. Fagaly, Rev. Sci. Instrum. **77** (10), 101101 (2006).

[3.29] N. A. Spaldin, *Magnetic materials : fundamentals and applications*, 2nd ed. (Cambridge University Press, Cambridge ; New York, 2011), p.274.

[3.30] A. Arauzo, E. Guerrero, A. Urtizberea, J. Stankiewicz, and C. Rillo, Rev. Sci. Instrum. **83** (6), 066106 (2012).

[3.31] M. A. Garcia, E. F. Pinel, J. de la Venta, A. Quesada, V. Bouzas, J. F. Fernandez, J. J. Romero, M. S. Martin-Gonzalez, and J. L. Costa-Kramer, J. Appl. Phys. **105**, 013925 (2009).

[3.32] J. Lindemuth, J. Krause, and B. Dodrill, IEEE T. Magn. **37** (4), 2752 (2001).

Chapter 4 : Kondo Effect in Isolated Cu(Fe) Particles

When magnetic material is doped as impurities inside non-magnetic metallic matrix, the interaction between the impurity spin and conduction electron spins could give rise to interesting phenomena, such as Kondo effect [4.2]. The advance in material engineering, nanofabrication and implementation of new experimental methods push the study of the Kondo effect further into low-dimensional systems such as quantum dots, clusters and even atoms [4.3-6]. For such system, the interaction cannot fully extend in all three dimensions and it offers new insight to the Kondo effect. Ever since, the interest in the nano-scale properties of such system grows exponentially, both in experiments and theories [4.7, 4.8].

Most efforts have been devoted on finding the existence of the Kondo screening cloud. Although predicted by many, this phenomenon has not been observed experimentally [4.9-11]. One of the many reasons is that, in most cases, the Kondo screening cloud diameter is much smaller than the dimensions of the investigated systems, even for nanoscale Kondo effect studies [4.12, 4.13]. Theory has predicted that the low temperature behavior of the Kondo effect, namely the flatten part of the magnetic susceptibility, would develop prematurely due to the underscreening of the conduction election [4.12]. Allowing the Kondo screening cloud to develop fully would make it difficult to observe such effect.

Using confined clusters to study the behavior of low dimensional Kondo effect has been proposed to be able to separate nanoscale effect from the bulk [4.12]. As demonstrated in Figure 4-1, the Kondo screening cloud can be restrained by putting magnetic impurities within a metallic cluster embedded in an insulating matrix, with

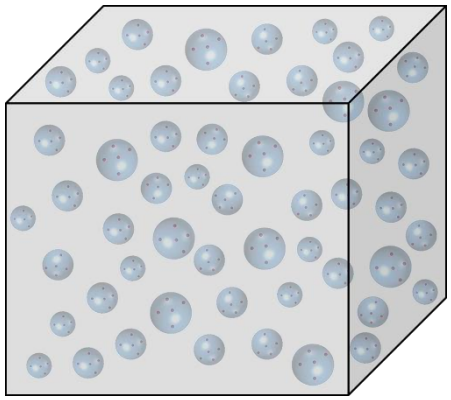

Figure 4-1 Non-magnetic metal clusters inside an insulating matrix. The Clusters are doped with magnetic impurities and are well separated from each other to prevent interaction.

dimensions smaller than that of the Kondo screening cloud [4.12]. Although the characteristic resistivity measurements are difficult to perform for such system, we can still investigate the Kondo effect by studying its magnetic properties as described in Section 2.2.4.

4.1 Experimental Design

The clusters were generated in a home-made cluster-deposition system using DC magnetron sputtering as described in Section 3.1.3. The base pressure of the aggregation chamber where the clusters condensed in-flight is in the order of 10^{-8} Torr with liquid Nitrogen cooling, while the deposition chamber is operated at 10^{-6} Torr at the room temperature. A three-inch composite target was prepared using the method described in Section 3.2.2. It was designed to give a certain Fe concentration in the Cu(Fe) clusters.

A pressure differential between the aggregation and deposition chambers drove the clusters through a 7 mm orifice and onto a 25 μm thick Kapton film substrate at ambient temperature. An insulating matrix of SiO_2 was sputtered either simultaneously or in turn onto the substrate in the deposition chamber to ensure the isolation of the individual

copper clusters. The substrate normal was tilted 20º from the cluster incidence and 70 º from the SiO_2 particle beam for optimal co-deposition, while remain 90 º for samples with stack structure. Unless specified otherwise, cluster layers are reported in nominal thickness. The cluster size distribution was determined by the TEM from a Cu(Fe) cluster layer covered by SiO_2 deposited on a copper grid. As described in Section 3.1.3, it is important to prepare clusters with small sizes, since the Fe atoms presented in the cluster would be minimized for a given Fe concentration. Therefore, the sputtering condition labeled as C1 in Section 3.1.3 was used for the cluster deposition where Ar/He ratio was 1, gun to aperture distance was 20 cm and the DC sputtering power was 18W.

Cu(Fe) thin films with the same Fe concentration was deposited on Si/SiO_2 substrate from the 2 inch sputtering gun. The film thick is 50 nm and the sample is cut into a bar shape to perform the temperature dependent resistance measurement. The resistance measurement was carried by the resistivity measurement module of PPMS at temperature from 2 K to 300 K using 4 point measurement as described in Section 3.9.1.

Magnetic measurements were performed on the Cu(Fe) cluster samples. The co-sputtered samples consist of approximately 16% volume percent of Cu(Fe) clusters in a 780 nm thick SiO_2 matrix deposited on a Kapton film substrate while the stacked samples have the following structure, Kapton/ $[Cu(Fe)\ (2Å)/SiO_2(3nm)]_{200}$. The one square inch flexible substrate was then folded into a hollow cylinder of 3 mm height and 5 mm in diameter for measurement in a SQUID magnetometer. The ZFC measurement for the samples covered the temperature range of 2 K to 150 K with an applied field of 200 Oe.

Kapton film has been used as substrate in many systems due to its superior dimensional stability, small coefficient of thermal expansion and high glass transition

temperature [4.14, 4.15]. Figure 4-2(a) shows the volume dependent magnetization of the Kapton film substrate cut from different places and reveals a linear behavior which suggests the substrate magnetic properties are quite consistent. Similar to SiO_2, the Kapton film shows clear diamagnetic behavior as demonstrated in Figure 4-2(b).

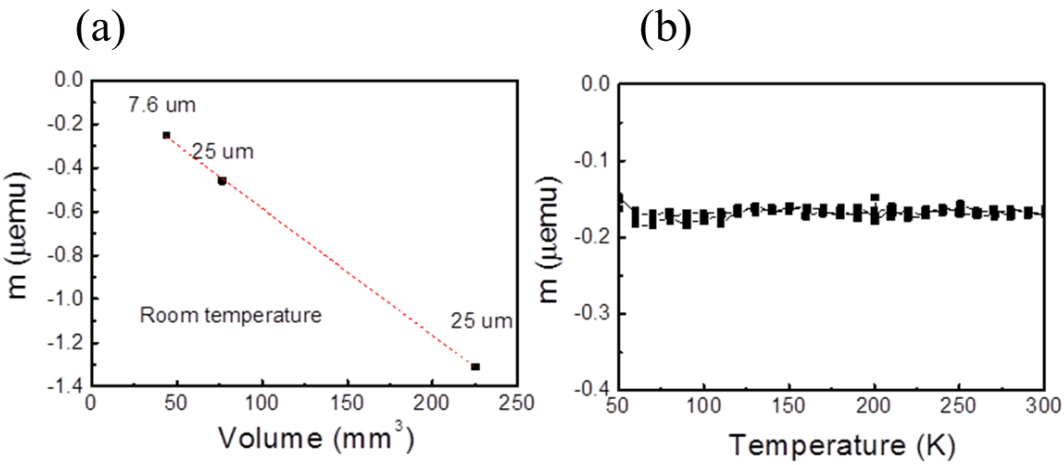

Figure 4-2 (a) Room temperature volume dependent magnetization and (b) ZFC/FC measurement under 1 kOe magnetic field of Kapton film substrate. The consistency of property make Kapton suitable to serves as a substrate in this research

4.2 Kondo effect in Cu(Fe) thin film

The film sample that contains 0.3 at.% Fe was prepared for resistivity measurement and showed clear Kondo behavior as demonstrated in Figure 4-3. A resistivity minimum followed by logarithmic temperature dependence is observed below 10 K. As the temperature decreases further, the resistivity shows a tendency towards saturation. The effect is suppressed by the present of an external magnetic field which is a common phenomenon for the Kondo effect [4.16].

The measured result was fitted using the empirical numerical renormalization-group (NRG)-like equation

$$\rho_m = \rho_0 \left[1 + \left(2^{\frac{1}{\alpha_s}} - 1\right)\left(\frac{T}{T_K}\right)^{\xi_s}\right]^{-\alpha_s} \quad (4.1)$$

where ρ_0 is the residual resistivity, T_K is the Kondo temperature, and ξ_s and α_s are fitting

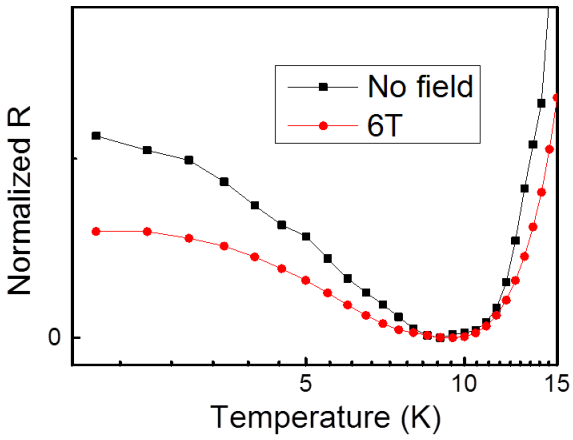

Figure 4-3 Temperature dependence of resistance of Cu(Fe) thin film with 0.3 at.% Fe under no magnetic field (black square) and 6 T field (red dot) in log scale. The Kondo effect is suppressed by the present of the magnetic field.

parameters [4.17]. Detailed information regarding this method can be found in the literature [4.17, 4.18]. As shown in Figure 4-4, a reasonably good fitting can be achieved using the above equation. The corresponding Kondo temperature acquired from the fitting for samples with 0.3 at. % Fe and 1 at. % Fe are 4.2 K and 0.3 K respectively. The drop of Kondo temperature with increasing Fe concentration is consistent with the previous studies [4.19, 4.20]. The Kondo screening length ξ_K can be estimated using the following equation from Section 2.2.3 [4.21].

$$\xi_K = \frac{h v_F}{k_B T_K} \quad (2.25)$$

where υ_F=1.57×10^6 m/s is the Fermi velocity of Cu [4.22]. Therefore the estimated Kondo screening length for Fe in Cu is around 3μm.

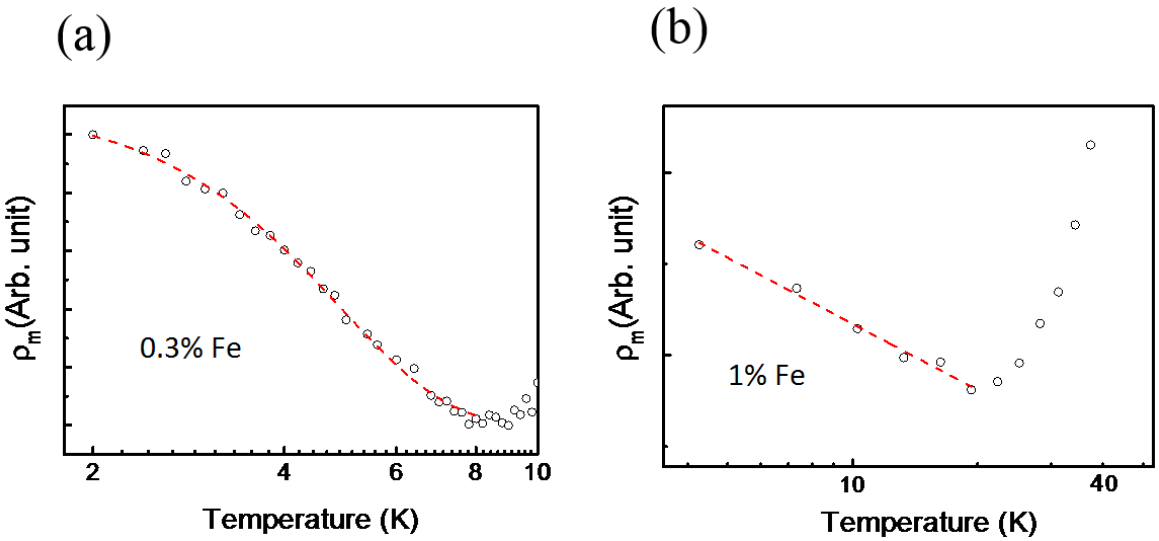

Figure 4-4 Resistivity fitting (dashed line) with Eq. 4.1 for Cu(Fe) with (a) 0.3 at.% Fe and (b) 1 at.% Fe

4.3 Characterization of Cu(Fe) Cluster Embedded in SiO_2 Matrix

As revealed by the TEM image in Figure 4-5, the Cu(Fe) clusters are well separated

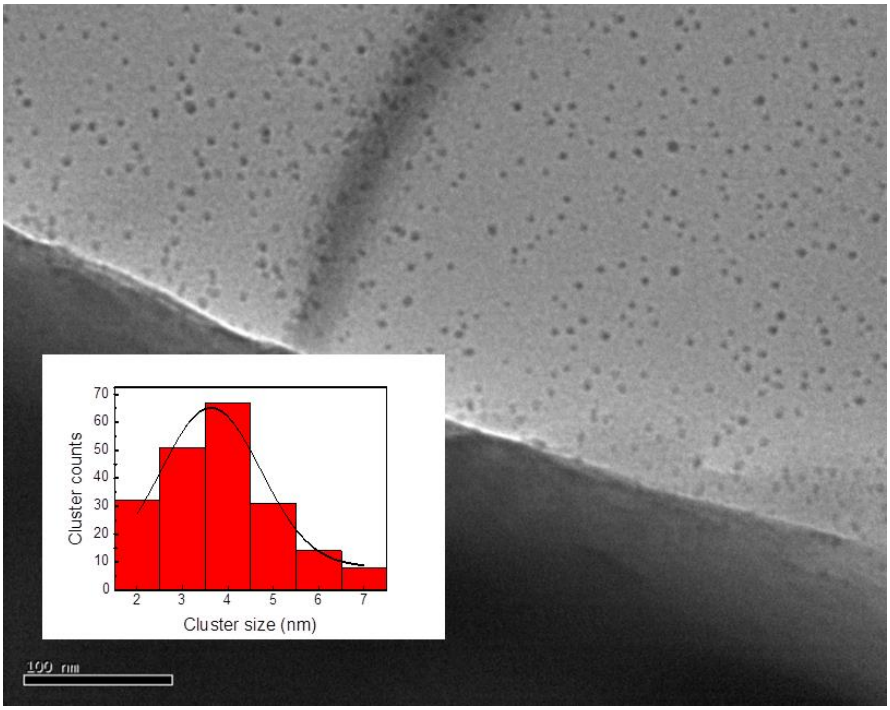

Figure 4-5 TEM image of Cu(Fe) clusters deposited on TEM grid. The insert is the cluster size distribution measured from the sample. Most clusters are well separated from each other.

from each other which eliminates the interaction between clusters. The shadow around the cluster is likely due to the strain effect around this nanometer-scale chemical zone [4.23]. The inset of Figure 4-5 also shows the clusters have an average diameter of around 4 nm which is much smaller than the estimated Kondo-cloud screening length. A 4 nm Cu cluster with FCC structure roughly contains 3000 Cu atoms. If it contains 0.3 at.% Fe impurity, there will be around 9 Fe atoms inside each cluster. In this case, the average Fe-Fe distance is close to 1.6 nm.

The ZFC measurement for co-sputtered Cu(Fe) clusters with 0.3 at.% Fe is shown in Figure 4-6. The curve shows clear paramagnetic-like behavior and no downturn was observed above 2 K. It can be fitted reasonably well with the following expression,

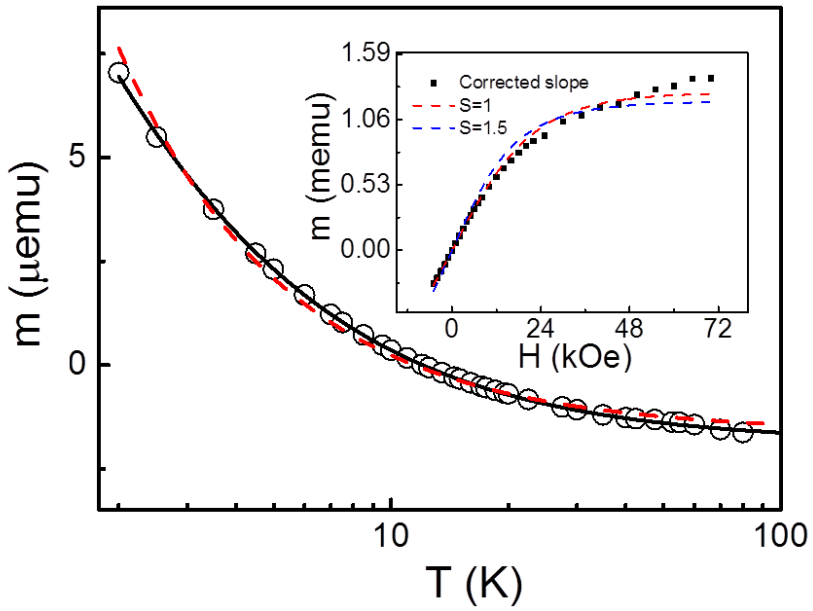

Figure 4-6 ZFC measurement of 0.3 at.% Fe-doping Cu clusters with 200 Oe applied field where the solid line is the fitting with Curie-Weiss law and the dashed line is the fitting with the Curie law. The inset is the *M-H* curve measured at 2 K where the dashed line is the fitting using Brillouin function with S=1 and 3/2.

$$M = \chi_0 H + \frac{CH}{T - \theta} \tag{4.2}$$

where χ_0 represents the temperature-independent term while the second term is due to the impurities plus Kondo interactions and θ is considered as an interaction temperature. The fitting yields θ = -0.7 K, which indicates an AFM interaction. If the interaction is indeed the Kondo interaction, then we have T_K = 0.7 K which is significantly smaller than the value acquired in bulk system [4.20], suggesting the Kondo interaction is suppressed by the reduced size of the system. Figure 4-6 inset shows the $M(H)$ curve after removing the diamagnetic background, and a reasonable fitting can be achieved using the Brillouin function with S = 1. As shown in Table 4-1, samples with stack structure show similar low temperature behaviors and the increase of Fe concentration also suppresses the Kondo effect.

Table 4-1 Cu(Fe) clusters with different structure and Fe concentration

Fe concentration (at. %)	Structure	θ (K)
0.3	Co-sputtering	-0.7
0.15	Co-sputtering	-0.9
0.3	Stack	-0.6
0.15	Stack	-1.0

Since the Fe atoms are randomly distributed in the Cu matrix, they are likely to experience coupling due to RKKY interactions. If these interactions are predominantly AFM, then they may mimic or mask the Kondo effect, because both mechanisms reduce the low-temperature susceptibility with respect to the Curie $1/T$ law. The interaction effect must be treated quantum-mechanically, because the Kondo effect consists in the discrete flipping of individual spins, and such a quantum-mechanical flipping can also be caused by AFM interactions. A classical interaction would yield an unphysical

continuous "wiggling" of the coupled spins and blur the discrete character of the Kondo effect.

Based on Dr. Skomski's calculation, for interacting spin-1 particles, the spin-1/2 Pauli matrices must be replaced by the spin operators [4.25]:

$$S_x = \frac{1}{\sqrt{2}}\begin{pmatrix} 0 & 1 & 0 \\ 1 & 0 & 1 \\ 0 & 1 & 0 \end{pmatrix};\ S_y = \frac{i}{\sqrt{2}}\begin{pmatrix} 0 & -1 & 0 \\ 1 & 0 & -1 \\ 0 & 1 & 0 \end{pmatrix};\ S_z = \begin{pmatrix} 1 & 0 & 0 \\ 0 & 0 & 0 \\ 0 & 0 & -1 \end{pmatrix} \qquad (4.3)$$

For isolated Fe particles in a field $\mathbf{H} = H\,\mathbf{e}_z$, only the last matrix is important, and the susceptibility is given by the Brillouin function $B_1(x)$. We consider pairs of $S = 1$ spins S_1 and S_2, coupled by Heisenberg exchange $-J\,S_1 \cdot S_2$. The interactions can then be written as direct products of the matrices of Eq. 4.3 for S_1 and S_2. The diagonalization of the resulting 9×9 matrix yields an $S = 2$ quintuplet of energy $-J$, an $S = 1$ triplet of energy $+J$, and an $S = 0$ singlet of energy $+2J$. Figure 4-7 shows these levels for positive (FM) and negative (AFM) values of J.

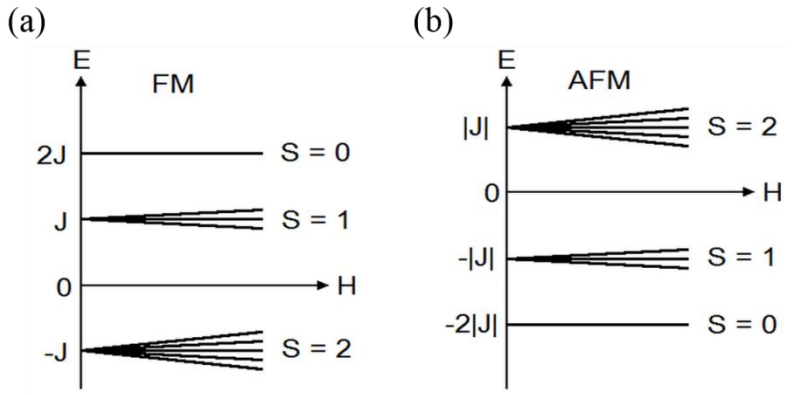

Figure 4-7 Energy levels for two interacting S = 1 atoms with (a) FM and (b) AFM RKKY interaction.

In the FM case, the main contribution to the susceptibility comes from the FM quintuplet, bottom of Figure 4-7(a), with small corrections due to the triplet. For AFM

coupling the situation is more complicated. The AFM ground state (S = 0) does not contribute to the susceptibility, but the S = 1 triplet is fairly close to the singlet and gives rise to a Van-Vleck-type susceptibility. Physically, the singlet and triplet states mean that the two coupled spin-1 atoms involve four spin-1/2 electrons with "two spins up, two spins down" (singlet) and "three spins up, one spin down" (triplet), and the corresponding wave functions are obtained by diagonalizing the above-mentioned 9 × 9 matrix.

The susceptibilities are readily obtained via the partition functions belonging to Figure 4-7 (a) and (b). In the FM case (a) the result is, in lowest order, equal to the susceptibility predicted by the Brillouin function $B_2(x)$. In the AFM case (b) the lowest-order susceptibility is zero, but there is a small Van-Vleck contribution proportional to the small parameter $\lambda = \exp(-|J|/k_BT)$. By contrast, the triplet correction to the FM quintuplet is of the order $\lambda^2 = \exp(-2|J|/k_BT)$. Figure 4-8 compares the corresponding susceptibility contributions and it can be seen that the contribution from the AFM coupling is quite small. As described in the previous section, in the present case, the

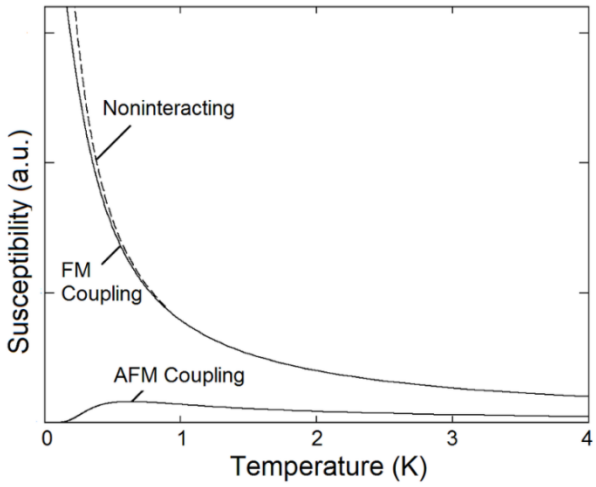

Figure 4-8 Susceptibility of non-interacting and interacting Fe atoms in Cu.

average Fe-Fe distance is 1.6 nm for samples with 0.3 at.% Fe impurity. Systematic experimental and theoretical studies on the RKKY interaction of Fe atoms in Cu have been carried by professor Wiesendanger's group. Around the distance of 1.6 nm, the RKKY exchange is either negative with small magnitude, less than about 0.5 K in temperature units, or even positive [4.1]. Therefore, it should not interfere greatly with the Kondo effect at such distance.

4.4 Conclusions

In conclusion, we have observed the Kondo effect in dilute Cu:Fe thin-film samples. Our magnetic susceptibility measurements indicate that the effect is reduced in isolated Cu:Fe particles. This is ascribed to the strong reduction of the Kondo screening cloud, which cannot be bigger than the particle size, and consistent with theoretical predictions. RKKY interactions between Fe atoms in one cluster are estimated to yield very small corrections.

4.5 References

[4.1] A. A. Khajetoorians, J. Wiebe, B. Chilian, S. Lounis, S. Blugel, and R. Wiesendanger, Nature Physics **8** (6), 497 (2012).

[4.2] J. Kondo, Prog. of Theor. Phys. **32** (1), 37 (1964).

[4.3] W. T. Herrera, Y. T. Xing, S. M. Ramos, P. Munayco, M. B. Fontes, E. M. Baggio-Saitovitch, and F. J. Litterst, Phys. Rev. B **84** (1), 014430 (2011).

[4.4] N. Roch, S. Florens, T. A. Costi, W. Wernsdorfer, and F. Balestro, Phys. Rev. Lett. **103**, 197202 (2009).

[4.5] N. Neel, J. Kroger, R. Berndt, T. O. Wehling, A. I. Lichtenstein, and M. I. Katsnelson, Phys. Rev. Lett. **101** (26), 266803 (2008).

[4.6] W. B. Thimm, J. Kroha, and J. von Delft, Phys. Rev. Lett. **82** (10), 2143 (1999).

[4.7] R. Zivieri, G. Consolo, E. Martinez, and J. Kerman, Adv. Condens. Matt. Phys. **2012**, 1 (2012).

[4.8] B. V. Costa, Braz. J. Phys. **41** (1), 94 (2011).

[4.9] I. Affleck, in *Perspectives of Mesoscopic Physics*, edited by Ora Entin-Wohlman and Amnon Aharony (World Scientific Publishing Co. Pte. Ltd., Singapore, 2010), pp. 1.

[4.10] G. Bergmann, Phys. Rev. B **77** (10), 104401 (2008).

[4.11] M. N. Kiselev, K. A. Kikoin, L. Y. Gorelik, and R. I. Shekhter, Phys. Rev. Lett. **110**, 066804 (2013).

[4.12] R. Skomski, R. Zhang, P. Kharel, A. Enders, S. H. Liou, and D. J. Sellmyer, J. Appl. Phys. **107** (9), 09E126 (2010).

[4.13] O. Ujsaghy and A. Zawadowski, J. Phys. Soc. Jpn. **74** (1), 80 (2005).

[4.14] T. Kinkeldei, C. Zysset, K. Cherenack, and G. Troester, presented at the Sensors, 2009 IEEE, 2009 (unpublished).

[4.15] S. Stadler, I. Derhalli, Khan M., and Chantal G., Proc. SPIE 3225, *Microlithography and Metrology in Micromachining III*, 102 (September 2, 1997).

[4.16] S. Andergassen, D. Feinberg, S. Florens, M. Lavagna, S. Shiau, P. Simon, and R. Van Roermund, Int. J. Nanotechnol. 7 (4-8), 438 (2010).

[4.17] J. J. Parks, A. R. Champagne, T. A. Costi, W. W. Shum, A. N. Pasupathy, E. Neuscamman, S. Flores-Torres, P. S. Cornaglia, A. A. Aligia, C. A. Balseiro, G. K. L. Chan, H. D. Abruna, and D. C. Ralph, Science **328** (5984), 1370 (2010).

[4.18] R. Bulla, T. A. Costi, and T. Pruschke, Rev. Mod. Phys. **80** (2), 395 (2008).

[4.19] M. Sasaki, A. Ohnishi, T. Kikuchi, M. Kitaura, Ki-Seok Kim, and Heon-Jung Kim, Phys. Rev. B **82** (22), 224416 (2010).

[4.20] J. M. Franz and D. J. Sellmyer, Phys. Rev. B **8** (5), 2083 (1973).

[4.21] M. Ternes, A. J. Heinrich, and W. D. Schneider, J. Phys.: Condens. Matter **21** (5), 053001 (2009).

[4.22] Charles Kittel, *Introduction to Solid State Physics*, 8th ed. (Wiley, Hoboken, NJ, 2005), p.139.

[4.23] B. Fultz and James M. Howe, *Transmission electron microscopy and diffractometry of materials*. (Springer, Berlin ; New York, 2001), p.748.

[4.24] R. A. Brand, H. Georges-Gibert, and C. Kovacic, J. Appl. Phys. **51** (5), 2647 (1980).

[4.25] D. J. Craik, *Magnetism: Principles and Applications*. (Wiley, Chichester, NY, 1995), pp.459.

Chapter 5 : Magnetization Reversal in Transition-Metal/Fe:SiO_2 Thin Films

Magnetic-field sensors have a significant impact on many different areas of modern society and technology [5.1]. This applies, in particular, to magnetic field sensors using MTJs, which have attracted much attention in recent decades due to high MR ratios [5.2-4]. MTJ sensing devices normally contain multilayer structures where a soft-magnetic free layer serves as the sensing element. Those soft magnetic materials are commonly required to have high permeability and very small hysteresis loss [5.5-9]. At present, this is achieved by finding novel magnetic materials [5.7, 5.10], using MFCs [5.6, 5.11], employing heat treatments in different environments [5.9, 5.12], and/or performing nanofabrication to exploit or to eliminate shape anisotropy [5.9, 5.12, 5.13]. All the methods mention above have their advantages and disadvantages, but most importantly, they are not mutually exclusive so that they can be implemented simultaneously. Finding a new mechanism to improve the free layer would simply add a new freedom in magnetic sensor design.

The aim of this chapter is to describe the development of a multilayered thin film to improve the performance of the soft FM layer for sensor applications. The concept of using multilayered magnetic systems has been widely used in recording media industry to improve the performance of the writability of the media, in form of exchange-spring magnets [5.14-16]. In this study, a ferromagnetic-superparamagnetic bilayer system was proposed to be able to reduce the coercivity and/or enhance the reversibility of the soft magnetic layer. By investigating the magnetic properties of various TM alloy layers adjacent to a layer of very soft superparamagnetic Fe particles embedded in a SiO_2 matrix,

a performance improvement of the TM layer has been established in all samples through a mechanism different from the exchange-spring magnets.

5.1 Experimental Design

The magnetron sputtering system described in Section 3.1.4 was used for the thin film deposition of all layers. It is commonly operated at a base pressure of 10^{-7} Torr with a multi-sample holder option attached. All sputtering targets were prepared in our lab through the sintering process described in Section 3.2.1, except the MgO and the NiFe targets which were commercially available. All metallic targets were sputtered using DC magnetron sputtering while MgO and Fe:SiO_2 were sputtered using RF. All samples were prepared on Si/SiO_2 substrates at the room temperature. The TM alloys were sputtered under the influence of a small magnetic field, less than 30 Oe, due to the magnetic flux from sputtering guns. No post annealing process was used.

Granular Fe:SiO_2 was deposited onto different TM alloy films including permalloy (NiFe), HCP CoFe, and amorphous CoFeB. The thickness of the soft-magnetic layer was kept constant for each series of samples, namely 20 nm NiFe, 5 nm CoFe, and 5 nm CoFeB, while the Fe:SiO_2 films have thicknesses varying from zero to 70 nm. Figure 5-1

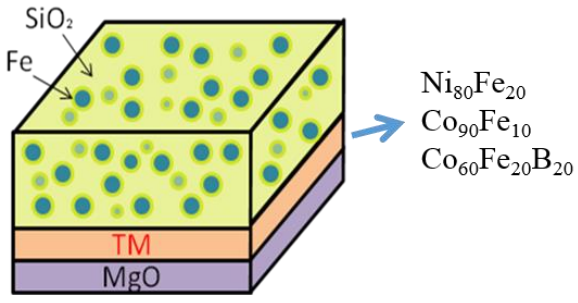

Figure 5-1 Soft-magnetic bilayer structure (schematic)

shows the schematic structure of such bilayer film. The Fe clusters are expected to be well separated not only from each other inside the SiO_2 matrix but also from the TM layers, which means no direct exchange interaction between particles. Single layer thin films of the TM and of the Fe:SiO_2 were also prepared for characterization purposes.

The *M(H)* magnetization curves were measured by AGFM with the magnetic field applied in the film plane. A typical sample size is 3 x 3 mm^2 and a gradient field of 0.04 Oe/mm was used for the AGFM measurements. SQUID was used to characterize the magnetic properties of the pure Fe:SiO_2 thin film.

5.2 Magnetic Properties of TM/Fe:SiO_2 Bilayer Systems

5.2.1 Properties of Fe:SiO_2

The Fe:SiO_2 composite target contains 70 at.% Fe, corresponding to a volume fraction of about 38% Fe in the granular film. It has been demonstrated in the previous studies that Fe particles in the granular film have an average size of less than 10 nm and are mainly bcc α-Fe [5.17-19]. Since the volume fraction of Fe in the Fe:SiO_2 granular films (38%) is below the percolation threshold of about 55%, the Fe particles are mostly isolated from each other in the amorphous SiO_2 matrix [5.20]. The particles are very small and therefore expected to be superparamagnetic single-domain particles, with fluctuating net moments and vanishing coercivity above their blocking temperature [5.17].

Figure 5-2 shows the *M-H* curve of a single layer Fe:SiO_2 granular film. The *M-H* curve exhibits a very small coercivity H_c, judging from the step size of the measurement, H_c is less than 50 mOe. Figure 5-2 inset(b) shows the ZFC/FC curve measured from 5 K to 300 K in a magnetic field of 100 Oe. The ZFC/FC measurement shows the

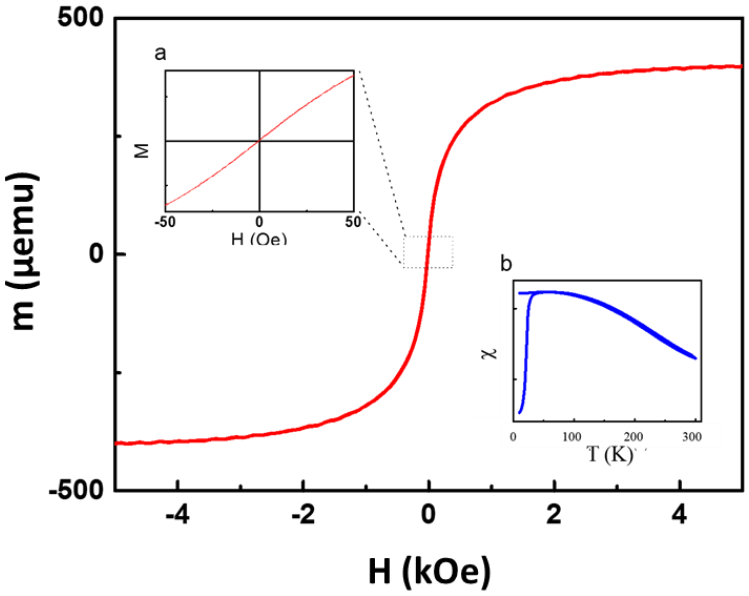

Figure 5-2 M-H curve of single layer Fe:SiO_2 granular film. The right inset is the FC/ZFC curve of the same film and left inset is the enlarged view of the M-H curve in the dashed box region

superparamagnetic behavior, and from the figure, a blocking temperature of about 38 K was estimated. As described in Section 2.3.4, $V \approx \frac{25k_BT_B}{K_1}$ and the bulk anisotropy of Fe is roughly 0.05 MJ/m^3, it gives the Fe particle of 7.9 nm in diameter. This result is in fair agreement with the above-mentioned value of 10 nm [5.18, 5.21]. Detailed information regarding the properties of the Fe:SiO_2 thin films can be found in the references [5.17, 5.18, 5.20, 5.22]. To summarize the magnetic properties of the pure Fe:SiO_2, the thin film is superparamagnetic, which has hysteresis loops without inflections and a very small coercivity.

5.2.2 CoFe/Fe:SiO_2

As demonstrated in the inset in Figure 5-3, the in-plane hysteresis loops of the CoFe samples are magnetically isotropic, despite the presence of a magnetic field during deposition. For the bilayer samples, 31% to 87% of the magnetization of the sample is

contributed by the Fe:SiO_2 layer, depending on its thickness. The coercivity initially

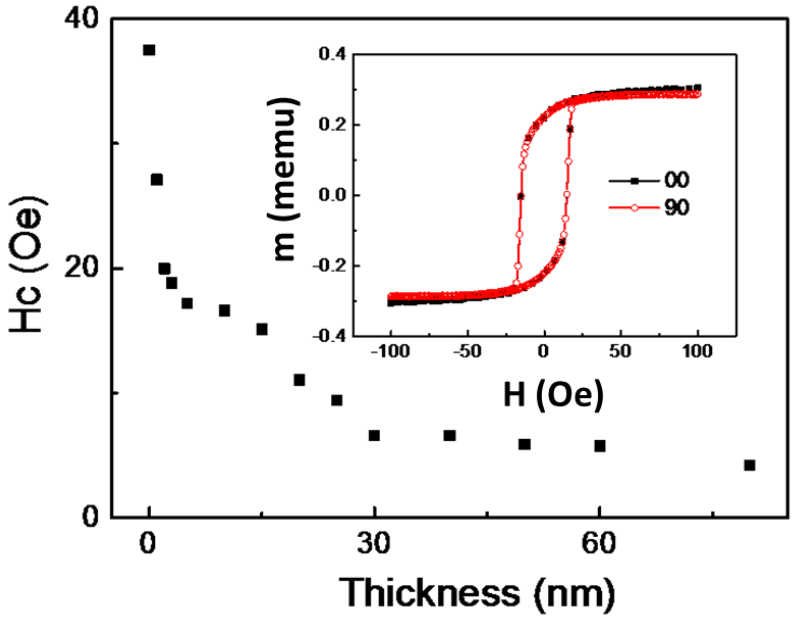

Figure 5-3 Bilayer coercivity as a function of the Fe:SiO_2 thickness. The inset shows the in-plane hysteresis loops of CoFe (5 nm)/Fe:SiO_2 (30 nm)bilayer sample along two orthogonal directions.

drops steeply as the thickness of the Fe:SiO_2 layer increases and then slowly approaches to a constant, as shown in Figure 5-3. The best improvement was achieved for samples with Fe:SiO_2 layer larger than 30 nm. The coercivity changed from 37.5 Oe (without Fe:SiO_2) to 6.6 Oe (with 30 nm Fe:SiO_2). No obvious change was observed for the permeability near zero field in all samples.

5.2.3 NiFe/Fe:SiO_2

Due to the presence of a small external magnetic field during deposition, an easy axis and a hard axis were formed in the film plane of the NiFe(20 nm)/Fe:SiO_2(x nm) sample. The coercivity reduction due to addition of Fe:SiO_2 layer was also observed and follows a similar trend as CoFe. Figure 5-4 shows the hysteresis loops for typical NiFe films with and without Fe:SiO_2. Depending on Fe:SiO_2 layer thicknesses, the

magnetization contribution from the Fe:SiO_2 is between 14% and 70%. Although all samples with Fe:SiO_2 measured along easy axis exhibit some decrease in coercivity, the

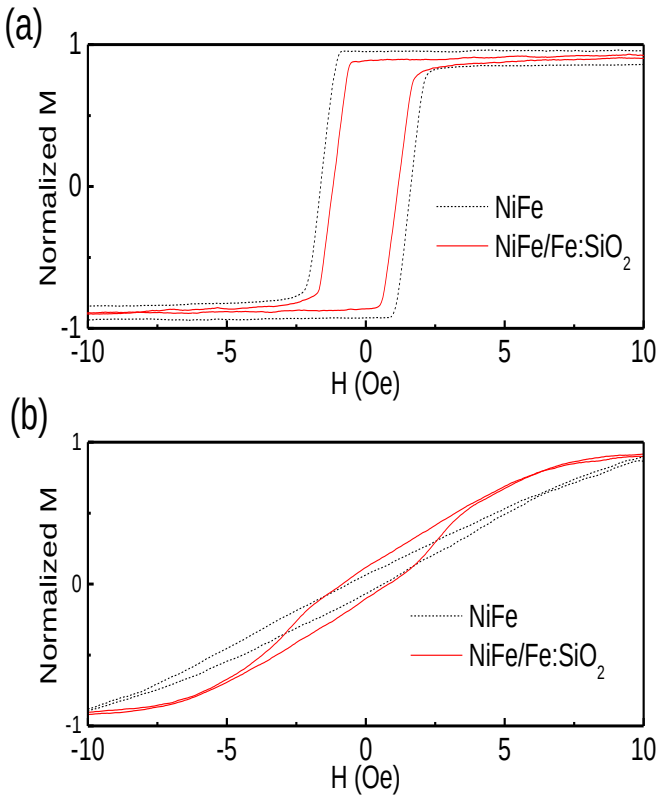

Figure 5-4 Hysteresis loops of easy axis (a) and hard axis (b) of 20 nm NiFe films with 40 nm Fe:SiO_2 (solid red line) and without Fe:SiO_2 (dashed black line).

best improvements were achieved for samples with 40 nm Fe:SiO_2 (Figure 5-4(a)). The coercivity along easy axis changed from 1.57 Oe (without Fe:SiO_2 top layer) to 1.04 Oe (with 40 nm Fe:SiO_2 top layer), but the permeability did not exhibit noticeable change. The coercivity along the hard axis was about 0.7 Oe, which is the same as in the pure NiFe sample, but the permeability was increased by a factor of 2, as shown in Figure 5-4(b).

5.2.4 CoFeB/Fe:SiO_2

Similar to the NiFe samples, the amorphous CoFeB samples also exhibit an easy axis and a hard axis due to the presence of the magnetic field. The magnetization contribution from the Fe:SiO_2 layer varies from 35% to 88% depending on the Fe:SiO_2 layer thickness. Figure 5-5(a) shows that the coercivity along both the easy and hard axis of the CoFeB samples drops as the thickness of Fe:SiO_2 layer increases and slowly

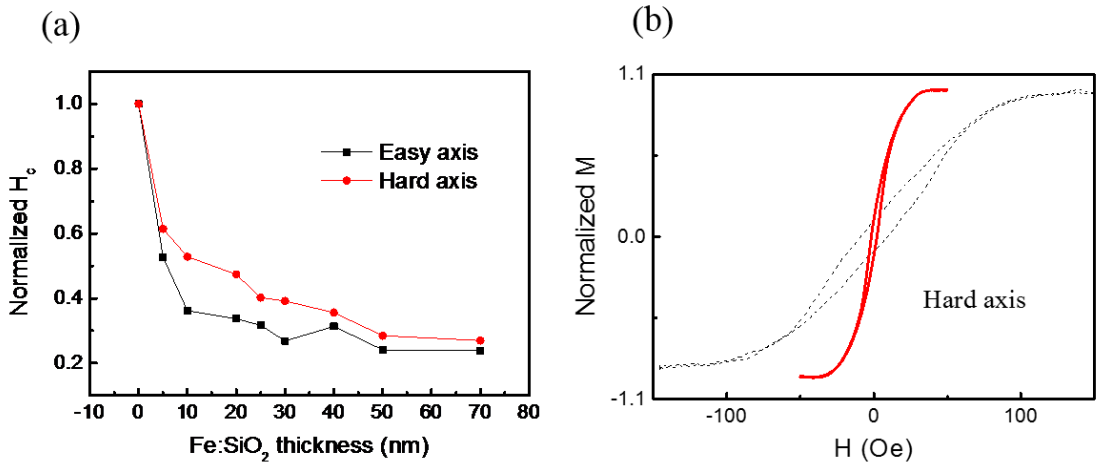

Figure 5-5 Bilayer coercivity as a function of the Fe:SiO_2 thickness measured along easy axis. The inset shows hysteresis loops of un-covered (black dashed line) and Fe:SiO_2 (70 nm)-covered (red solid line) CoFeB films, both measured along the hard axis.

approaches a minimum value. The permeability for the easy axis remains almost constant as the Fe:SiO_2 thickness increases, but the permeability along the hard axis increases by a factor 5 companied with the coercivity change from 3.75 Oe to 1.77 Oe as shown in Figure 5-5(b).

5.3 Micromagnetic Origin of Coercivity Reduction

The hysteresis of the films, including coercivity and loop slope, is determined by magnetization processes which largely depend on the interaction between the Fe particles

and the TM films. As described in the previous sections, the Fe clusters are typically well-separated from each other and from the continuous TM film by an insulating SiO_2 matrix, so the hysteresis-loop changes of the preceding section cannot be explained by the interatomic exchange. However, the quasi-infinite character of the TM layers leads to the formation and motion of domain walls [5.23], so that the Fe particles can affect the pinning behavior of the walls by magnetostatic interactions.

The simplest approach to the micromagnetic modeling of complex domain-wall phenomena is to determine the domain-wall energy as a function of the domain wall position [5.21, 5.24]. As discussed in Section 2.3.3, the domain-wall energy is $E_{wall} = L^2(\gamma(x) - 2\mu_0 M_s H x)$ where γ is the domain-wall energy, *x* is the domain wall position in a suitable chosen coordinate frame, and L^2 is an effective domain-wall area. For a simple Bloch wall, $\gamma_B = 4\sqrt{AK_1}$, but in the present case, γ contains contributions from the magnetostatic and exchange interactions between the continuous-layer domain-wall and the Fe particles in the SiO_2 matrix. Magnetostatic fields created by homogeneously magnetized thin films are important at the film edges only, but domain walls create substantial stray fields, which can interact with the Fe particles. The magnitude of the coupling field is strongly fluctuating and varies between 0 and 500 Oe. However, only a very small fraction of these interaction fields translate into coercivity changes. Figure 5-6 shows the schematic stray-field contributions created by Bloch walls (a) and Néel walls (b). The soft particles interact with these stray fields, and this interaction depends on the relative distance between the wall and the defect and also on the nature of the wall (Bloch wall or Néel wall). In fact, Néel walls are realized in very thin films and Bloch to Néel wall transitions start at or above 20 nm [5.18, 5.25-27]. A possible mechanism and

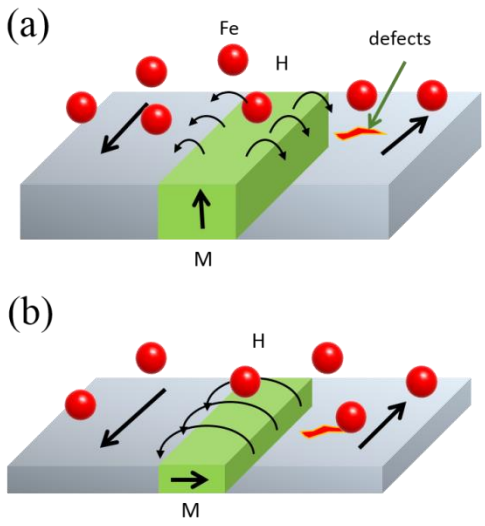

Figure 5-6 Interaction between Fe particles (red) with the stray fields created by domain walls (green): (a) Bloch wall (out-plane domain wall magnetization) and (b) Néel wall (in-plane domain wall magnetization). The interaction affects the coercivity indirectly, via the influence of the defects.

qualitative explanation of the coercivity reduction is that the flux closure provided by the Fe particles affects the stray-field contribution to the domain-wall and smoother surface inhomogeneity, which are a major pinning mechanism [5.28]. The interaction effect is probably very small but sufficient to interfere with small coercivity of the alloy layers. Magnetostrictive contributions mediated by the SiO_2 may also play a role.

5.4 Summary

In this chapter, TM/Fe:SiO_2 bilayers for magnetic sensors have been produced and investigated. Each bilayer consists of a continuous TM layer and a layer of Fe particles embedded in SiO_2 matrix. All samples with Fe:SiO_2 top layers exhibit a reduction in coercivity and follow a similar trend as the Fe:SiO_2 grows thicker. Some samples also exhibit an improvement in permeability (NiFe, CoFeB), while some show no noticeable

permeability changes (CoFe). The best results are obtained for amorphous CoFeB layers, with a moderate improvement of the soft-magnetic performance. Our micromagnetic analysis shows that the magnetostatic coupling between the superparamagnetic Fe particles and TM layers is moderately strong, and a possible qualitative explanation of the improved soft-magnetic performance of the TM film is the absorption of domain-wall stray fields by the Fe particles.

5.5 References

[5.1] C. Albon, A. Weddemann, A. Auge, K. Rott, and A. Hutten, Applied Physics Letters **95** (2), 023101 (2009).

[5.2] S. Tsunegi, Y. Sakuraba, M. Oogane, Hiroshi Naganuma, K. Takanashi, and Y. Ando, Appl. Phys. Lett. **94** (25), 252503 (2009).

[5.3] S. Yuasa, J. of the Phys. Soci. Jpn. **77** (3), 031001 (2008).

[5.4] S. Yuasa and D. D. Djayaprawira, J. Phys. D: Appl. Phys. **40** (21), R337 (2007).

[5.5] R. A. McCurrie, *Ferromagnetic materials: structure and properties*. (Academic, London; San Diego, 1994).

[5.6] S. Edelstein and G. A. Fischer, J. Appl. Phys. **91** (10), 7795 (2002).

[5.7] R. Schad, H. Alouach, J. W. Harrell, M. Shamsuzzoha, and D. Wang, J. Appl. Phys. **93** (10), 8561 (2003).

[5.8] F. C. S. da Silva, W. C. Uhlig, A. B. Kos, S. Schima, J. Aumentado, J. Unguris, and D. P. Pappas, Appl. Phys. Lett. **85** (24), 6022 (2004).

[5.9] J. Hayakawa, S. Ikeda, Y. M. Lee, F. Matsukura, and H. Ohno, Appl. Phys. Lett. **89** (23), 232510 (2006).

[5.10] R. Zhang, R. Skomski, X. Z. Li, Z. Li, P. Manchanda, A. Kashyap, R. D. Kirby, S. H. Liou, and D. J. Sellmyer, J. Appl. Phys. **111**, 07D720 (2012).

[5.11] Z. Marinho, S. Cardoso, R. Chaves, R. Ferreira, L. V. Melo, and P. P. Freitas, J Appl Phys **109** (7), 07E521 (2011).

[5.12] S. H. Liou, R. Zhang, S. E. Russek, L. Yuan, S. T. Halloran, and D. P. Pappas, J. Appl. Phys. **103**, 07E920 (2008).

[5.13] R. Skomski, J. of Phys.: Conden. Matt. **15** (20), R841 (2003).

[5.14] I. A. Al-Omari and D. J. Sellmyer, Phys. Rev. B **52** (5), 3441 (1995).

[5.15] C. L. Platt, A. E. Berkowitz, S. David, Eric E. Fullerton, J. S. Jiang, and S. D. Bader, Appl. Phys. Lett. **79** (24), 3992 (2001).

[5.16] A. Zambano, H. Oguchi, I. Takeuchi, Y. Choi, J. Jiang, J. Liu, S. Lofland, D. Josell, and L. Bendersky, Phys. Rev. B **75** (14), 144429 (2007).

[5.17] C. L. Chien, Gang Xiao, S. H. Liou, J. N. Taylor, and A. Levy, J. Appl. Phys. **61** (8), 3311 (1987).

[5.18] C. Chien, L., Gang Xiao, and S. Liou, H., J. Phys. Colloques **49** (C8), C8 (1988).

[5.19] R. Skomski, M. L. Yan, Y. F. Xu, and D. J. Sellmyer, IEEE Transl. J. Magn. Jpn. **43** (6), 2163 (2007).

[5.20] G. Xiao, S. H. Liou, A. Levy, J. N. Taylor, and C. L. Chien, Phys. Rev. B **34** (11), 7573 (1986).

[5.21] R. Skomski, *Simple models of magnetism*. (Oxford University Press, Oxford ; New York, 2008), p.349.

[5.22] S. S. Malhotra, Y. Liu, J. X. Shen, S. H. Liou, and D. J. Sellmyer, J. Appl. Phys. **76** (10), 6304 (1994).

[5.23] Jr E. E. Huber, D. O. Smith, and J. B. Goodenough, J. of Appl. Phys. **29** (3), 294 (1958).

[5.24] R. Becker and W. Döring, *Ferromagnetismus*. (Springer, Berlin, 1939).

[5.25] T. Trunk, M. Redjdal, A. Kakay, M. F. Ruane, and F. B. Humphrey, J. Appl. Phys. **89** (11), 7606 (2001).

[5.26] A. Hubert and R. Schäfer, *Magnetic domains: the analysis of magnetic microstructures*. (Springer, Berlin ; New York, 1998), pp.696.

[5.27] J. S. Miller and M. Drillon, *Magnetism: molecules to materials*. (Wiley-VCH, Weinheim ; New York, 2001).

[5.28] A. A. Ivanov and V. A. Orlov, Phys. Solid State **53** (12), 2441 (2011).

Chapter 6 : Anisotropy and Micromagnetism of Fe/CrPt Bilayers

AFM $L1_0$-ordered CrPt is of interest as a pinning material in exchange-biased systems due to its high blocking temperature, simple hysteresis loops and high corrosion resistance [6.1]. Moreover, compared to Mn atoms in presently used Mn-based alloys, Cr undergoes much less harmful interdiffusion during heat treatment [6.1-3]. Thin films of $L1_0$ phase CrPt with a (001) texture have also been used as an underlayer to promote the $L1_0$ phase formation of materials such as FePt [6.4, 6.5], which is of great importance in magnetic recording media [6.6, 6.7]. Therefore, it is important to control and understand both the formation of the $L1_0$ phase and the texture with which it grows.

In addition to the mentioned practical applications of $L1_0$-ordered CrPt, the spin structure and micromagnetism of this intriguing system is not fully understood, and little is known about its magnetocrystalline anisotropy. Figure 6-1 shows the schematic crystal structure and spin configuration of $L1_0$-ordered CrPt, based on neutron diffraction [6.8].

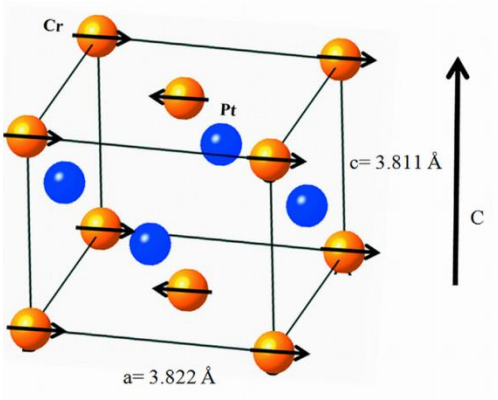

Figure 6-1 Schematic crystal structure and spin configuration of $L1_0$ CrPt. The preferential magnetization direction is in the basal plane

Each Cr atom carries a moment of 2.24 ± 0.15 μ_B, with AFM alignment between nearest

neighbors in the (001) planes, whereas the contribution from the Pt is very small [6.8, 6.9] Preliminary research into the anisotropy has led to an experimental estimate of 10 kJ/m^3 by measuring the exchange bias in an FeCo/CrPt bilayer system and using Eq. 2.16 and 2.17 [6.1, 6.10]. This value is much smaller than the theoretical predication of 3500 kJ/m^3 [6.11]. The fundamental reason for this discrepancy is the oversimplification of the model used to extract the experimental value, using Eq. 2.16 and 2.17 [6.12]. However, even if the model could perfectly describe the relation between exchange bias and AFM anisotropy, this method may still not be accurate due to its incomplete exchange coupling between the bilayers, which may mimic a strongly reduced anisotropy. As described in Chapter 1, Fe thin films can be used as a probe to approach measurement of the anisotropy of AFMs.

In this chapter, the method of introducing exchange bias using MA and its limitations are examined. A systematic study of the effect of deposition and processing conditions on $L1_0$ phase formation in CrPt thin films is performed and an investigation of the resulting anisotropy using magnetic measurements of an exchange-coupled CrPt/Fe system will be presented.

6.1 Experiment Methods

CrPt is AFM only when it is in its $L1_0$ phase. It has been demonstrated that its easy axis lies in the basal plane of the crystal lattice as illustrated in Figure 6-1 [6.8, 6.11] Therefore, it is important to achieve highly textured $L1_0$ phase CrPt thin films in order to analyze the anisotropy of the specimen. As in the case of $L1_0$-ordered FePt, heat

treatments either during the deposition or post-deposition are required to achieve the phase formation and (001) texture [6.13-15].

6.1.1 Sample Preparation

The AJA magnetron sputtering system described in Section 3.1.5 was used to prepare the samples in this study. The base pressure of the system is on the order of 10^{-8} Torr for all samples. Silicon substrates with 1 μm thermally oxidized layer along with the sample holders were baked at 60 °C before transferring into the load-lock chamber of the sputtering system. The load-lock chamber was then pumped over one hour. Further pumping would yield only minor improvements of the chamber vacuum in the chamber.

The $L1_0$ Phase CrPt can be achieved by post-annealing the $[Cr/Pt]_n$/FM stack structure deposited on Si substrates above 350 °C for 5 hours, however, all the films were highly (111) textured [6.1, 6.10]. In order to achieve the (001) texture, different approaches were applied in this study. Three series of thin-film samples (labeled A, B, and C) were prepared, as illustrated in Figure 6-2 (a) and (b). The samples of Series A

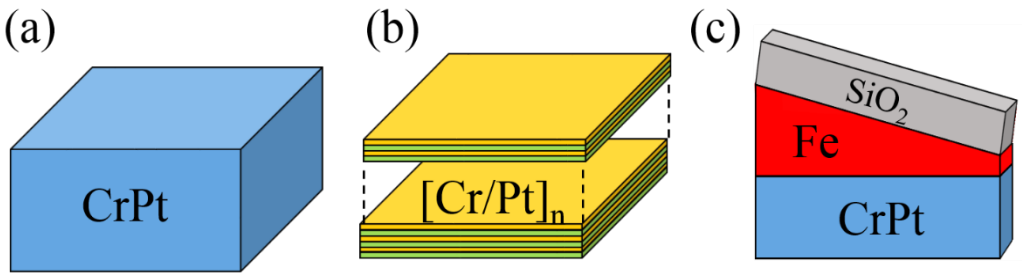

Figure 6-2 Schematic diagram of sample structures of (a) series A, (b) series B and (c) series C with Fe wedge

were deposited at room temperature by co-sputtering from pure Cr and Pt targets. The deposition rate and time were set in such a way that the sample has a 1:1 atomic ratio. Series B was also deposited at the room temperature in a multilayer structure of [Cr(x

Å)/Pt(1.7 Å)]$_n$ which has a much thinner bilayer structure compared with the one used in previous study [6.1]. Sample series C was prepared using the same method as sample A, but the deposition was carried at elevated temperatures ranging from 300 °C to 800 °C. The sample was kept inside the load-lock until it reached room temperature. The total thickness of CrPt for all samples is kept at 40 nm, above the critical thickness of 12.5 nm [6.1]. In order to probe the anisotropy of the AFM CrPt layer, an additional co-sputtered sample deposited at 600 °C was capped at the room temperature with an iron wedge. Table 6-1 lists the different sample deposition conditions for different sample series.

Table 6-1 Summary of different sample deposition condition

Sample ID	Sample Structure	Substrate Temperature
A	Co-sputtering	RT
B	Multilayer	RT
C	Co-sputtering	up to 800 °C

The samples in Series A and B were annealed by either RTA or CF in H_2/Ar forming gas environment to establish the $L1_0$ phase. For the RTA process, temperature was ramped up to 800 °C with a 100 °C per sec ramping speed. The sample stayed at the target temperature for 5 min and then quickly cooled down to room temperature. For the CF process, the temperature ramping took a much slower path and stayed at the target temperature for 5 hours. The sample was then naturally cooled down to room temperature. No heat treatment was carried for the samples with the Fe wedge structure.

The MTJ sample used to investigate the annealing effect on exchange bias was prepare at National Institute of Standards and Technology with the following structure: Ta(5nm) / Cu(5nm) / $Ir_{20}Mn_{80}$(10nm) / $Co_{90}Fe_{10}$(2nm) / Ru(0.85nm) / $Co_{60}Fe_{20}B_{20}$ (3nm)/

Al_2O_3(1.4nm) / $Co_{90}Fe_{10}$ (2nm) / $Ni_{80}Fe_{20}$(28nm) /Ta(5nm) / Ru(5nm). Sixteen ellipse shape junctions were connected serially and the resistance is of the order of kilo-ohm.

6.1.2 Sample Characterization Technique

The thicknesses of all samples were estimated through XRR measurements. Figure 6-3(a) shows a series of XRR measurement along the Fe wedge direction. The drifting of the measurement curves clearly shows the evolution of the thickness throughout the sample. The thickness variation over the thin film is estimated using XRR measurements, as shown in Figure 6-3(b). The figure suggests that the thickness of the Fe wedge ranges from 4 nm up to 9 nm. The binary Cr-Pt equilibrium phase diagram indicates the $L1_0$

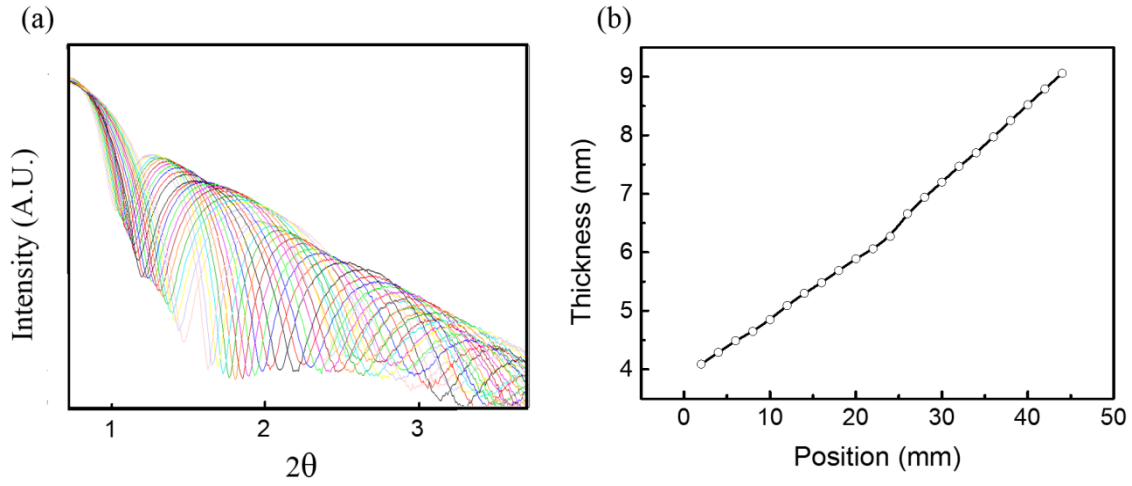

Figure 6-3 (a) XRR measurements of Fe wedge, curves with different color represents different location. (b)Thickness variation of Fe wedge estimated from XRR measurements

phase CrPt can be achieved for certain Cr and Pt ratio [6.16]. The composition of the CrPt was measured with by doing EDS measurement in the SEM. The phase formation and texture of CrPt were characterized by XRD and TEM, while the magnetic measurements were performed using AGFM and SQUID.

The MTJ samples were connected to the HTRMS described in Section 3.9.2 which can be heated up to 350 °C and where a magnetic field up to 10 kOe can be applied. Different factors, such as magnetic field, annealing time and annealing temperature, affect to the MTJ during MA process. The current is supplied by a current source and the voltage was measured by a nanovoltmeter. The high-resistance (R_{ap}) and low-resistance (R_p) states were recorded and the tunneling MR ratio was defined as $TMR = \frac{R_{ap}-R_p}{R_p}$.

6.2 CrPt $L1_0$ Phase Formation and Texture Analyses

Figure 6-4(a) shows the x-ray diffraction spectra for the A and B samples that were processed at different temperatures in the CF. The as-deposited samples show a strong (111) texture. For samples annealed at 400 °C, the (111) peak shifts slightly to a lower angle. This peak shift upon annealing indicates the formation of the $L1_0$ phase, which has larger lattice spacing along the body diagonal [6.17]. The sample is still highly (111) textured with no sign of a (001) peak. Only after the annealing temperature exceeds 500 °C does the $L1_0$ phase (001) peak appear along with the (200)/(002) peak, and the intensity of those peaks becomes quite pronounced as the annealing temperature increases. These XRD patterns indicate that the $L1_0$ phase formation for post-deposition annealed co-sputtered films (series A) and multilayer films (series B) follow a similar trend. The advantage of using RTA has been described in Chapter 3, and the use of layer structure in FePt has been demonstrated to be effective in promoting (001) texture on amorphous substrate [6.18,19]. As shown in Figure 6-4 (b), even with a significantly shortened annealing time, $L1_0$ phase CrPt can still be formed for both series and the phase formation follows the same trend as samples that were annealed using CF.

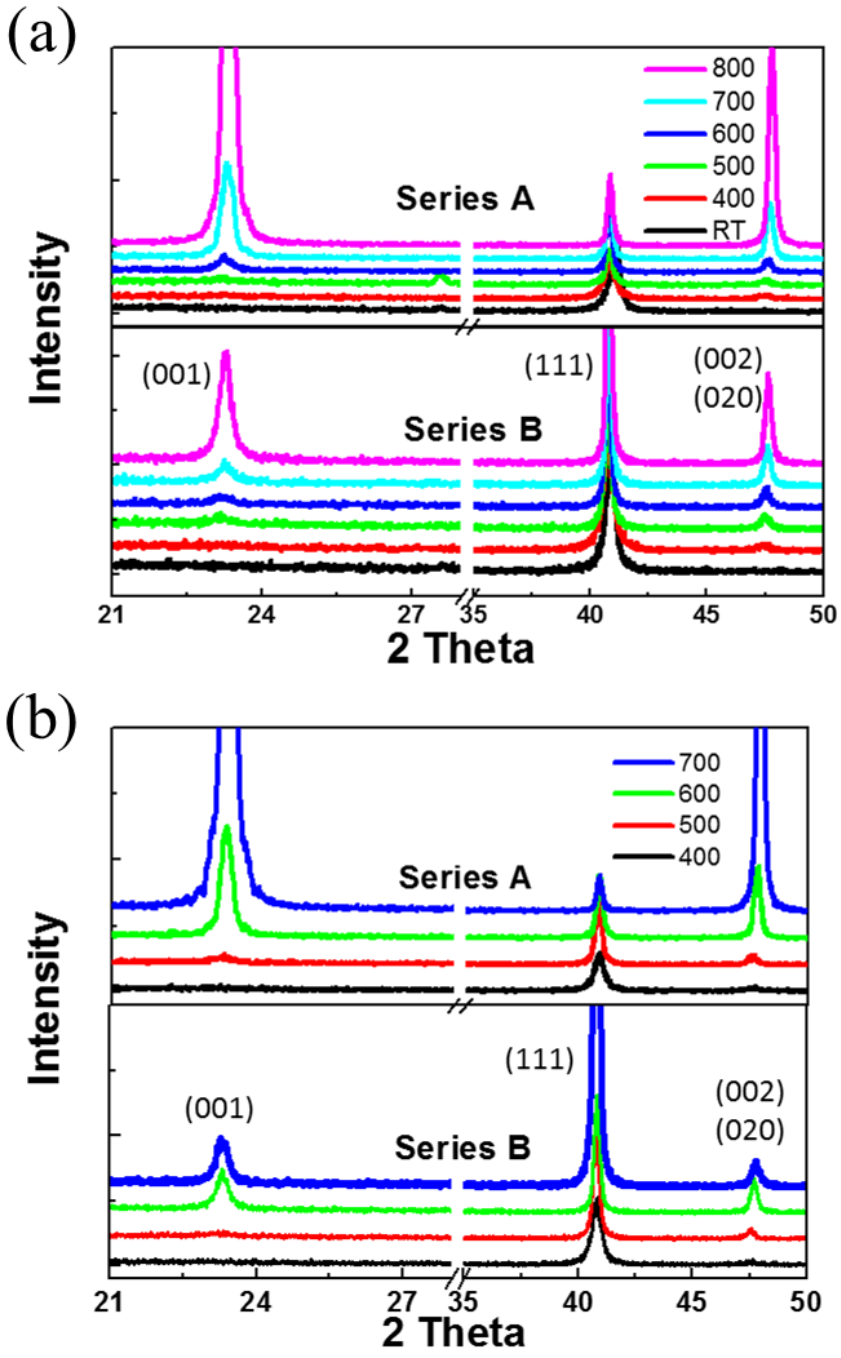

Figure 6-4 XRD measurement of sample Series A and B, (a) annealed using CF and (b) annealed using RTA.

It can also be seen from Figure 6-4(a) that the degree of texture is quite different between series A and B. Through estimating the peak intensities, sample series A shows

higher quality texture than sample series B does for any given annealing temperature. Similarly, the degree of $L1_0$ order and (001) texture appear more prevalent in series A than in series B. Samples annealed using RTA share the same tendency as demonstrated in Figure 6-4(b). However, this difference is most pronounced in the samples annealed using CF. Unlike FePt, the stack structure did not seem to help promoting the (001) texture of $L1_0$ phase CrPt [6.18]. This is likely due to the fact that the interdiffusion between Cr and Pt is very difficult and only actively occurs at temperature above 500 °C [6.20].

For the sample series C, which is deposited at elevated temperatures, the $L1_0$ phase can be formed at temperature as low as 300 °C. However, samples deposited below 500 °C show strong out-of-plane (111) texture, Figure 6-5(a), which is similar to the post-annealing samples from series A and B. Although the (001) peak is present in samples deposited above 600 °C, with an intensity increasing with temperature, the ratios with the (002) and (111) peaks do not indicate a high degree of $L1_0$ order or (001) texture, respectively. A selected-area-electron-diffraction (SAED) pattern was taken on the sample deposited at 600 °C (Figure 6-5(b)). A calculated polycrystalline pattern was produced by Dr. Li using the PCED2.0 program [6.21], in which the (001) texture is simulated based on the March model [6.22]. Within this model, crystalline texture is quantified by the parameter r, where $r = 0$ corresponds to perfect texture and $r = 1$ to fully random orientation. The March parameter for this sample is estimated to be $r = 0.65$. This result suggests that roughly 60% of the c-axis of CrPt is within 60° to 90° of the film plane normal for this particular sample. The sample deposited at 800 °C does not show improvement in crystallinity, but the average grain size is increased from about 50 nm to

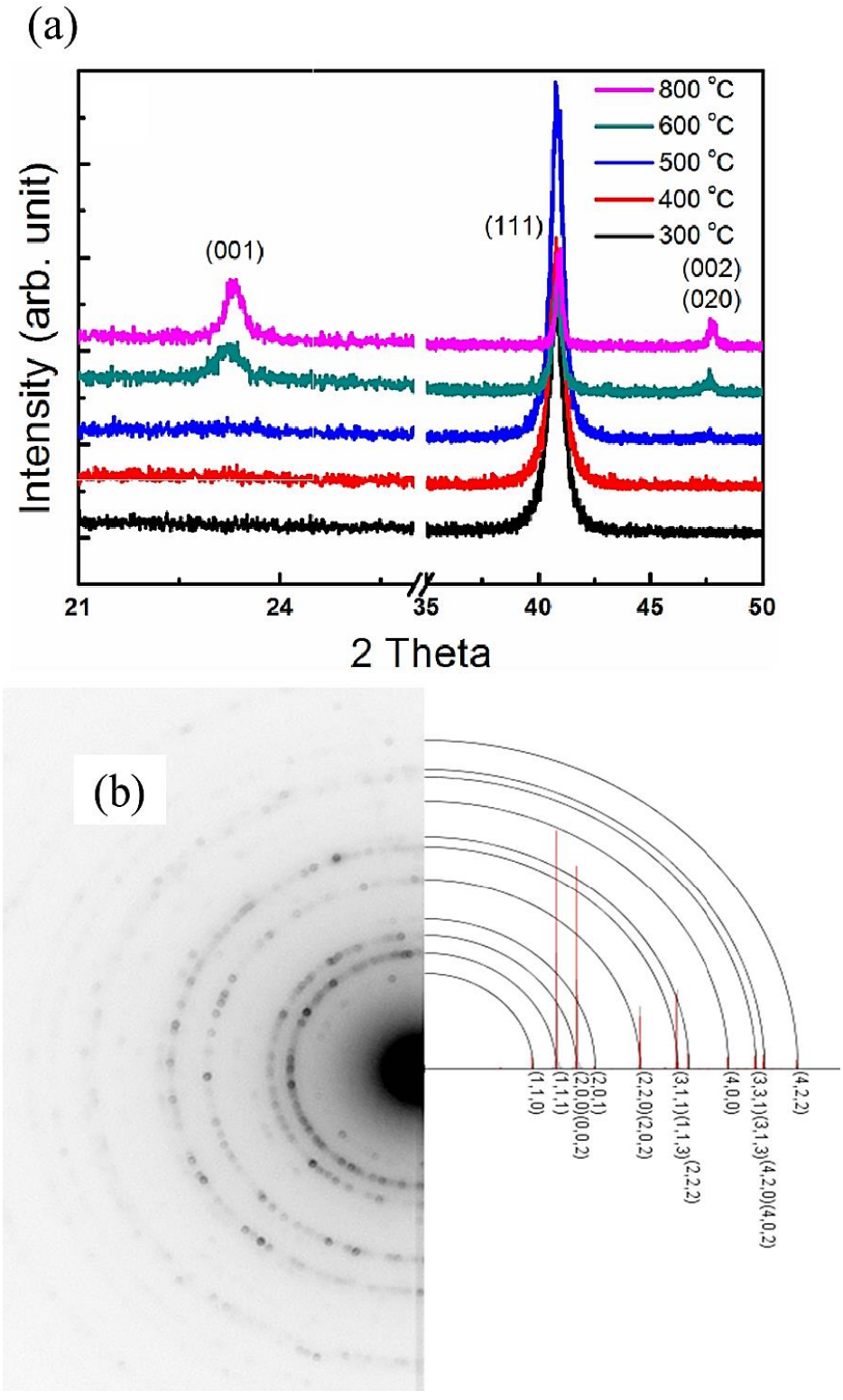

Figure 6-5 (a) XRD measurement of sample Series C and (b) SAED diagram of CrPt deposited at 600 °C

roughly 200 nm, as shown in Figure 6-6. As mentioned in Section 2.1.5, the effect of the

grain size on the anisotropy of the AFM is not conclusive, and therefore, a sample deposited at 600 °C was used for anisotropy estimation in order to minimize the surface

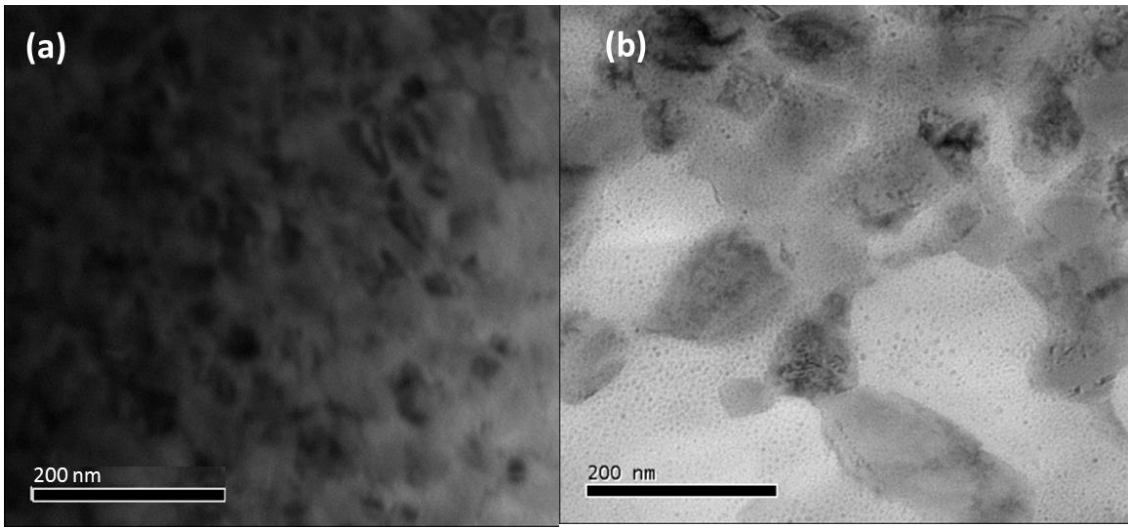

Figure 6-6 TEM images of CrPt deposited at (a) 600 °C and (b) 800 °C. The average grain size increased from 50 nm to roughly 200 nm

roughness while maintaining a reasonably good crystallinity [6.23-25].

6.3 Probing the Anisotropy of $L1_0$-ordered CrPt

6.3.1 Preparation of the Bilayer Structure

Although post-annealed samples show far superior (001) texture than samples deposited at high temperatures, a well-defined exchange interaction cannot be established due to the destruction of AFM/FM interface [6.26, 6.27]. A post-annealed sample from series A was deposited with CoFe at room temperature. It was then annealed at 350 °C for one hour under an external magnetic field of 10 kOe. The hysteresis loops, before and after the MA, show no apparent loop shift or coercivity change. The exchange bias could not be established when the FM layer is deposited on post-annealed samples once the chamber vacuum is broken. Therefore, the interface quality is crucial for forming

AFM/FM exchange interaction. The FM layer must be deposited after the $L1_0$ phase CrPt is formed in-situ.

6.3.2 Probing the Anisotropy Using E_{eb}

In this experiment, a CrPt thin film deposited at 600 °C was coated with a 5 nm Fe thin film at room temperature without breaking the vacuum. The sample was then annealed in a 10 kOe magnetic field at 350 °C for one hour. After naturally cooling down to room temperature, the sample was measured using VSM at different temperatures. As shown in the inset of Figure 6-7, the room temperature hysteresis loop exhibits a pronounced loop shift and the coercivity drastically increased compared to pure Fe. This is a direct indication of the establishment of exchange bias. The exchange bias field is around 300 Oe, and by using Eq. 2.16 and 2.17, the anisotropy of CrPt is estimated to be

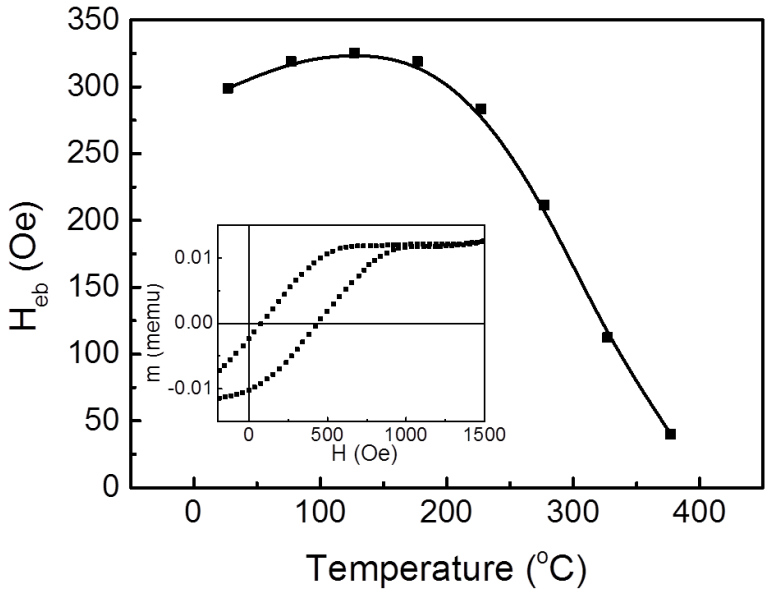

Figure 6-7 Temperature dependence of exchange bias field of sample with CrPt/Fe bilayer structure after MA. The inset shows the hysteresis loop measured at the room temperature

10.6 kJ/m^3. This is far below the theoretical prediction of 3500 kJ/m^3 done by Dr. Manchanda [6.11]. Figure 6-7 also shows that the exchange bias of the system remains

almost constant up to 200 °C. Above this temperature, the exchange bias decrease and vanishes before reaching its blocking temperature of 600 °C [6.1].

6.3.3 Limitations of the H_{eb} Method

The discrepancy between theory and experiment has its origin in the very crude modeling of the exchange bias, as outlined in Section 2.1.5. In particular, the MA process is a crucial step for introducing exchange bias in the FM/AFM bilayer system. It is also important to anneal the system above the blocking temperature of the AFM layer in order to achieve maximum exchange anisotropy [6.28].

The TMR ratio is the direct evidence of the annealing effect on the MTJ, and setting the exchange bias for AFM/FM bilayer is the main purpose of the magnetic annealing. As shown in Figure 6-8, when the MTJ sample was annealed at different

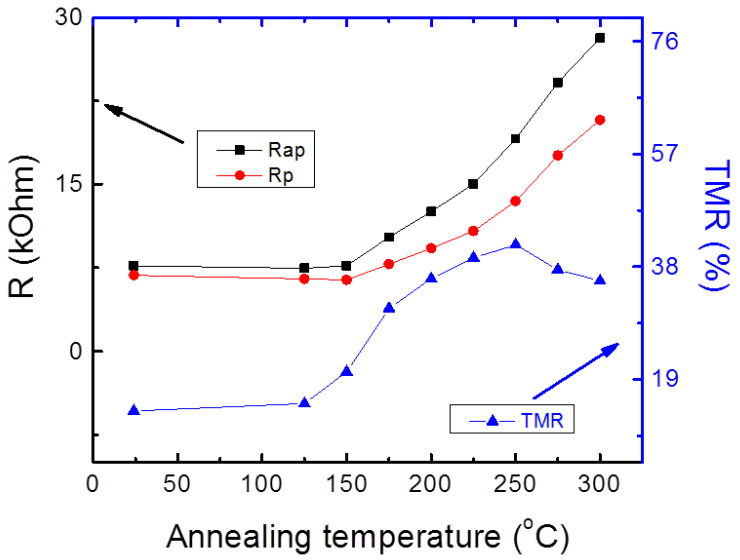

Figure 6-8 The temperature dependence of R_{ap}, R_p and TMR. The drop of TMR at high annealing temperature might due to interdiffusion of IrMn layer

temperatures under a 10 kOe magnetic field for 30 min, the TMR ratio kept increasing

until it reach 250 °C which is the typical blocking temperature for the IrMn system [6.29]. As the temperature further increases, the TMR starts to deteriorate, which is likely due to the interdiffusion between IrMn and its adjacent layers [6.30, 6.31]. It is, therefore, important to anneal the sample above the blocking temperature to maximize the exchange bias, yet low enough to prevent any interdiffusion.

Figure 6-9 shows how the properties of the MTJ depend on the annealing time. The R_{ap}, R_p and TMR increase with the increasing annealing time, but the TMR appears to saturate after 8 min annealing while both R_{ap} and R_p keep increasing. The increasing resistance in the MTJ would enhance the noise level of the system, which is not desired [6.32]. Therefore, it is beneficial to control the annealing time within a certain time frame to minimize the resistance increase of the system. Shorter annealing can also effectively

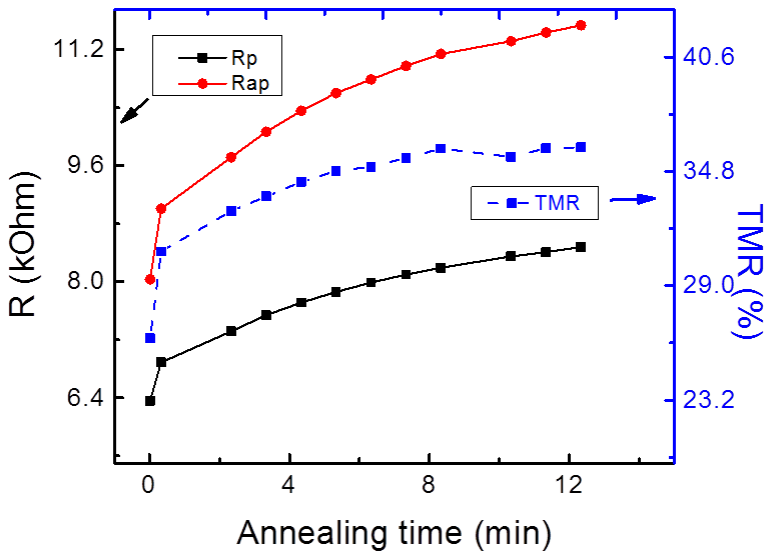

Figure 6-9 The annealing time dependence of Rap, R_p and TMR.
Note resistance keep increasing with increasing annealing time.

minimize the harmful interdiffusion during the annealing process.

Exchange bias can be introduced by a magnetic field of 10 kOe or less during the annealing (Figure 6-10). However, to fully develop the exchange bias, one needs a field that exceeds 1 kOe.

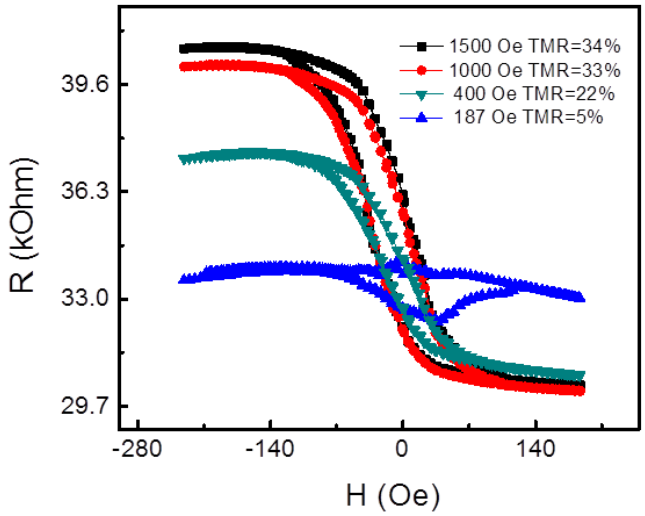

Figure 6-10 Applied magnetic field dependence of MR loop. 1 kOe is sufficient to set the exchange bias.

Overall, the exchange bias can be established shortly after the system reaches its annealing temperature, in this case after 8 minutes. The magnetic field required is determined by the saturation magnetization of the FM layer that is adjacent to the AFM layer of the bilayer system. It is important to anneal the system above the blocking temperature of the AFM layer in order to maximize the exchange anisotropy.

As mentioned above, the blocking temperature of $L1_0$-ordered CrPt is much higher than the MA temperature used in this study. The exchange bias vanished at the vicinity of the annealing temperature which clearly indicates that the exchange interaction between Fe and CrPt layers is only partial. This leads to an experimental underestimation of the CrPt anisotropy. On the other hand, it is also difficult to magnetically anneal the bilayer

structure above the blocking temperature of AFM material without introducing structural changes inside the system.

6.3.4 Probing the CrPt Anisotropy Using H_c

Section 2.1.5 suggests that the anisotropy can be estimated by adding an Fe layer. An Fe wedge has been deposited on the 40 nm $L1_0$ phase CrPt. Figure 6-11(a) shows that the in-plane hysteresis loops for samples without MA are nearly rectangular. As the Fe thickness decreases, the coercivity (H_c) of the system increases from around 12 to 42 mT. The perpendicular hysteresis loops, as shown in Figure 6-11(b), reveal a two-step transition in the hysteresis for Fe layers thicker than 6 nm, below which the signal

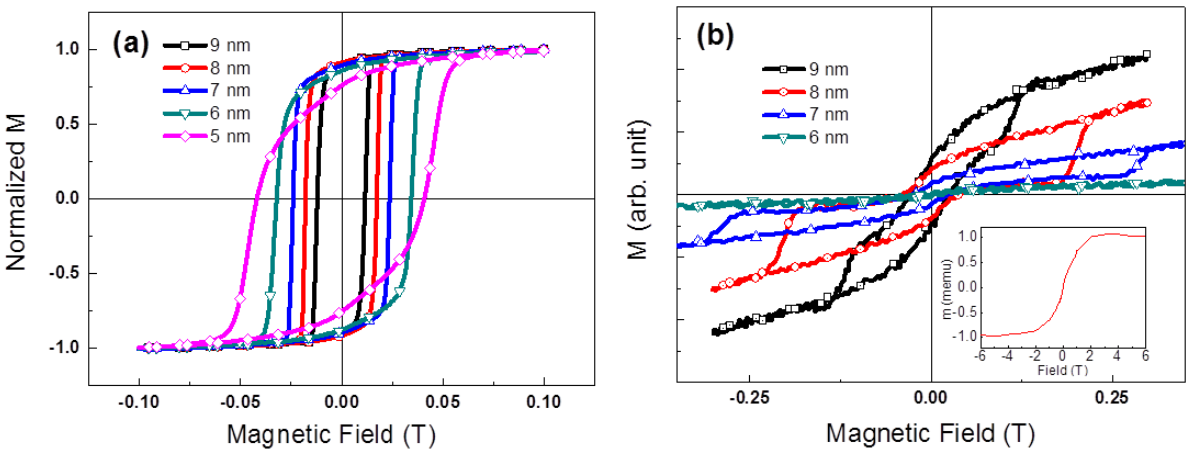

Figure 6-11 In-plane (a) and perpendicular (b) hysteresis loop of CrPt/Fe as a function of Fe-layer thickness measured by AGFM. The inset shows the hysteresis loop measured by SQUID

becomes a straight line. The step on each side of the curve is due to the coherent rotation for FM spins that are pinned 90° from the applied field [6.33]. The hysteretic field or "coercivity" (H_c) of these hysteresis loops varies from 0.12 T to 0.28 T as the thickness of Fe decreases. These coercivities are much larger than in a typical Fe thin film and can be

viewed as a result of AFM/FM exchange interaction. As shown in the inset of Figure 6-11(b), the perpendicular hysteresis loop could not be saturated until the external field reached 2 T.

Figure 6-11 suggests that the CrPt exhibits a substantial anisotropy, much higher than the previously estimated anisotropy constant of 10.6 kJ/m. An estimate for the anisotropy is obtained by equating H_c in Figure 6-11(b) with the anisotropy field H_A as suggested in Section 2.1.5. Since the magnetization and the anisotropy originate nearly exclusively from the Fe and the CrPt, respectively, we can write

$$H_{CrPt} \approx H_c = \frac{2K_{CrPt}t_{CrPt}}{\mu_0 M_{Fe} t_{Fe}} \tag{6.1}$$

where t is the thickness of each layer and M_{Fe} is the magnetization of Fe.

Thicker Fe layers would normally yield less reliable estimation, because the Fe magnetization gets more and more inhomogeneous as the Fe thickness increases, and this effect is not included in Eq. 6.1. Using $\mu_0 H_c$= 0.28 T, t_{CrPt}= 40 nm, and t_{Fe} = 7 nm, one can obtain K_{CrPt}= - 438 kJ/m^3. The anisotropy estimate using this method is much closer to the theoretical calculation, compared with the results from the other method.

6.3.5 Origin of the Discrepancy

Although the complications introduced by the MA are eliminated, there are still several factors that would influence the experimental results. First, the assumption made in Eq. 6.1 is coherent rotation of the magnetic moment in the Fe thin film [6.34]. In this approximation, the coercivity field is equivalent to the anisotropy field. However, as described in Section 2.3.3, coercivities encountered in practice are more complicated. For instance, imperfections, both chemical and magnetic, could promote nucleation sites for

reversed-magnetization domains which bypass the anisotropy of the system. Hence the experimental coercivity fields are generally much smaller than the anisotropy fields, often by one or two orders of magnitude [6.35, 6.36]. Second, the texture analysis in Section 6.2 shows that a substantial fraction of the grains is misaligned, which could also reduce the coercivity. Note that the easy axis of $L1_0$ phase CrPt lies in the *a*-*b* plane and any deviation from this would cause a change in anisotropy [6.11]. Figure 6-12 illustrates this point by showing typical spin structures in the Fe/CrPt system [6.11]. If the a-b plane is 45^o according to the film surface, the spin configurations of (a) and (b) are equivalent to the AFM film. However, it would yield different exchange interaction with FM spins which cause the induced anisotropy of the FM spins to be orthogonal to each other in these two configurations. Consequently, the *c*-axis misalignment would translate into the coercivity of the bilayer system, even if $K_1 < 0$ which led to the hysteresis loops showed

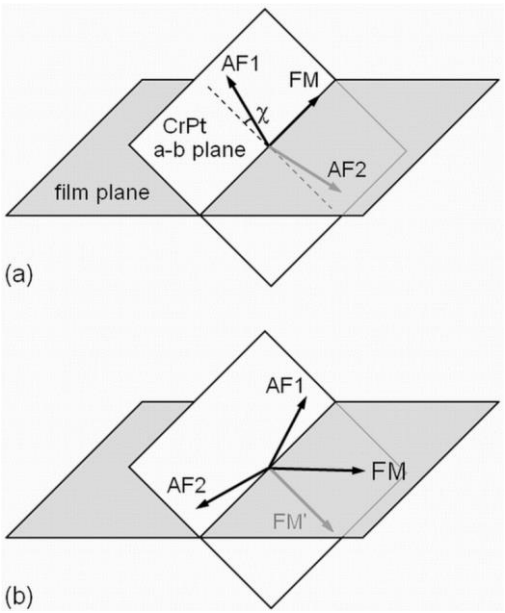

Figure 6-12 Effect of spin structure misalignment on CrPt/Fe system. (a) and (b) are two equivalent AFM spin configuration

in Figure 6-11(b). This micromagnetic feature further contributes to the reduction of H_c.

6.4 Conclusions

$L1_0$-ordered AFM CrPt with (001) texture can be formed in samples either deposited or annealed at temperature above 600 °C. The anisotropy of $L1_0$ phase CrPt has been estimated using Fe as a probe. The experimentally deduced value of - 0.438 MJ/m^3 is still significantly smaller than the theoretical prediction of - 3.5 MJ/m^3. The disagreement is explained by the deviations from the SW behavior and by the misalignment of the CrPt crystal structure.

6.5 References

[6.1] B. Dai, J. W. Cai, W. Y. Lai, Y. K. An, Z. H. Mai, F. Shen, Y. Z. Liu, and Z. Zhang, Appl. Phys. Lett. **87** (9), 092506 (2005).

[6.2] J. H. Lee, H. D. Jeong, C. S. Yoon, C. K. Kim, B. G. Park, and T. D. Lee, J. Appl. Phys. **91** (3), 1431 (2002).

[6.3] G. W. Anderson, M. Pakala, and Y. M. Huai, IEEE T. Magn. **36** (5), 2605 (2000).

[6.4] J. L. Tsai, Y. C. Lin, and C. J. Hsu, J. Phys. D: Appl. Phys. **41** (2), 025002 (2008).

[6.5] X. Y. Wang, H. Wang, H. W. Jiang, P. J. Wang, and J. L. Wang, J. Nanosci. Nanotechno. **12** (2), 1032 (2012).

[6.6] D. J. Sellmyer and R. Skomski, Advanced Magnetic Nanostructures (Springer, New York, 2009).

[6.7] A. T. McCallum, P. Krone, F. Springer, C. Brombacher, M. Albrecht, E. Dobisz, M. Grobis, D. Weller, and O. Hellwig, Appl. Phys. Lett. **98** (24), 242503 (2011).

[6.8] S. J. Pickart and R. Nathans, J. Appl. Phys. **34** (4), 1203 (1963).

[6.9] A. Kashyap, R. Skomski, A. K. Solanki, Y. F. Xu, and D. J. Sellmyer, J. Appl. Phys. **95** (11), 7480 (2004).

[6.10] R. Zhang, M.S. Thesis, University of Nebraska-Lincoln, 2006.

[6.11] R. Zhang, R. Skomski, X. Z. Li, Z. Li, P. Manchanda, A. Kashyap, R. D. Kirby, S. H. Liou, and D. J. Sellmyer, J. Appl. Phys. **111**, 07D720 (2012).

[6.12] J. Nogués and Ivan K. Schuller, J. Magn. Magn. Mater. **192** (2), 203 (1999).

[6.13] K. Yano, V. Nandwana, N. Poudyal, C. B. Rong, and J. P. Liu, J. Appl. Phys. **104** (1), 013918 (2008).

[6.14] S. Ishio, T. Narisawa, S. Takahashi, Y. Kamata, S. Shibata, T. Hasegawa, Z. Yan, X. Liu, H. Yamane, Y. Kondo, and J. Ariake, J. Magn. Magn. Mater. **324** (3), 295 (2012).

[6.15] C. Brombacher, C. Schubert, K. Neupert, M. Kehr, J. Donges, and M. Albrecht, J. Phys. D: Appl. Phys. **44** (35), 355001 (2011).

[6.16] R. Süss, L. A. Cornish, and M. J. Witcomb, J. Alloys Compd. **490** (1–2), 124 (2010).

[6.17] K. Aimuta, K. Nishimura, S. Hashi, and M. Inoue, presented at the Magnetics Conference, 2005. INTERMAG Asia 2005. Digests of the IEEE International, 2005 (unpublished).

[6.18] T. A. George, Z. Li, M. L. Yan, Y. Xu, R. Skomski, and D. J. Sellmyer, J. Appl. Phys. **103** (7), 07D502 (2008).

[6.19] S. N. Hsiao, S. H. Liu, S. K. Chen, T. S. Chin, and H. Y. Lee, Appl. Phys. Lett. **100** (26), 261909 (2012).

[6.20] S. D. Mukherjee, D. V. Morgan, and M. J. Howes, J. Electrochem. Soc. **126** (6), 1047 (1979).

[6.21] X.Z. Li, Ultramicroscopy **110** (4), 297 (2010).

[6.22] P. G. Fazey, B. H. Oconnor, and L. C. Hammond, Clay Clay Miner **39** (3), 248 (1991).

[6.23] X. Zheng, C. Xu, K. Nishikubo, K. Nishiyama, W. Higemoto, W. Moon, E. Tanaka, and E. Otabe, Phys. Rev. B **72**, 014464 (2005).

[6.24] C. Mitsumata, A. Sakuma, K. Fukamichi, M. Tsunoda, and M. Takahashi, J. Phys. Soc. Jpn. **77** (4), 044602 (2008).

[6.25] M. Fitzsimmons, D. Lederman, M. Cheon, H. Shi, J. Olamit, Igor Roshchin, and Ivan Schuller, Phys. Rev. B **77**, 224406 (2008).

[6.26] J. V. Kim, L. Wee, R. L. Stamps, and R. Street, IEEE Transl. J. Magn. Jpn. **35** (5), 2994 (1999).

[6.27] A. E. Berkowitz and Kentaro Takano, J. Magn. Magn. Mater. **200** (1–3), 552 (1999).

[6.28] H. Kurt, K. Rode, H. Tokuc, P. Stamenov, M. Venkatesan, and J. M. D. Coey, Appl. Phys. Lett. **101** (23), 232402 (2012).

[6.29] G. Anderson, Y. M. Huai, and L. Miloslawsky, J. Appl. Phys. **87** (9), 6989 (2000).

[6.30] Kebin Li, Zaibing Guo, Guchang Han, Jinjun Qiu, and Yihong Wu, J. Appl. Phys. **93** (10), 6614 (2003).

[6.31] S. J. Joo, J. Appl. Phys. **95** (11), 7522 (2004).

[6.32] S. H. Liou, R. Zhang, S. E. Russek, L. Yuan, S. T. Halloran, and D. P. Pappas, J. Appl. Phys. **103**, 07E920 (2008).

[6.33] A. Tillmanns, S. Oertker, B. Beschoten, G. Guntherodt, C. Leighton, I. K. Schuller, and J. Nogues, Appl. Phys. Lett. **89**, 202512 (2006).

[6.34] D. Givord, M. F. Rossignol, and D. W. Taylor, J Phys Iv **2** (C3), 95 (1992).

[6.35] R. Skomski and J. M. D. Coey, *Permanent magnetism*. (Institute of Physics Pub., Bristol, UK ; Philadelphia, PA, 1999), p.404.

[6.36] R. Skomski, J. Phys.: Condens. Matter **15** (20), R841 (2003).

Chapter 7 : Summary and Outlook

In this thesis, interaction effects in several iron-based magnetic nanostructures have been investigated. This includes the Kondo effect in isolated Cu(Fe) clusters, magnetostatic interaction in TM / Fe:SiO_2bilayer systems and exchange interactions in Fe/CrPt bilayer systems. All systems being investigated are either fundamentally interesting or practically useful.

7.1 Diluted Magnetic System in Confined Clusters

We have investigated how the confinement of the screening cloud affects the Kondo effect. In contrast to earlier approaches, where metallic leads distort rather than confine the Kondo screening cloud, the embedding of the Fe-containing Cu clusters in SiO_2 matrix ensures that the Kondo screening cloud is truly confined to the size of the nano-particle. Since resistance measurements cannot be used to measure this nano-particle Kondo effect, magnetic susceptibility measurements have been used to achieve this goal. In agreement with theoretical predictions, the confinement reduced the strength of the Kondo interaction. Although RKKY interactions between Fe impurities cannot be completely ruled out, it is estimated to yield only a very small correction for the whole system.

One suggestion for future researches is to systematically vary the size of the isolated particles through different deposition conditions and patterning methods up to the Kondo screening cloud dimension. It could provide crucial information regarding the formation of the Kondo screening cloud.

7.2 Pursuing a Low Coercivity Soft Magnetic Layer

Controlling the hysteretic behavior of soft magnetic layers in sensors is an important technological challenge. Although different from the exchange-spring mechanism, the reversibility of the FM layer can be improved through the magnetostatic interaction between adjacent layers of FM and superparamagnetic materials. All samples showed clear reduction of coercivity regardless the present of induced magnetic anisotropy. For certain samples, improvement for permeability was also observed up to a factor of 5. Such improvements were attributed to the absorption of domain-wall stray fields by the Fe particles which effectively smoothed the magnetic surface of the soft magnetic layer. This mechanism offers a new angle to improve the free layer properties for magnetic sensors application. The superparamagnetic layer can serve as a recovering layer to decrease hysteresis of the free layer due to surface roughness or defects.

Suggestions for future work are the contribution of magnetostrictive effects and the implementation of such structure into the existing magnetic sensor system could also be a challenging topic.

7.3 Probing Anisotropy of AFM Materials

Measuring the anisotropy of an AFM material is not always straightforward especially when the Néel temperature of the material is very high, such as in $L1_0$-ordered CrPt. Commonly used methods that utilize the exchange bias field lead to strongly underestimated AFM anisotropy value. The enhanced coercivity of the exchange bias system was used to address this problem by avoiding the complication introduced by the magnetic annealing. With an additional Fe layer on the top, the exchange interaction

between CrPt and Fe drastically increased the coercivity of Fe and the anisotropy of $L1_0$-ordered CrPt was determined to be - 0.438 MJ/m^3 which is a significant improvement from previous experimental estimation. This anisotropy appears to be significantly lower than the theoretical prediction of $L1_0$ phase CrPt; the disagreement may largely come from the deviation from Stoner-Wohlfarth behavior and the misalignment of CrPt crystal structure.

Concerning future researches, it should be noted that the micromagnetism of AFM materials is still not well established. Experimentally, it may be interesting to improve the (001) texture of the $L1_0$ phase CrPt through lattice matching by using either a MgO or $LaAlO_3$ single-crystal substrate.

Appendix 1 ABBREVIATIONS

AGFM	Alternative Gradient Force Magnetometer
AFM	Antiferromagnetic, Antiferromagnet
CA	Conventional Annealing
CF	Conventional Furnace
DC	Direct Current
EM	Electron Microscope
EDX	Energy-Dispersive X-ray Spectroscopy
FM	Ferromagnetic, Ferromagnet
GMR	Giant Magnetoresistance
GADDS	General Area Detector Diffraction System
HTRMS	High Temperature Resistance Measurement System
MA	Magnetic Annealing
MFC	Magnetic Flux Concentrator
MTJ	Magnetic Tunneling Junction
MR	Magnetoresistance
MR-FORC	Magnetoresistive FORC
MFT	Mean Field Theory
NRG	Numerical Renormalization Group
PPMS	Physical Property Measurement System
RF	Radio Frequency
RTA	Rapid Thermal Annealing

RSO	Reciprocating Sample Option
RKKY	Ruderman-Kittel-Kasuya-Yosida
SEM	Scanning Electron Microscopy
STM	Scanning Tunneling Microscopy
SAED	Selected Area Electron Diffraction
SW	Stoner-Wohlfarth
SQUID	Superconducting Quantum Interference Devices
TM	Transition Metal
TEM	Transmission Electron Microscopy
TMR	Tunneling Magnetoresistance
VSM	Vibrating-Sample Magnetometer
XRD	X-Ray Diffractometer
XRR	X-ray Reflectometry
ZFC/FC	Zero Field Cool/Field Cool

Appendix 2 CONSTANTS

Symbol	Name	SI Unit	CGS Unit
m_e	Electron Rest Mass	9.109×10^{-31} kg	9.109×10^{-34} g
μ_B	Bohr Magneton	9.274×10^{-24} J·T^{-1}	9.274×10^{-21} erg·G^{-1}
μ_0	Vacuum Permeability	$4\pi\times10^{-7}$ N·A^{-2}	1
k_B	Boltzmann Constant	1.380×10^{-23} J·K^{-1}	1.380×10^{-16} erg·K^{-1}
h	Planck Constant	6.626×10^{-34} J·s	6.626×10^{-27} erg·s
eV	Electron Volt	1.602×10^{-19} J	1.602×10^{-12} erg

Appendix 3 Publications in Period (2005-2013)

1. R. Zhang, T. A. George, P. Kharel, R. Skomski, and D. J. Sellmyer, 'Susceptibility of Fe Atoms in Cu Cluster', Journal of Applied Physics, **113** (2013)
2. R. Zhang, R. Skomski, X. Z. Li, Z. Li, P. Manchanda, A. Kashyap, R. D. Kirby, S. H. Liou, and D. J. Sellmyer, 'L10 CrPt Phase Formation and Magnetic Properties', Journal of Applied Physics, **111** (2012)
3. R. Skomski, Z. Li, R. Zhang, R. D. Kirby, A. Enders, D. Schmidt, T. Hofmann, E. Schubert, and D. J. Sellmyer, 'Nanomagnetic Skyrmions', Journal of Applied Physics, **111** (2012)
4. X. Yin, D. Le Roy, R. Skomski, R. Zhang, B. Gilg, S.H. Liou, and D.J. Sellmyer, 'Magnetization Reversal Behaviors of Patterned Fe-Alloy/Fe:SiO2 Bilayers', Journal of Applied Physics, (2012)
5. M. A. Peck, Y. Huh, R. Skomski, R. Zhang, P. Kharel, M. D. Allison, D. J. Sellmyer, and M. A. Langell, 'Magnetic Properties of NiO and (Ni, Zn)O Nanoclusters', Journal of Applied Physics, **109** (2011)
6. R. Zhang, R. Skomski, X. Yin, S. H. Liou, and D. J. Sellmyer, 'Reversibility and Coercivity of Fe-Alloy/Fe: SiO2 Multilayers', Journal of Applied Physics, **107** (2010)
7. R. Skomski, R. Zhang, P. Kharel, A. Enders, S. H. Liou, and D. J. Sellmyer, 'Magnetic Susceptibility of Nanoscale Kondo Systems', Journal of Applied Physics, **107** (2010)
8. S. H. Liou, R. Zhang, S. E. Russek, L. Yuan, S. T. Halloran, and D. P. Pappas, 'Dependence of Noise in Magnetic Tunnel Junction Sensors on Annealing Field and Temperature', Journal of Applied Physics, **103** (2008)
9. J. Shi, Y.F. Lu, H. Wang, K. J. Yi, Y. S. Lin, R. Zhang, S. H. Liou, 'Synthesis of suspended carbon nanotubes on silicon inverse-opal structures by laser-assisted chemical vapor deposition', Nanotechnology, **17** (2006)
10. T. Yokota, L. Gao, R. Zhang, L. Nicholl, M. L. Yan, D. J. Sellmyer, and S. H. Liou, 'The Perpendicular Magnetic Anisotropy of CoPt/Au Multilayer Films', Journal of Magnetism and Magnetic Materials, **286** (2005)
11. T. Yokota, M. L. Yan, Yingfan Xu, L. Gao, R. Zhang, L. Nicholl, L. Yuan, R. Skomski, D. J. Sellmyer, S. H. Liou, C. Lai, C. Yang, and S. Huang, 'Magnetic Properties and L10 Phase Formation of FePt Films Prepared by High Current-Density Ion-Beam Irradiation and Rapid Thermal Annealing Methods', Journal of Applied Physics, **97** (2005)